Università di Roma *"Sapienza"*

DOTTORATO DI RICERCA IN

MECCANICA TEORICA E APPLICATA

XXXIII CICLO

# Revealing the shape of turbulence in channel flows

*Chiara Pilloton*

*1165025*


Advisor:

*Dott.* C. Lugni - CNR-INM

*Prof.* F. Fedele - Georgia Tech

Tutor:

*Prof.* G. Graziani - Sapienza

25 November 2020

*"Scrivi del notare sotto l'acqua e avrai il volare dell'uccello in aria"*

---

L. da Vinci (Codice Atlantico, f. 571ar)

.

*"Molecola fluida girandola*
*in vortici trasparenti*
*seguendo percorsi assoluti*
*scansando detriti e barriere*
*di aria e ombra:*
*hai abraso il terreno*
*sfavillando in tragitti di luce,*
*mormorando nel mondo*
*la vita.*
*Or quindi qui ti lanci*
*dall'alto divenendo*
*imponente cascata*
*fragorosa di liquidi atomi*
*per poi più in là silenziarti "*

---

C. Monachesi
(Poesia per l'acqua - 7 maggio 2010)

.

*"Dove corri acqua senza fine?*
*Lontano, lontano verso l'ignoto*
*Là dove terra e cielo si uniscono per sempre!*
*Lontano, lontano verso l'ignoto*
*corre con te il mio destino!*
*Lontano, lontano*
*dove il vento, mio padre,*
*la nuvola, mia madre,*
*si confondono con l'infinito a trovar pace;*
*come il mio cuore che,*
*lontano , lontano verso l'ignoto*
*corre con te!*
*Ma dove... perché?*
*Lontano, lontano*
*verso l'ignoto*
*sempre con te!"*

---

Eugenio Monti Colla
(LA LEGGENDA DI POCAHONTAS)

.

## ABSTRACT

The proposed research focuses on a novel geometric approach to study Navier-Stokes turbulence. In the last century, the study of turbulence has been approached following the great Kolmogorov's physical insights on the inertial energy cascade and, more recently by investigating the geometry of the state space of the Navier-Stokes equations treated as a dynamical system. This novel geometric approach arises from the evidence that what is observed in physical space sometimes is not always suggestive of the hidden laws of physics of the turbulent motion. Thus, looking at the turbulent dynamics in state space may lead to a new understanding of the associated physical processes. In particular, vortices in a channel flow change shape as they are transported by the mean flow at the Taylor speed, or dynamical velocity. Removing the translational (Toric) symmetry in state space reveals that the shape-changing dynamics of vortices influences their own motion and it induces an additional self-propulsion velocity, or geometric velocity. Thus, in strong turbulence, the Taylor's hypothesis (Taylor, 1938) of frozen vortices is not satisfied because the geometric velocities can be significant. In my PhD work, I aim at revealing the shape of turbulence in channel flows. In particular, I study how vortices change shape as they are transported by the mean flow, and how these shape-changing dynamics influence their own motion. This study yields the discovery that the geometric velocity, induced by vortex shape changes, is the physical manifestation of hidden wave-like dispersion properties of turbulence.

### RESULTS

Symmetry reduction approaches provide a new way to understand the vortical motion of turbulence in channel flow (Cvitanovic et al. (2005); Fedele et al. (2015); Willis et al. (2013)). This depends on the inertia of the flow and on its own shape-changing form over time. Because of the inertia of the flow, vortices are transported at roughly the Taylor speed, the so-called dynamical velocity $V_{dyn}$ (Fedele et al. (2015)). If turbulent fluctuations are significant because of vortex stretching and tilting, vortices change shape over time as they are transported by the mean flow. Their shape-changing dynamics induces an additional "self-propulsion velocity", the so-called geometric velocity $V_{geom}$ (Fedele et al. (2015)). Thus, in strong turbulence the Taylor's hypothesis of frozen vortices is not satisfied since the geometric velocity is not negligible over the Kolmogorov's inertial range.

The Navier-Stokes (NS) equations for channel flows have translational symmetry, i.e. if the fluid velocity $u(x,t)$ and associated pressure $p(x,t)$ fields are solutions of the NS equations, so are the space-shifted $u(x+\ell,t)$ and $p(x+\ell,t)$, where $\ell$ is any shift along the streamwise direction $x$. From a dynamical system perspective, if symmetry is present, the velocity $V$ of the vortical motion can be uncoupled in to the sum of dynamical and geometric components (Fedele et al. (2015))

$$V = V_{dyn} + V_{geom}. \tag{1}$$

Such uncoupling is clearly observed in state space, and symmetry can be reduced or quotiented out to reveal the pure motion solely due to turbulence. The desymmetrized state space reveals how i) vortices change shape over time and how ii) their shape-changing influences their own motion. The Fourier representation of the velocity field is

$$u(x,t) = \sum_{-N}^{N} z_n(t) e^{ik_0 n x} \tag{2}$$

and the truncated NS state space is $\mathbb{C}^N = \mathbb{R}^{2N}$, where $N$ is the number of Fourier modes. As $N \longrightarrow \infty$ the state space becomes of infinite dimensions. We collect the Fourier modes $z_n$ in a vector $z$ and the NS equations can be rewritten as

$$\dot{z} = F(z), \tag{3}$$

where $F(z)$ is a nonlinear vector function of $z$. Translational symmetry in physical space becomes a Toric symmetry (T-symmetry) in Fourier space, i.e. if the set $\{z_n\}$ of Fourier modes is a solution of Eq. (3), so is $\{z_n \exp(ik_0 n\ell)\}$, for any shift $\ell$. The state space $\mathbb{C}^N$ has the geometric structure of a fiber bundle (see Fedele et al. (2015) and references therein). The bundle is made of a base manifold $B \in \mathbb{C}^N$ of dimensions $\mathbb{R}^{2N-1}$ and 1D fibers along the direction of T-symmetry that attach at any point of $B$.

The T-symmetry can be reduced by devising a reduction map $\pi$ that maps trajectories or orbits $z(t)$ of $\mathbb{C}^N$ onto desymmetrized orbits $Z_D(t)$ of the base manifold $B$. The map $\pi$ is invariant under the T-symmetry and it can be interpreted as a coordinate change transformation that allows for a map representation of the abstract base manifold. There are infinite ways to represent such manifold, i.e Mercatore projection, stereographic projections, etc. The desymmetrized orbit $Z_D(t)$ depends only on the shape-changing dynamics of vortices as in the motion of a jellyfish. Geometric and dynamical velocities allow studying the motion of the vortical motion in the desymmetrized frame. Figure 1b shows the mean velocity profile $V_m$ of a turbulent channel flow at $Re = 3300$ $(Re_\tau = 180)$. The regime of turbulence is strong and the Taylor hypothesis is not satisfied. The dynamical velocity $V_{dyn}$ is estimated as if

vortices were transported by and frozen in the flow. $V_{dyn}$ underestimates the observed mean velocity and the geometric component $V_{geom}$, proportional to $V_m - V_{geom}$, is not negligible, indicating that the shape-changing of vortices affects their own speed.

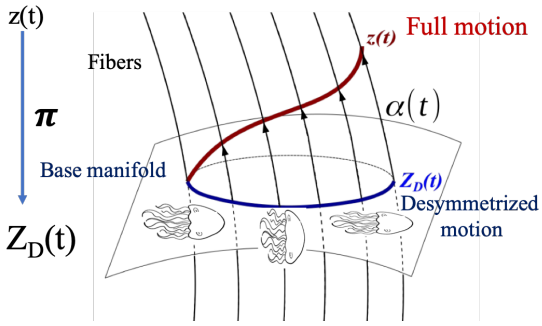


(a) Desymmetrization concepts

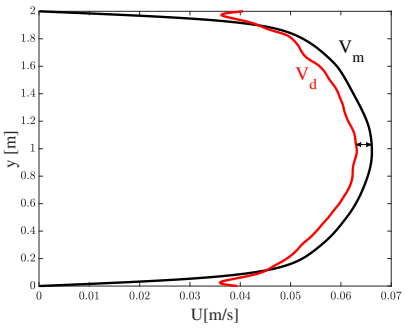


(b) Dynamic and geometric velocity

The group orbit of a trajectory $z(t)$ is a sheet of the fiber bundle and it is defined as

$$\begin{cases} G(z) = \{G_\alpha(z(t)) \quad \forall\, t\} \\ G_\alpha(z(t)) = \left\{z_n(t)e^{in\alpha}, \quad \alpha \in [0\ 2\pi]\right\} \end{cases} \tag{4}$$

Typical group orbits of $\mathbb{C}^N$, visualized in a 3D subspace are depicted in figures 2. The simulated full trajectory or orbit $z(t)$ (black line), the orbit in the comoving frame (green line) and the desymmetrized orbit $Z_D(t)$ (blue line) are also shown. The comoving frame trajectory is that seen from a frame that moves with the dynamical velocity $V_{dyn}$. The desymmetrized trajectory is seen from a frame that moves at the total speed $V = V_{dyn} + V_{geom}$, sum of the dynamical and geometrical velocities.

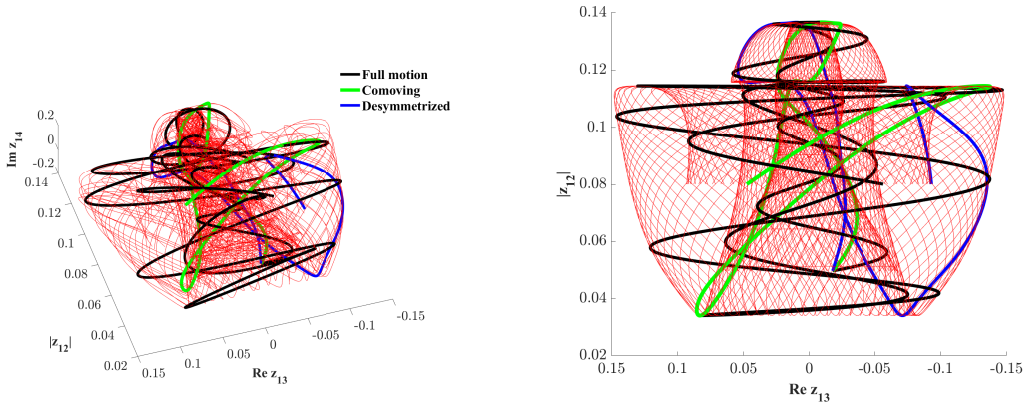


Figure 2: Group orbit of DNS turbulent channel flow

This novel approach is applied to both the global dynamics in a channel flow and to a reduced dynamics of few vortices followed in their motion along the channel. In particular, the study of two vortices and their merging, from which a third vortex arises, reveals the effect of the shape changing dynamics of vortices to their own motion. Moreover, in the Kolmogorov's inertial range, the geometric velocity is induced by the vortex shape-changing dynamics, which is the physical manifestation of an hidden wave-like of dispersion property of turbulence. In particular,turbulent motion behaves as capillary-type in the wall region of the channel and as of deep-water type waves in the centerline region.

## CONCLUSIONS

Symmetry reduction approaches are new ways to study the anatomy of the vortical motion in channel flows. Because of the inertia of the flow, vortices are transported at the Taylor speed, the so-called dynamical velocity (Fedele et al., 2015). When the vortex shape changes over time, it induces an additional self-propulsion velocity, the so-called geometric velocity (Fedele et al., 2015). Thus, in strong turbulence the Taylor's hypothesis of frozen vortices is not satisfied since the geometric velocity is not negligible. At least, the physical manifestation of an hidden wave-like dispersion property of turbulence is noticed. The dispersion properties of turbulence is revealed using symmetry reduction method and Boccotti's quasi-determinant theory (Boccotti, 2008).

# CONTENTS

# 1

# INTRODUCTION TO THE THESIS

Under turbulence a dictionary says: ”strong sudden movements within air or water” or ”violent or unsteady movement of air or water, or of some other fluid” or ”a state of confusion without any order”, a state of conflict or confusion”. These are some definitions of turbulence: starting from a physical point of view, its meaning it is used in terms of social, psychological and political conditions and behaviour. When one thinks about turbulence, his mind goes towards something chaotic, uncontrollable and incomprehensible and sometimes frightening. The contradiction lies in the fact that our daily life is perennially surrounded by turbulent phenomena. There are many occasions to observe turbulent conditions in our daily life as a smoke from a chimney, water into a river or waterfall or the buffeting of a strong wind on leaves. In the waterfall the flow is unsteady, irregular, seemingly random and chaotic and its eddies and droplets motion seems to be unpredictable (Pope, 2001). In chimney the smoke rises and increases in speed and its motion passes from ordered to disordered and vortices follow each other making sometimes beautiful shapes. To understand how much turbulence is present in our life, let's consider that the earth is covered for two thirds by water from the oceans and seas where turbulence plays an important role in sea currents, wave motions and the wind interaction in weather condition and ecosystems life (Lesieur, 2012). The wave mode is extraordinarily complex due to the water interaction with the bottom sea and winds. This is the case of extreme phenomena such as rogue waves, ”a huge wave that appears from nowhere and disappears without a trace” (Fedele et al., 2016), an open problem (Fedele et al., 2017), where turbulent airflow over steep ocean wave may play an important role in its development. In the emerged lands there are rivers and streams in which the water generates swirling and chaotic motions in waterfalls, rapids and hydraulic jumps. Finally, the earth's surface is surrounded by the atmosphere where the circulation of air masses takes place, which allows the exchange of heat between areas with different temperatures and humidity. In clouds, updrafts, and intense cyclonic phenomena, very well known to pilots and engineers, turbulence plays an important role but it is often counteracted. Turbulence is widely present in flora and fauna reigns. Flying birds benefit from turbulence (Mallon et al.,

2016). On the contrary, nocturnal raptor have wings whose shape is such as to reduce as much as possible the turbulence in order to be less noisy and hunt without being heard by their prey (Krishnan et al., 2020). Even animal-induced turbulence in the ocean (Huntley and Zhou, 2004) or the effect of flow turbulence on the swimming speed was deeply studied (Lupandin, 2005). These considerations are necessary to understand that the presence of fluids in nature is so wide that the study of fluid dynamics is fundamental and turbulence plays a huge role. In other words, without turbulence the earth would not be as we know it. Obviously, the study of turbulent flows encounters considerable practical applications, some of which try, albeit in vain, to reduce it or at least to control it. Aeronautical and mechanical engineering study turbulent flows around the wings and that induce resistance, vibrations and noises causing possible to the vehicle's structures and its dynamic. In the ducts' turbulence causes friction and reduction of the flow rate and, in the case of engines, it produces problems in combustion. All engineering applications lead to a continuous deep study in turbulence having as their objective the prediction of the effects and its control. From a strictly physical point of view, there is an ever greater need to understand this physical phenomenon in order to have a further explanation of the interconnected phenomena. The essential feature of turbulent flow is that fluid velocity varies significantly and irregularly in space and time and it allows the transport and the mix of fluid much more effectively than a comparable laminar flow. Despite the considerable research conducted on the origin and behavior of turbulence, still today there is no a clear and complete understanding of its dynamics, which motivates the numerous studies still existing and, in some way, also the research activity of the present thesis.

## 1.1 MOTIVATION AND BACKGROUND

Turbulence is a challenging research topic which is sometimes at the origin of serious fights within the scientific research community originated by the extremely different points of view. All of them have in common the model complexity based on the Navier-Stokes equation, as well as the inability to solve the problem at all (Lesieur, 2012).
In the last century, the Navier-Stokes equations have been studied and explored thanks to the great Kolmogorov's physical insights on the inertial energy cascade. However, turbulence is not still fully understood.
In the last decade, turbulence has been approached by studying the Navier-Stokes equations applied to a chaotic dynamical system. Such novel approach arises from the evidence that what happens or it is observed in physical space sometimes is not significant to fully understand the hidden physics laws of the turbulent motion. Thus, moving in the state space of the dynamical system may lead to new understanding of the associated physical processes.

The aim of my Ph.D. work consists in revealing the shape of turbulence of channel flows. This will be realized by looking at how vortices change their shape, how they are transported by the mean flow, and how the shape deformation dynamics influences their own motion.
The first studies on the dynamics of turbulence date back to the Renaissance. All the hydraulic works, done up to then, were based entirely on a purely experiential approach. Leonardo, an Italian inventor, artist and scientist, a man of genius and universal talent, he was probably the first started to questioning on turbulence. Leonardo was a good observer of nature and his passion became almost an obsession. He was fascinated by the vortical and turbulent motions not only of water, but on all systems governed by the same laws, as blood. In the Codex Leicester he provided unprecedented depictions of vortices and their infinite variability. With its devastating spiral dynamics, the vortex is an expression of the irrepressible force of nature. Nothing can resist its destructive action that continually changes the surface and the belly of the Earth (da Vinci, 2020). In figure 1.1b the famous "Cascades of water" based on the Atlantic code where the Reynolds decomposition and dispersion are clearly drawn: there is a mean flow where fluid has a principal circular motion and fluctuations move getting smaller and smaller (Wikipedia, 2020). In a stolen picture of Leonardo (see figure 1.1c) called 'Leda and the swan' (1505) is incredibly visible in woman's curly hair its perennial study and observation on nature in the vortical motion. The first detailed description of wave motion and the effects of their impact on the shores of the sea or on the banks of rivers was found in the Leicester Code. Leonardo interpreted wave motions in terms of dynamic motion. He analysed the impact of the wave on the shore with an exceptional degree of detail, highlighting the back protrusions of the crest that collides with the next wave dividing into two parts (see figure 1.1d)

Leonardo was also the first in using the term 'turbulence' to describe the swirling motion of a fluid, thus using it with its current scientific meaning. In the Codex Atlanticus preserved at the Ambrosiana Library in Milan, reads (Treccani, 2020):

*"Doue la turbolenza dellacqua rigenera, doue la turbolenza dellacqua simantiene plugho, doue la turbolenza dellacqua siposa"*
"Where water turbulence is generated, where water turbulence lasts for a long time, where water turbulence settles"

This demonstrates how Leonardo intuited some physical characteristics of turbulence at the basis of modern theory, which begins with the works of William T. Kelvin, Lewis F. Richardson and Andreij N. Kolmogorov and governed by the Navier-Stokes equation. All available evidence suggests that the phenomenon of turbulence is consistent with the Navier-Stokes equation (Sreenivasan, 1999) or the Navier-Stokes equations contains all of the turbulence information (Frisch, 1995). The Navier-Stokes equation are a set of partial

(a) An apocalyptic deluge drawn

(b) Waterfalls-Atlantic code

(c) Leda and the swan picture

(d) Leicester Code

Figure 1.1: Leoanardo's drowns

differential equations which describe the motion of viscous fluid substances. In 1823, Claude-Louis Navier derived the equation of motion of a viscous fluid by adding a friction term proportional to the velocity gradient to the Euler equation. Navier's work was later perfected by the Irish mathematician and physicist George G. Stokes and, but less known, it was the results of the cumulative work of heroes such as J.R. d'Alambert, L. Euler, A.L Cauchy, S.D Poisson, J.C.B. Saint Venant (Sreenivasan, 1999). Despite it has been still 200 years and even if in some cases it can be solved using modern calculators, the Navier-Stokes equation presents mathematical difficulties still to be solved and little understood. Although the formulation of Navier-Stokes equations is quite easy, their behavior is not. The main difficulty lies in being strongly non-linear equations. A problem that remained a matter of debate for almost a century was the meaning to be attributed to the adjectives irregular and chaotic, used to describe in a qualitative way the turbulent motion of a fluid. It should be noted that, on a conceptual level, the problem is made even more difficult and

interesting. In a turbulent flow, it is possible to observe some well-defined and regular structures, such as vortices, which are continuously formed and destroyed. Turbulence is an irregular mixture of eddies of all sizes. It was Reynolds (1883-1894) who declared a new beginning of the study of turbulence. Studying pipe flow, he identified two different flow regimes, laminar and turbulent and the criterion for the onset of turbulence in terms of the nondimensional parameter that has his name: Reynolds number ($Re = UL/\nu$). The Reynolds decomposition was his new statistical method where he splinted the fluid motion into mean and fluctuation parts. He understood also that the nonlinear terms in the Navier-Stokes produce additional stresses called Reynolds stresses (Sreenivasan, 1999). This approach highlights the so called "closure problems " in turbulence: "if one generates from the Navier-Stokes equations an auxiliary equation for a low-order moment such as the mean value, that equation contains higher-order moments, so that, at any level in the hierarchy of moments, there is always one unknown more than the available equations" (Sreenivasan, 1999).
Although Reynolds addressed the problem, the merit goes to Keller and Friedmann who derived the general dynamic equations for two point velocity moments and showed that the equations for each moments also contain high order moments. In order to solve the problem, the moment equations have been closed by involving various statistical hypotheses. The most famous are Boussinsew, Taylor, Prandtl and vomn Kármán who postulated relations between turbulent stress and the gradient of mean velocity closing the equation. Taylor (1935) introduced the concept of homogeneous and isotropic turbulence that is statistically invariant under translation, rotations and reflections of coordinates. He derived the equations for turbulent vorticity and started the use of Fourier transform and spectral representation.
In reality, turbulence is not homogeneous and isotropic, so in 1941 Kolmogorov (1941b) published his revolutionary postulated, known with the jargon as K41,in which the "small" scale of turbulence are universal even though "large" scale are specific to a given flow or class of flow with the same boundary condition (Kolmogorov, 1941). In K41, Kolmogorov showed the energy spectral density varies with the wave number k according with $\phi(k) = c_k \epsilon^{2/3} k^{-5/3}$ where $\epsilon$ is the rate at which the energy is dissipated by the low end of the small scales and $c_k$ is unknown but defined as an universal constant called Kolmogorov constant. In K41 he explained the basic dynamic of coupling that is assumed to be between scales of similar size and how the energy cascade (also studied by Richardson) is injected in the large scales and it is dissipated in the small scales. The key assumption is that $< \epsilon >$ is independent of viscosity and it is the only relevant dynamical property of the flow. When it is combined with $\nu$

the kinematic viscosity of the fluid, the smallest length scale in the flow can be calculated by dimensional analysis and it given by (Nelkin, 2000):

$$\eta = (\nu^3/ < \epsilon >)^{1/4} \cong LRe^{-3/4} \tag{1.1}$$

Landau in 1944 showed the limits of Kolmogorov's theory, demonstrating the non universality. This was explained by the fact the turbulence flows are intermittent ((Frisch, 1995)). In particular, turbulent flow shows active zones, characterized by the concentration of vortices with high speeds, followed by zones of inactivity where the flow has characteristics of laminarity. In this way the turbulence turns out to be intermittent both considering the speed range, but also taking into account the rate energy dissipation, the latter being linked to speeds (Meringolo, 2009).
From the intermittent hypothesis, several interpretative models have been proposed and also Kolmogorov himself in 1962 presented a modified version of his original theory (Kolmogorov, 1962).
In 1960s Mandelbrot was the first to connect intermittence through fractal patterns and in 1985 Parisi and Frisch developed the multi-fractal model. The real revolution appeared with the introduction of the "Chaos Theory", as a new approach to study the non liner system and thus turbulence with a deterministic approach (Frisch, 1995).
The works of Henri Poincaré, David Ruelle, Edward Lorenz, of the Russian school of Andreij N. Kolmogorov and his students Jacov G. Sinai and Vladimir I. Arnold, led to a profound understanding of the concept of chaotic motion and unpredictability, or irregularities and chaotic motions. Thanks to these works, it has been possible to understand how a physical system, even if described by absolutely deterministic laws, can behave in an apparently random and unpredictable way, just like it happens in turbulence. It should be noted that some of these concepts have found direct confirmation, stimulating the interest of many researchers, thanks to the use of numerical simulations as a new investigation tool, and in some cases an alternative, compared to the theory-experiment dichotomy existing in scientific research. As explained by Ruelle, turbulence at low Reynolds numbers corresponds to a mathematical phenomenon observed in the study of solutions of differential equations

$$dx/dt = F(x). \tag{1.2}$$

This is the equation describing a generic dynamical system. In many cases, solutions have an asymptotic behaviour when $t \to \infty$ and as a consequence, the flow appears chaotic, "turbulent", and the solutions depend in a sensitive manner on initial condition (Ruelle, 1976). Lorenz was the first to interpret turbulence by solutions of differential equations which appear chaotic with sensitive dependence on the initial conditions. In particular, these chaotic solutions belong to the attractor, the set of numerical values toward which the

system tends to evolve, for a wide variety of starting conditions of the system. System that gets close enough to the attractor remains close even if slightly disturbed.

In the last thirty years, two different points of view on turbulence have been carried out. The first, 'statistical', tries to model the temporal evolution of the average quantities of the flow. This follows the theories of Taylor and Kolmogorov, believing in the phenomenology of the energy cascade. The second, 'order from chaos', considers turbulence from a purely deterministic point of view, studying both the behavior of dynamical systems and the stability of the flow under different circumstances. This community is also associated with experimentalists who seek to identify coherent structures in turbulence (Lesieur, 2012) Much of the qualitative understandings and aspects of turbulence have been acquired from Reynolds to the present day. These advances have been useful in practice, although there are many obscure points in our understanding of this phenomenon.

It has been remarked that viewing turbulence as one problem remains difficult. The large and different approaches, such as astrophysical, mechanical, aeronautical, atmospheric physical and chemical engineering make difficult a focused frontal attack and a unique solution (Sreenivasan, 1999). A real but amazing representation of turbulence community and some of main approaches (theoretical, experimental and numerical) are shown in figure 1.2.

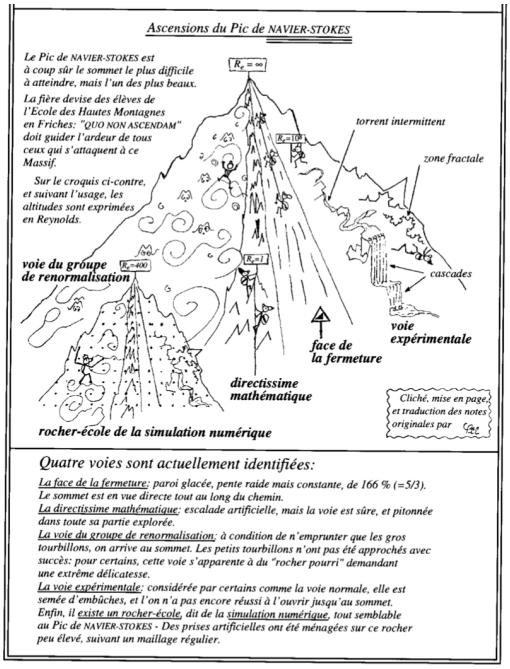


Figure 1.2: "Climbs of the peak of Navier-Stokes" Cartoon drawn of turbulence community by Philippe Delache from (Frisch, 1995)

## 1.2 STATE OF THE ART

As previously stated, turbulence is a huge branch that has been studying for more than 150 years and is still an open problem. My research starts from a numerical procedure to turbulence thought the well-known problem of turbulent channel flow using the statistical approach.
The incompressible and viscous channel flow is one of the main physical problems used for studying turbulence. While the laminar condition has a theoretic solution, the turbulence one is still a physical open problem under investigation. Since the study started, there have been numerous advances from an experimental and numerical point of view thanks to the evolution of instruments and methods of measurement and the increase of computing power.
The first studies were of an experimental nature. Nikuradse (1929) and Reichardt (1938) were the first to investigate the fully developed turbulent channel flow. Nikuradse's measurements were centered on the mean flow,while Reichardt was able to measure the fluctuations in streamwise and wall normal directions. Laufer (1951) was the first to present detailed turbulence statistics. Comte-Bellot(1963) added higher-order statistics such as two point correlation, energy spectra, skewness and flatness factors. Clark (1968) documented additional information in the region near the wall at high Reynolds numbers. Hussain and Reynolds conducted experiment at high Reynolds numbers ($Re = 13800 - 33300$) and for extremely long times, in order to reach, with higher-order statistics, a fully developed turbulence. Eckelmann and Kreplin (1974) were the first to give detailed information regarding turbulence structures near the wall. Despite the great efforts, there were discrepancy among results may be due to the wide range of Reynolds numbers used and also the technological difficulties in the experiment measures, in particular near the wall. Now it is well know how Reynolds number affects the log law men velocity profile.
For these reason numerical simulations became an important research tool to investigate the physic of turbulence and there was an important effort to develop this methods. Unlike the turbulence models as RANS and LES, in direct numerical simulation (DNS) the Navier–Stokes equations are completely solved. It allows to solve the whole range of temporal and spatial scales of turbulence. However, the DNS is not applied to all turbulent cases caused by its high computational cost but only to moderate Reynolds numbers. Accurate DNS calculations of turbulent channel flow have been carried out by (Kim et al. (1987), Lyons et al. (1991), Antonia et al. (1992), Kasagi et al. (1992),Rutledge and Sleicher (1993), Moser et al. (1999),Abe et al. (2001), Iwamoto et al. (2002),Del Alamo and Jiménez (2003),del Álamo et al. (2003), Tanahashi et al. (2004),Iwamoto et al. (2005) ,Hoyas and Jiménez (2006), Hu et al. (2006),Alfonsi and Primavera (2007),Lozano-Durán et al. (2012),Lozano-Durán and Jiménez

(2014),Vreman and Kuerten (2014b), Bernardini et al. (2014), Lee and Moser (2015) and Alfonsi et al. (2016))

| Authors | Method | Years | $Re_\tau$ |
|---|---|---|---|
| (Kim et al., 1987) | Spectral | 1987 | 180 |
| (Lyons et al., 1991) | Spectral | 1991 | $Re_b = 2075 - 2262$ |
| (Antonia et al., 1992) | Spectral | 1992 | $Re_b = 3300 - 21500$ |
| (Kasagi et al., 1992) | Spectral | 1992 | 150 |
| (Rutledge and Sleicher, 1993) | Spectral | 1993 | 180-2800 |
| (Moser et al., 1999) | Spectral | 1999 | 180,395,590 |
| (Abe et al., 2001) | Finite Difference | 2001 | 180,395,640 |
| (Iwamoto et al., 2002) | Spectral | 2002 | 110–650 |
| (Del Alamo and Jiménez, 2003) | Spectral | 2003 | 180-550 |
| (del Álamo et al., 2003) | Spectral | 2004 | 1900 |
| (Tanahashi et al., 2004) | Spectral-Finite Difference | 2004 | 800 |
| (Iwamoto et al., 2005) | Spectral | 2005 | 2320 |
| (Hoyas and Jiménez, 2006) | Spectral-Finite Difference | 2006 | 2003 |
| (Hu et al., 2006) | Spectral | 2006 | 1440 |
| (Alfonsi and Primavera, 2007) | Spectral-Finite Difference | 2007 | 180 |
| (Lozano-Durán et al., 2012) | Spectral | 2012 | |
| (Lozano-Durán and Jiménez, 2014) | Spectral | 2014 | 4200 |
| (Vreman and Kuerten, 2014b) | Spectral | 2014 | 590 |
| (Vreman and Kuerten, 2014a) | Spectral | 2014 | 180 |
| (Bernardini et al., 2014) | Finite Difference | 2014 | 4000 |
| (Lee and Moser, 2015) | Spectral | 2015 | 5200 |
| (Alfonsi et al., 2016) | Spectral | 2016 | 200,400,600 |

Table 1.1: Overview of DNS Turbulent channel flow

The scientific community set exact Reynolds number, as function of friction-velocity $U_\tau$, $Re_\tau = u_{tau}\delta/\nu$, equal to some values $180, 395, 590, 640$ in order to have the same turbulent regime and to be able to compare their results. In this study, the DNS simulation of turbulent channel flow is set at $Re_\tau = 180$, that is the first regime of fully developed turbulence. In 1987 Kim, Moin and Moser (Kim et al., 1987) performed the first DNS simulation at $Re_\tau = 180$ with pseudo-spectral code and in 1990 Moser, Kim and Mansour (Moser et al., 1999) repeated the simulation with the same numerical method but with a quite different computational domain (Kim, 2012). A recent comparison at the same $Re_\tau = 180$ of DNS databases and new simulations was conducted by (Abe et al. (2001), Vreman and Kuerten (2014a) and Alfonsi et al. (2016)) using spectral method. The present simulation were conducted with an open source code, called OPEN-Foam, base on a finite volume method. Although this methodology was not the best performing in terms of computational cost,

it was used because it was the simplest and fastest available to obtain results aimed to find a methodology for a new characterization of turbulence and to test the DNS code for future applications. The core of this study was the application of the symmetry-reduction method on the numerical results. It was possible exploiting the symmetry of channel flow, called translational symmetry. More in general, a symmetry is any discrete or continuous invariance group of dynamical theory. Let G denote a group of transformation acting on space-time function $v(t, r)$, which are spatially periodic and divergenceless. In Navier-Stokes equation G is said to be *symmetry group* if ,for all $v$ solution of NS equation, and all $g \in G$, the function $gv$ is also a solution (Frisch, 1995). The symmetries of NS equation are:

- *Space-translation* $g_\rho^{time} : t, r, v \longrightarrow t, r + \rho, v, \qquad \rho \in \mathbf{R}^3$
- *Time-translation* $g_\tau^{time} : t, r, v \longrightarrow t + \tau, r, v, \qquad \tau \in \mathbf{R}$
- *Galilean-translation* $g_U^{Gal} : t, r, v \longrightarrow t, r + Ut, v + U \qquad U \in \mathbf{R}^3$
- *Parity* $P : t, r, v \longrightarrow t, -r, -v$
- *Rotations* $g_A^{rot} : t, r, v \longrightarrow t, Ar, Av, \qquad A \in SO(\mathbf{R}^3)$
- *Scaling* $g_\lambda^{scal} : t, r, v \longrightarrow \lambda^{1-h} t, \lambda r, \lambda^h v, \qquad \lambda \in \mathbf{R}_+, h \in \mathbf{R}$

If space and time symmetries are obvious, the listed symmetry, except for the scaling symmetry, are the macroscopic consequence of the basic symmetries of Newton's equation governing microscopic molecular motion in the classical approach. The presence of symmetry and its removal represents a possibility to discover an hide turbulence structure's behavior. It is based on the chaos theory approach. Chaos theory defines the non linear equation of Navier-Stokes in state space as a infinite dimensional sets of exact solutions (attractors as equilibrium points, stable and unstable periodic orbits), which form a rigid skeleton that allows to describe and predict the motions of turbulent flows (Cvitanovic et al., 2005) and (Cvitanović and Gibson, 2010). The incompressible turbulence flows in pipe flow has been examined as chaotic dynamics in the state space of a high-dimensional system at moderate Reynolds numbers (Fedele et al., 2015) and it can be visualized as a sequence of close passages to unstable periodic orbits typical of time-recurrent dynamical coherent structures (Cvitanović and Gibson, 2010). In this approach turbulence is structured as a effective random paths in state space through a collection of invariant ('exact') solution of Navier-Stokes equations (Willis et al., 2013). In state space, the turbulent trajectory travel around the equilibrium solution, periodic orbits, passing from one saddle to another through their stable and unstable periodic orbits (Fedele et al., 2015). The studies on the geometry of 2D Kolmogorov flow (Chandler and Kerswell, 2013) revealed that the unstable periodic orbits are the skeleton of the chaotic dynamic of turbulent flow. In channel flow the intrinsic

continuous streamwise translational symmetry hides the periodic orbits that have inside the characteristic of the flow structures. These structures travel downstream with the Taylor's velocity, a drift velocity, connected with the streamwise translational simmetry (Fedele et al., 2015). Recently the geometry of the state space of a pipe flow at moderate Re numbers was investigated by the symmetry reduction through the method of slices (Siminos and Cvitanović (2011) and Willis et al. (2013)). Furthermore (Budanur et al., 2015) applied the first Fourier slice to a spatially extended system, such as channel or pipe flows. These system are equivariant under continuous symmetry transformations because each state of the flow have an infinite numbers of equivalent solutions obtained from it by a translation or a rotation. This method permits to reveal the shape-changing dynamic in a symmetry reduced space such as a base manifold and one dimensional transverse fibers attached to it associated with the group symmetry. The state space is the geometric representation of the non-linear dynamical system as a high dimensional system in $\mathbb{C}^N$ made by a fiber bundle, where N are the degrees of freedom (DOFs) of the dynamical system. The symmetry reduction decomposes the state space of the dynamical system in a base manifold, the desymmetrized dynamics (not associated to the drift), and transverse fibers attached to it along the symmetry associated to the drift (Hopf (1931) and Marsden et al. (1990)). Furthermore, the symmetry reduction in state space allows uncoupling vortical speed in a dynamic phase velocity component $U_d$ related to the symmetry and in the geometric phase velocity $U_g$ induced by the shape changing dynamics of the turbulence structures (Fedele et al., 2015). In other studies at high Reynolds numbers, the associated Navier-Stokes equations has been reduced to a set of coupled Korteweg-de Vries–type (KdV) equations that support inviscid and smooth travelling waves. The weakly nonlinear dynamics of small long-wave disturbances to the laminar state in non-rotating axisymmetric Poiseuille pipe flows was studied (Fedele, 2012) to localized travelling waves in form of toroidal vortices concentrated near the pipe boundaries (wall vortexons) or that wrap around the pipe axis (centre vortexons)(Fedele and Dutykh, 2013b). Such studies suggest that vortices of the turbulent flow are analogous to ocean wave groups in the capillary to deep-water gravity waves regime. Following their "crest" motion is possible to figure out their speed up and slow down related to the geometry and dynamical phases $c = U_g + U_d$ (Fedele, 2014). The motion of vortices (slow down and speed up) and their interplay depend on the dispersion similar to the energy exchange as the ocean waves. The novelty of this dissertation is represented by:

- Symmetry reduction method applied to DNS turbulent channel flow simulation.
- Symmetry reduction approaches as new ways to study the anatomy of the vortical motion. This depends on the inertia of the flow and on its own shape-changing form over time.

- Because of the inertia of the flow, vortices are transported at the Taylor speed, the so-called dynamical velocity (Fedele et al., 2015)
- The shape-changing dynamics induces a "self propulsion velocity", the so-called geometric velocity (Fedele et al., 2015)
- In strong turbulence, the Taylor's hypothesis (Taylor, 1938) of frozen vortices is not satisfied since the geometric velocity is not negligible (Fedele, 2014).
- In the Kolmogorov's inertial range, the geometric velocity is induced by the vortex shape-changing dynamics, which is the physical manifestation of an hidden wave-like dispersion property of turbulence (Fedele, 2014).
- The Boccotti's quasi-deterministic method (Boccotti, 2008) was applied to vorticity field treated as a wave group in order to further demonstrate the wave-like dispersion of turbulence. In particular, turbulent motion behaves as capillary-type in channel's wall region and as deep water waves in channel's centreline.

## 1.3 STRUCTURE OF THE THESIS

The research done in this dissertation is based on the cooperation activity between University of Roma 'Sapienza' and CNR-INM (ex INSEAN) and the Georgia Institute of Technology (Atlanta - USA). The thesis has the same structure as the logic that was followed during the study: numerical simulations of the turbulent channel, the study on the symmetry reduction of discrete vortices as Hamiltonian systems, symmetry reduction theory and its application on turbulent channel flow turbulence and the investigation on the wavelike behaviour of turbulence. It is decomposed into three parts. In the first part, Chapter §2 presents a brief historical reference to the turbulent channel flow, the numerical simulation results and comparisons with literature. It is necessary to remark that the numerical simulation were used as an investigation tool to obtain fluid dynamic data in order to study turbulence evolution thorough symmetry reduction method.
The second part deals with the symmetry reduction method. In Chapter §3 the method is introduced studying the symmetry reduction concepts on a simpler system of discrete planar vortices exploiting the Hamiltonian theory. In Chapter §4, the deeply and general explanation of the symmetry reduction method from geometric and mathematics point of view. In Chapter §5 the results of the application of symmetry reduction on turbulent Channel flow data: the translational symmetry is removed to the global field of vorticity, demonstrating the Taylor's hypothesis are non consistent with high turbulence regime. Later a system of few vortices were tracked to go deeply inside the

physics of turbulence and reveal the shape of turbulence.
The third part contains the wave theory and its application on vorticity field to discover the dispersive wave-like property of turbulence. In Chapter §6 a wave group of capillary wave and deep water wave was studied in order to understand the different dispersive behaviours and associated to vortices through the application of the quasi-deterministic theory: boundary layer vortices behave as capillary wave while central channel vortices as deep water wave. Finally in Chapter §7 the conclusion of that work and the future prospective to move on in this scientific research of turbulence.

# 2

# TURBULENT CHANNEL FLOW

The turbulent channel flow problem has been studied intensively to increase the understanding of the dynamic of wall-bounded turbulent flow. Unlike the laminar channel in which the particles have smooth path and highly ordered, in the turbulent channel they are characterized by velocity fluctuation and highly disordered motion. The transition from laminar to turbulent flow does not occur immediately; rather, it occurs over some region in which flow fluctuates between laminar and turbulent motion before it becomes fully turbulent. The simple geometry allowed to perform a first numerical simulation on turbulence; its velocity and pressure data provided information to complement experiments in the study of the physic of this chaotic dynamic system. Numerical simulations are one of the way to approach turbulence flow investigation. Unlike the RANS (Reynolds-Averaged Navier-Stokes) and LES (Large eddies simulation) method, the direct approach of solving Naver-Stokes equations for turbulence flows, called direct numerical simulation (DNS), is the most straightforward and powerful research tool for investigating simple turbulent flows at moderate Re. In the direct numerical simulation (DNS) the Navier–Stokes equations are numerically solved without any turbulence models. This means that the whole range of spatial and temporal scales of the turbulence are resolved. The objective of this work is to perform the direct numerical simulation of the fully developed channel flow at $Re = 3300$ using a open source code called OpenFoam. The database obtained by such simulation is of considerable value for qualitative and quantitative studies of the structures of turbulence and to design and test the numerical code for future perspective for more complex flows. The computed flow field was used in this study to carry out a new characterization of turbulence. The obtained results were compared with the available numerical and experimental data. Agreements as well as discrepancies will be presented in detail. The formulation of the continuous problem and the computational set-up, including physical and numerical parameters, computational domain and initial and boundary condition are described in this chapter. Results and comparison will be presented below.

## 2.1 THE CONTINUOUS PROBLEM AND THE PHYSICAL PARAMETERS

The developed turbulence in channel flow is a theoretical case consisting of a flow passing through two infinite parallel planes, driven by a constant pressure gradient. The scientific community decided to set the coordinated system as shown in figure 2.1 Let the x-axis be in the direction of negative pressure

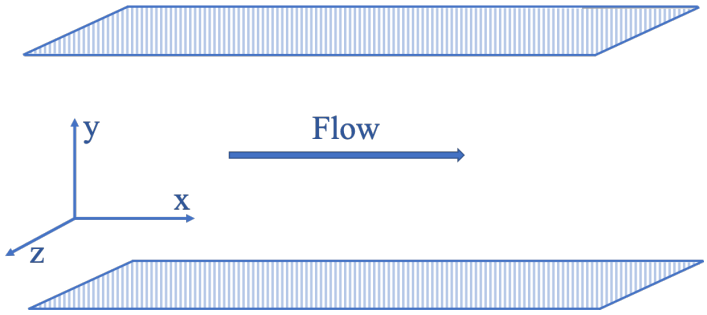


Figure 2.1: Coordinate system in channel

gradient coinciding with that of the mean flow i.e. the *streamwise* direction. The y-axis is taken to be orthogonal to the walls, pointing from the lower to the upper and it is named as *wall-normal* direction. Finally, the z-axis is given so that (x,y,z) forms a orthonormal coordinate system and it is called *spanwise* direction. Since the walls are considered as infinite size, the only geometric parameter is the channel width, $h$ or the distance between the two plane, $\delta = h/2$ is the channel half-width while the bottom and the top walls are at $y = 0$ and $y = h$ respectively. While in the experiments it is more difficult to reproduce the infinite extension of the walls, in numerical simulations the channel is artificially truncated in x and z direction, but the infinity is made thanks to the periodic boundary conditions. Despite this, in both cases, the effective dimensions of the channel have to be large enough to fit the largest turbulent structures inside the domain. In this case, the simulations were conducted using the same geometric dimensions as in Kim et al. (1987).

The physical parameters of the flow are the driving pressure gradient and the kinematic viscosity of the fluid $\nu = \mu/\rho(m^2/s)$. The problem is well-defined when these two parameters are given. The pressure gradient can be imagined directly related to the power of a fan or a pump to maintain the velocity constant in order to contrast the viscous effects. The dimensionless quantity called Reynolds number $Re = \frac{UL}{\nu}$, allows to defines the flow regimes: increasing the Reynolds number, the flow passes from laminar to turbulent regime. In the case of channel flow, an alternative to the pressure gradient, easier to set, is the *mean bulk velocity* $U_b$

$$U_b = \frac{1}{h}\int_0^h < u(x,y,t) >_{xz} \, dy \tag{2.1}$$

with $< \cdot >$ the average in x e z direction. The Reynolds bulk number is

$$Re_b = \frac{U_b h}{\nu}. \tag{2.2}$$

The flow is laminar for $Re_b < 1350$ and fully turbulent fro $Re_b > 1800$ although transitional effects are evident up to $Re_b = 3000$. The kinematic viscosity $\nu$ can be viewed as a viscous diffusivity of momentum and another characteristic velocity scale is the wall *friction velocity* $u_\tau$ defined as a function of the wall shear stress $\tau_w$ and of the fluid density $\rho$:

$$u_\tau = \sqrt{\frac{\tau_w}{\rho}} \tag{2.3}$$

and the friction Reynolds number is:

$$Re_\tau = \frac{u_\tau \delta}{\nu} \tag{2.4}$$

evaluated of the channel half-width. The case tested is at $Re_\tau = 180$ that coincides to $Re_b = 3300$.

### 2.1.1 *Mean force balance*

The fully developed channel flow is statistically stationary and one-dimensional, with velocity statistics (mean value, Reynolds stress, mean square root) depending only on y. The Reynolds decomposition equations:

$$u = U(y) + u' \qquad v = V(y) + v' \qquad w = W(y) + w' \tag{2.5}$$

allows to separate the mean velocity components $U(y), V(y), W(y)$ from the fluctuations $u', v', w'$. The Reynolds-Averaged Navier-Stokes equations, in tensor notation, result:

$$\begin{cases} \frac{\partial U_i}{\partial x_i} & = 0 \\ \rho \frac{DU_i}{Dt} & = \frac{\partial}{\partial x_i}(\overline{T}_{ij} - \rho(u_i' u_j')) \end{cases} \tag{2.6}$$

with

$$\frac{\partial \overline{T}_{ij}}{\partial x_j} = -\frac{\partial P}{\partial x_i} + \mu \frac{\partial^2 U_i}{\partial x_j \partial x_j} \tag{2.7}$$

the internal forces and without the mass force contribution. Moreover, the flow is statistically symmetric about the mid-plane $y = \delta$ that brings to $W(y) = 0$. Since $W(y) = 0$ and $U = U(y)$, the mean continuity equation reduces to:

$$\frac{dV(y)}{dy} = 0 \tag{2.8}$$

and with the boundary condition at bottom wall $V(0) = 0$ yields $V(y) = 0$ so that the boundary condition at the top wall $V(2\delta) = 0$ is satisfied. The lateral (y) mean-momentum equation reduces to:

$$0 = -\frac{d}{dy}(\overline{v'^2}) - \frac{1}{\rho}\frac{\partial P}{\partial y} \tag{2.9}$$

which, with the boundary condition $(\overline{v'^2})_{y=0} = 0$, integrates to

$$\overline{v'^2} + P/\rho = p_w(x)/\rho \tag{2.10}$$

where $p_w$ is the mean pressure at the bottom wall. An important consequence from this equation is that the mean streamwise pressure gradient is uniform across the flow:

$$\frac{\partial P}{\partial x} = \frac{dp_w}{dx} \tag{2.11}$$

Moreover, the streamwise mean-momentum equation is:

$$0 = \nu\frac{d^2U}{dy^2} - \frac{\overline{u'v'}}{dy} - \frac{1}{\rho}\frac{\partial P}{\partial x} \tag{2.12}$$

and can be written as:

$$\frac{d\tau}{dy} = \frac{dp_w}{dx} \tag{2.13}$$

where the total shear stress $\tau(y)$ is:

$$\tau = \rho\nu\frac{dU}{dy} - \rho\overline{u'v'} \tag{2.14}$$

As a consequence in this flow there is no mean acceleration, so the mean momentum equation consists of a balance of forces: the axial normal stress gradient and the cross-stream shear stress gradient. Since $\tau$ is a function only of y and $p_w$ is a function only of x, both $d\tau/dy$ and $dp_w/dx$ are constant and the solution of $\tau(y)$ and $dp_w/dx$ can be expressed in terms of the wall-shear stress:

$$\tau_w = \tau(0) \tag{2.15}$$

The shear stress $\tau(y)$ is anti-symmetric about the mid-plane. The solution of the equation 2.13 is:

$$\frac{\tau_w}{\delta} = -\frac{dp_w}{dx} \tag{2.16}$$

and

$$\tau(y) = \tau_w(1 - \frac{y}{\delta}) \tag{2.17}$$

The flow is driven by the pressure gradient in x direction between the entrance and the exit of the channel. It is needed to balance the shear stress gradient in y direction given by the equation 2.17 So the flow is defined if $\rho, \nu\delta$ are specified toghether with one between the pressure gradient $dp_w/dx$, the mean velocity $\overline{U}$ or the center-line velocity $U_b$ (Pope, 2001).

### 2.1.2 *Shear stress and turbulent velocity profile*

Consider the fluid entering in the channel with a uniform velocity. The no-slip condition given by the presence of the walls causes the complete stop of the layer of particles in contact with the wall. This causes the layers immediately over to slow down gradually as a results of friction. To counterbalance this velocity reduction the particle's velocity in the mid-section of the channel has to increase to keep the mass flow rate constant. The region of the flow in which the effects of the viscous shearing forces are stronger is called *boundary layer*. Hypothetically, the channel in the xy plane is divided in two regions: the boundary layer region in which the viscous effects are significant and the irrotational flow region where the viscous effects are negligible and the velocity remains essentially constant in the streamwise direction. The thickness of the boundary layer increases in the flow direction until it reaches the channel mid-section and thus it fills the entire channel and the flow is said to be fully developed. The velocity profile in the fully developed region is parabolic in laminar flow and flatter in turbulence flow due to the eddies motion and more vigorous mixing in the streamwise direction. Turbulent flow is characterized by random and rapid fluctuations of swirling regions, called eddies. The intense mixing of the fluid in turbulent flow is a result of rapid fluctuations which enhance momentum transfer between fluid particles, increases the friction force on the surface and thus the required pumping power. The friction reaches a maximum when the flow becomes fully turbulent. The time-averaged velocity profile remains unchanged when the flow is fully developed. The shear stress $\tau_w$ is related to the slope of the velocity profile at the wall surface. If the velocity profile remains unchanged also the wall shear stress remain constant in that region. How turbulence affects the wall shear stress is one of the most important aspects of the turbulent flows. The time average of fluctuations is zero and its magnitude is usually just a few percent of $U$ but the high frequency of the eddies make it very important for the momentum transport and for the pressure drop. The turbulent fluctuations increase the shear stress $\tau$. The total shear stress can be considered the sum of a laminar component $\tau_{lam} = -\mu dU/dy$, which accounts for the friction between layers in the flow direction and a turbulent component that depends from the velocity fluctuation $\tau_{turb} = -\rho\overline{u'v'}$, also called Reynolds stress, In compact form it is:

$$\tau_{tot} = \tau_{lam} + \tau_{turb} \tag{2.18}$$

Many semi-empirical formulation, called turbulence model, has been developed in order to model the Reynolds stress terms and to provide a mathematical closure to the equations.

One of the simplest model suggested by the mathematician J. Boussinesq is:

$$\tau_{turb} = -\rho\overline{u'v'} = \mu_t \frac{\partial U}{dy} \tag{2.19}$$

where $\mu_t$ is called eddy viscosity and $\nu_t = \mu_t/\rho$ the kinematic eddy viscosity. While $\nu$ is the molecular diffusivity of momentum and it is a fluid property, the eddy viscosity is not a fluid property and its value depends on flow conditions: it decrease toward the wall and becomes zero at the wall but exceeds several thousand times the value of $\nu$ in the core region. The velocity gradients at the wall and the wall shear stress of turbulent flow are much larger than laminar flow and they change the shape of the mean velocity profile. While the mean velocity profile of laminar flow is parabolic and constant in space and time and its expression is given by an exact solution, the fully developed turbulent profile is flatter with a sharp drop near the channel wall. In fact the turbulent boundary layer is thicker than the laminar one for the same value of the free stream velocity.

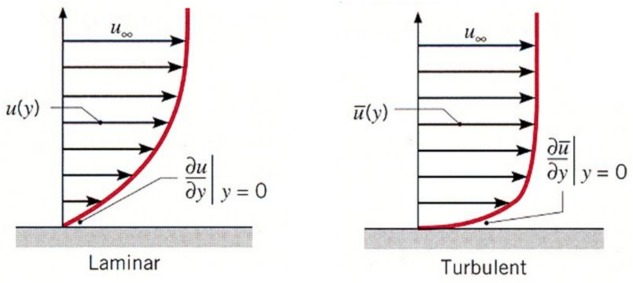


Figure 2.2: Comparison between laminar and turbulent boundary layer shape

Turbulent boundary layer can be considered to be divided in four regions, identified moving away from the wall :

- viscous sublayer
- buffer layer
- inertial sublayer
- outer layer

The viscous sublayer is the very thin layer next to the wall where the viscous effects are dominant. In this region the velocity profile is quite linear and the flow is laminar. Next to the viscous sublayer is the buffer layer in which the turbulent effects becomes significant but the flow is still dominated by the viscous effects. Above the buffer layer there is the transition layer called inertial sublayer where the turbulent effects are much more relevant than before. Finally

there is the outer layer where the turbulent effects are predominant over the viscous effects. There is not an analytic expression for the thickness of the boundary layer and for their extensions as exists for the laminar flow. Generally the viscous sublayer is very small (generally 1% of the channel width) but it plays a dominant role caused by the large velocity gradient. The latter remains nearly constant in the viscous sublayer $du/dy = u/y$ and the wall shear stress can be expressed as

$$\tau_w = \mu \frac{u}{y} \rightarrow \qquad \frac{\tau_w}{\rho} = \frac{\nu u}{y} \tag{2.20}$$

where the quantity $\frac{\tau_w}{\rho}$ is related to the friction velocity $u_\tau = \sqrt{\frac{\tau_w}{\rho}}$ and by substituting it in the equation 2.20, the velocity profile in the viscous sublayer is obtained in dimensionless form as:

$$\frac{u}{u_\tau} = \frac{\nu u_\tau}{\nu} \tag{2.21}$$

that is also called the *law of the wall*. The thickness of the viscous sublayer is found by the experimental data to be roughly:

$$y = \delta_{sublayer} = \frac{5\nu}{u_\tau} \tag{2.22}$$

that results to be proportional to the kinematic viscosity and inversely proportional to the friction velocity. As a results, the viscous sublayer gets thinner as the velocity increases and consequently the velocity profile becomes nearly flat and the velocity distribution becomes more uniform at high Re numbers.

The quantity $\nu/u_{tau}$ is called *viscous length* or *wall unit* and it is used to nondimensionalize variables as distance and velocity:

$$y^+ = \frac{y u_\tau}{\nu} \qquad u^+ = \frac{u}{u_\tau} \tag{2.23}$$

The law of the wall becomes simply :

$$u^+ = y^+ \tag{2.24}$$

In the overlap layer, dimensional analysis and experiments confirmed that the velocity is proportional to the logarithm of the distance and the velocity profile can be express by:

$$\frac{u}{u_\tau} = \frac{1}{\kappa} \ln \frac{y u_\tau}{\nu} + B \tag{2.25}$$

where $\kappa$ and B are constants whose values are evaluated experimentally to be about $\kappa = 0.41$, called Karman constant, and $B = 5.2$ and the *logarithmic law* is:

$$u^+ = 2.5 \ln y^+ + 5.2 \tag{2.26}$$

with $1/\kappa = 2.5$. As will be explained later, further studies have been carried out and corrections have been made to this expression. However, comparisons with DNS data of fully developed turbulent channel flows for $109 < Re_\tau < 2003$ showed good agreement (Absi, 2009)

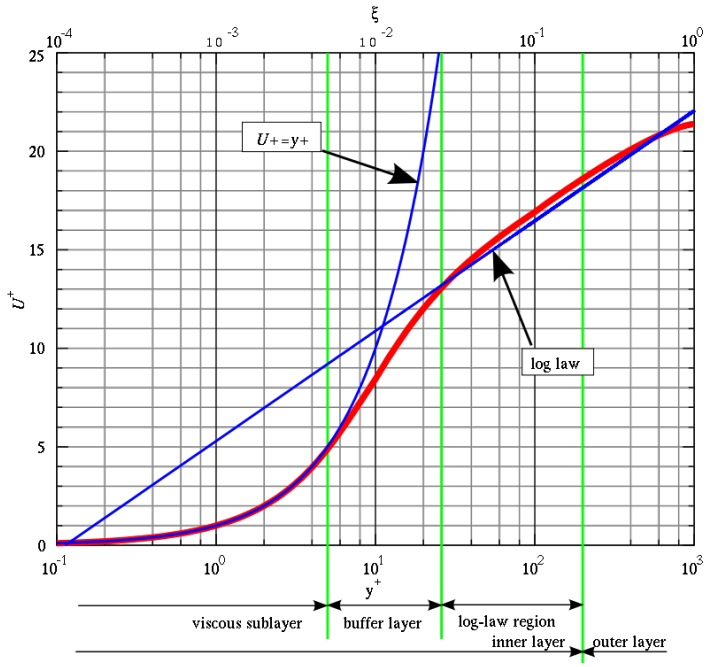


Figure 2.3: Universal velocity profile

For a first interpretation, the universal velocity profile, has two main regions: the inner layer and the outer layer. The *inner layer*, in wall units, is composed by the region very close to the wall in the *viscous sublayer* for $0 < y^+ < 5$, the *buffer layer* for $5 < y^+ < 30$ and the logarithmic law in the *inertial sublayer* for $y+ > 30$ . The *outer layer* is for $y^+ > 50$ where the direct effects on the mean velocity U are negligible and it is characterized by the *velocity defect law* as :

$$\frac{U_0 - U}{u_\tau} = F\left(\frac{y}{\delta}\right) \tag{2.27}$$

that is the difference between the mean velocity U and the center-line value $U_0$ and it is independent from the viscosity of the fluid.

## 2.2 NUMERICAL METHOD

### 2.2.1 *Govening equations*

The NS equations fully describes the motions of fluid particles in the case of turbulent channel flow. The well-know equations for an incompressible and viscous flow are given by:

$$\begin{cases} \frac{\partial \mathbf{u}}{\partial t} + (\mathbf{u} \cdot \nabla)\mathbf{u} = -\frac{\nabla p}{\rho} + \nu \nabla^2 \mathbf{u} + \mathbf{f} \\ \nabla \cdot \mathbf{u} = 0 \\ +\text{I.C} \\ +\text{B.C} \end{cases} \tag{2.28}$$

where $\mathbf{u}$ is the velocity of the fluid, $\rho$ the density, $p$ is the pressure and $\nu$ the viscosity. "I.C" and "B.C" are respectively the initial and boundary conditions needed to close the mathematical problem. While the incompressibility of the fluid is given by the continuity equation $\nabla \cdot \mathbf{u} = 0$, the momentum equation is composed by the terms with the following meaning:

$$\overbrace{\underbrace{\frac{\partial \mathbf{u}}{\partial t}}_{\text{Acceleration}} + \underbrace{(\mathbf{u} \cdot \nabla)\mathbf{u}}_{\text{Convection}}}^{\text{Inertia (per volume)}} - \underbrace{\nu \nabla^2 \mathbf{u}}_{\text{Diffusion}} = \underbrace{-\frac{\nabla p}{\rho}}_{\substack{\text{Internal} \\ \text{source}}} + \underbrace{\mathbf{f}}_{\substack{\text{External} \\ \text{source}}} \tag{2.29}$$

System 2.28 is locally nonlinear. One of its peculiar characteristics is that of constituting a hyperbolic / parabolic hybrid system. In fact, the first equation for the conservation of mass is hyperbolic while the equations for the balance of the amount of motion and energy conservation are parabolic in nature. It is then said that the incompressible equations constitute an incomplete parabolic system. In particular, the system is composed of 4 equations:

- one for the mass conservation
- three, for each directions, of the momentum equation

and 4 unknown: three components of velocity (u,v,w) and the pressure p. The density of the fluid $\rho$ is constant in space and time. As a direct consequence, four initial and boundary conditions of velocity and pressure are necessary to close the problem.

### 2.2.2 *Solver algorithm*

The DNS numerical simulations of turbulent channel flows were carried out using OpenFOAM Open-source Field Operation And Manipulation"). It is a C++ toolbox for the development of customized numerical solvers, and pre-/post-processing utilities for the solution of continuum mechanics problems, in particular computational fluid dynamics (CFD). It based on the finite volume method. This method subdivides the flow domain into a finite number of contiguous control volumes and uses the integral forms of the equation set as a starting point. These equations are integrated and the result is a finite

number of linear algebraic equations that can be solved using matrix methods. The same code was used to perform LES simulations of turbulent channel flow (by De Villiers (2006) and Mukha and Liefvendahl (2015)) at $Re_{tau} = 395$. OpenFoam has not been used for DNS simulations of channel flows at $Re_\tau = 180$, although OpenFoam has been used to solve for other physical problems on turbulence flows by DNS simulations ( (Zheng et al., 2019),(Komen et al., 2014),(Zhang et al., 2015),(Vo et al., 2016), (Marocco and Franco, 2017)).
The solver used in the simulations exploits the PISO algorithm (Pressure-Implicit with Splitting of Operators). It is an extension of the SIMPLE algorithm used in computational fluid dynamics to solve the Navier-Stokes equations. It was proposed in 1986 without iterations and with large time steps and a lesser computing effort. PISO is a pressure-velocity calculation procedure for the Navier-Stokes equations particularly adapted to steady-state problems. The algorithm solves the discretized momentum equation, in accord with the boundary condition, to compute an intermediate velocity field, and then it carry out the mass fluxes at the cells faces. At this point it solves the pressure equation and correct the mass fluxes at the cell faces. Using the new pressure field it corrects the velocities and updates the boundary conditions. It repeats the computing the mass fluxes for the prescribed number of times and if it converges it increases the time step and repeats from the start (Ferziger et al., 2002).

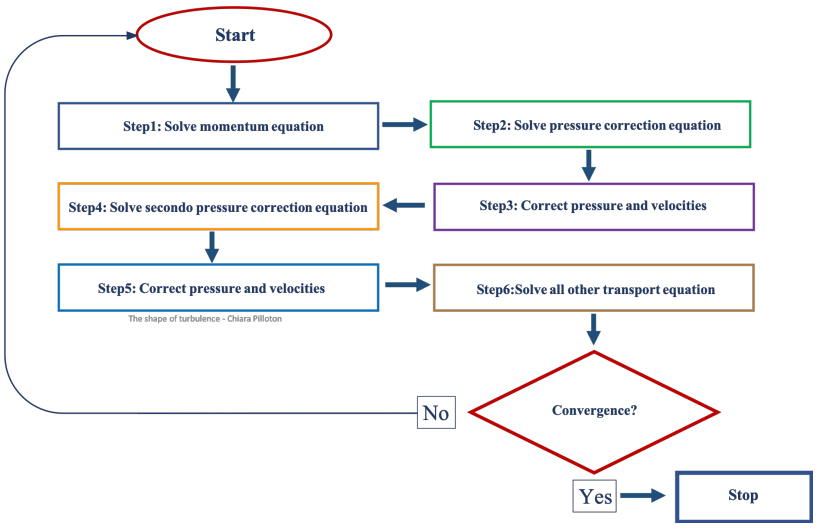


Figure 2.4: PISO algorithm's flow chart

### 2.2.3 *Computational domain and grid spacing*

Two simulation were carried out at $Re_\tau = 180$ taking into account the simulation of (Kim et al., 1987). The value of the parameters chosen for the simulations

are listed in table 2.1 (Kim et al., 1987) defined the bulk mean velocity as a

| | |
|---|---|
| $\rho$ | $1 kg/m^3$ |
| $\nu$ | $2 * 10^{-5} m^2/s$ |
| $Re_\tau$ | 180 |
| $Re_m = \frac{U_m 2*\delta}{\nu}$ | 5600 |
| $Re_c = \frac{U_c \delta}{\nu}$ | 3300 |
| $u_\tau$ | $0.0036 m/s$ |
| $U_m$ | $0.0569 m/s$ |
| $\Delta t$ | 0.15 |

Table 2.1: Parameters' values

function of the channel width h as:

$$U_m = \frac{1}{2}\int_0^h \overline{u} d(\frac{y}{\delta}) \tag{2.30}$$

so the bulk Reynolds is $Re_m = \frac{U_m 2*\delta}{\nu} = 5600$ unlike Reynolds center-line, used in literature, that is $Re_c = \frac{U_c \delta}{\nu} = 3300$ function of the channel half-width. The ratio between the mean center-line velocity to the mean bulk velocity $U_c/U_m = 1.16$, in agreement with Dean's correlation of $U_c/U_m = 1.28 Re_m^{-0.0016} = 1.16$. The dimensions of the computational domain is chosen to be in streamwise and spanwise direction periodic and large enough to capture the larges eddies in the flow 2.2

| | x | y | z |
|---|---|---|---|
| L | $Lx = 4\pi\delta$ | $h = Ly = 2\delta$ | $Lz = 2\pi\delta$ |

Table 2.2: Dimensions of computational domain

where the channel half-width $\delta = 1$.

The geometrical simplicity of the channel allows to use a structured hexahedral computational mesh. One of the goals of this part is based on the understanding of the effects of the grid size and if the numerical code and the methodology used are suitable for doing DNS simulations. Two different computational meshes are used. The first was employed with the same grid of (Kim et al., 1987) and a second with a finer mesh made of 13 million of points. The result were compared in particular with (Kim et al. (1987) , Moser et al. (1999), Abe et al. (2001)) that used a pseudo-spectral code in their simulation. It means they needed a coarser mesh, thanks to a more accuracy of the spectral codes, than finite volume code in order to have the same results. For this reason the fist simulation (M1) was carried out with the same number of points while

in the second (M2), the finest, the number of points was doubled in x and z direction, the same directions where the spectral method acts. Presumably there is a factor two of the convergence order between the spectral and finite volume codes. However, the computation effort for the second mesh (M2) was intense that it don't permit to do a finer one with the computational power and time available. The meshes were produced with an implemented Matlab code that was able to pull out the mesh files written appropriately for OpenFoam. The planned computationally intense simulations have been performed with the Georgia Tech PACE-cluster (64 nodes). Both simulations were performed decomposing the numerical domain and using parallel function. The mesh characteristics are summarized in tables respectively for M1 2.3 and M2 2.4.

| **M1** | x | y | z |
|---|---|---|---|
| N | $Nx = 192$ | $Ny = 129$ | $Nz = 160$ |
| C | $Cx = 191$ | $Cy = 128$ | $Cz = 159$ |
| $\Delta$ | $\Delta x = 0.0658$ | - | $\Delta z = 0.0395$ |
| $\Delta^+$ | $\Delta x^+ = 11.84$ | - | $\Delta z^+ = 7.11$ |

Table 2.3: Coarser Mesh M1 details

| **M2** | x | y | z |
|---|---|---|---|
| N | $Nx = 383$ | $Ny = 129$ | $Nz = 319$ |
| C | $Cx = 382$ | $Cy = 128$ | $Cz = 318$ |
| $\Delta$ | $\Delta x = 0.0329$ | - | $\Delta z = 0.0198$ |
| $\Delta^+$ | $\Delta x^+ = 5.922$ | - | $\Delta z^+ = 3.56$ |

Table 2.4: Finer Mesh M2 details

Note that the dimensionless quantity marked by the superscript $+$ were calculated at first using the theoretical value of $u_\tau$ whose value has been confirmed during the simulations. In order to increase the resolution of the turbulent structure and to reach a correct definition of the boundary layer, because of the large gradient in the wall region, a non uniform grid was used in the wall-normal direction, as (Kim et al., 1987), with the following law :

$$y_j = \cos\theta_j = \cos((j-1)\pi/(N-1)) \tag{2.31}$$

where N is the number of points in y-direction and details of the finest grid M2 (M1 has the values doubled) are listed in the table 2.5,

where $y_\delta$ is the dimension of the cell at the channel centreline and $y_\delta^+$ the unidimensional quantity.

| $y_1$ | $y_1^+$ | $y_\delta$ | $y_\delta^+$ |
|---|---|---|---|
| 0.0003134 | 0.05 | 0.05 | 7.11 |

Table 2.5: M2 details in y direction

### 2.2.4 *Initial and boundary conditions*

In order to reach faster the steady-state condition, the laminar parabolic profile of velocity, given by the theoretical solution, was employed as a initial condition of the velocity based on $Re_c = \frac{U_c \delta}{\nu}$.

Moreover to advect the streamwise flow and counteract the viscous effects, a function of OpenFOAM, called *meanVelocityForce* part of the fvOptions tool is used. It introduces an additional external force term into the momentum equation that drives the flow. The magnitude of the force is extracted by the bulk velocity . At each time step, the volume averaged velocity is computed and a correction of the momentum source is made in order to research the desired mean velocity $U_{bar}$.

$$\frac{\sum_i (\frac{\overline{u}}{|\overline{u}|} u_i) V_i}{\sum_i V_i} \tag{2.32}$$

where the summation is over the cells that belong to the user-specified domain, $\overline{u}$ is $U_{bar}$, $u_i$ is the velocity in the i-th cell and $V_i$ is the volume of the i-th cell. In particular the algorithm evaluates a pressure gradient increment needed to adjust the average velocity and reach the user-specified value $U_{bar}$. The value used as $U_{bar}$ was the velocity based on $Re_m = \frac{U_m 2\delta}{\nu}$. In order to simulate a domain of the infinite size, in the streamwise and spanwise directions periodic boundary conditions were applied for the velocity and the pressure. The first connects the boundaries at $x = 0$ and $x = L_x$ and the second $z = 0$ and $z = L_z$. Otherwise the walls were treated with the Dirichlet type (no-slip $u = 0$) boundary condition for the velocity and the Von Neumann type ($\frac{dP}{dn} = 0$) condition for the pressure .

| Boundary conditions | Type | U | p |
|---|---|---|---|
| x | Periodic | Periodicity | Periodicity |
| y | Wall | No-slip | $\frac{dP}{dn} = 0$ |
| z | Periodic | Periodicity | Periodicity |

Table 2.6: Boundary conditions

### 2.2.5 *Numerical schemes*

OpenFoam has a wide range of options for numerical schemes. It is allowed by the setting of the numerical schemes for each terms of equations, such as derivatives or laplacian, that are calculated during a simulation. In the present simulations the numerical schemes used are listed in table 2.7. In particular,

| Term | Scheme | Order |
|---|---|---|
| Time derivative $\frac{\partial}{\partial t}$ | Cranck Nicolson | 2◦ |
| Gradient $\nabla$ | Gauss linear | 2° |
| Divergence $\nabla\cdot$ | Gauss Linear | 2° |
| Laplacian $\nabla^2$ | Gauss linear | 2° |

Table 2.7: Numerical schemes

CrankNicolson is a transient, second order implicit, bounded scheme. It requires an off-centering coefficient $\Psi$ chosen here equal to 0.9 because it is used to bound/stabilize the scheme for practical engineering problems. The Gauss entry specifies the standard finite volume discretization of Gaussian integration which requires the interpolation of values from cell centers to face centers. The linear entry, means linear interpolation or central difference and it corresponds to a second order, unbounded scheme. The only drawback is the absence of numerical schemes with a convergence order higher than three and those with three are not recommended for their high numerical dissipation.

### 2.2.6 *Numerical procedures*

In order to reach faster the steady state of fully developed turbulence an additional forcing terms was used to force turbulence. A new solver has been created in which a random force $F_z$, periodic function of the mesh coordinates and with random phases, has been added to the momentum equation acting in the spanwise direction, visible in the figure 2.5. The equation of the dimensionless forcing term is the following:

$$F_z = A * C(F_1 + F_2 * F_3) f_x * f_y \tag{2.33}$$

and its terms are:

$$\begin{cases} F_1 = \cos(2Z + \theta_1) \\ F_2 = 0.1\cos(8Z + \theta_2) \\ F_3 = \cos(X + \theta_1) \\ f_x = \sin(X + \theta_2) \\ f_y = \frac{(F_{arg}^3)}{(1+F_{arg}^{16})} \\ F_{arg} = 1.8\,|Y - 1|\,A = U_{bar}^2/\delta \end{cases} \tag{2.34}$$

where the $X, Y, Z$ are the cell center coordinates divided by the channel half-width $\delta$, $\theta_1$ and $\theta_2$ are random phases. The amplitude of the forcing term is of the order of $F_z \propto 10^3 \frac{dP}{dn} = 0$

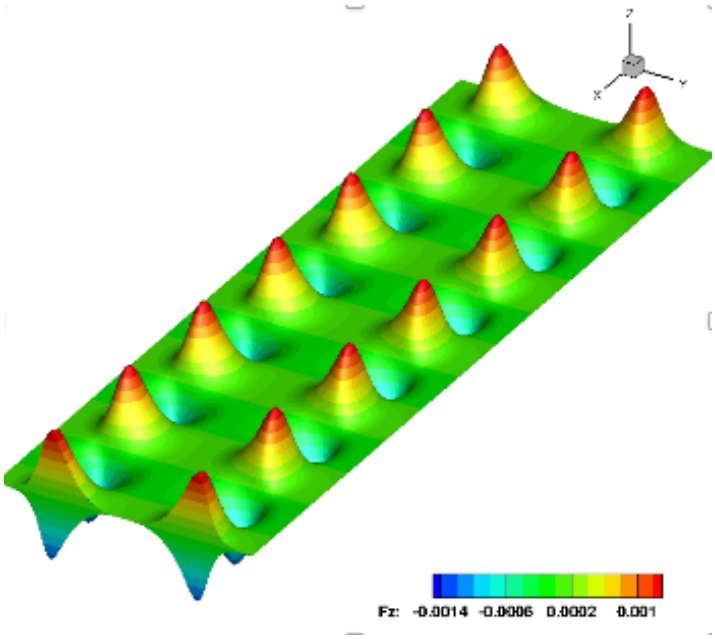


Figure 2.5: Visualization of an instant time of the forcing term $F_z$ acting in spanwise direction

The simulation for each mesh size consisted of two phases. The first when the force acts and accelerates the chaotic behaviour of fluid and the second when the force is turned off. Both the simulations were carried out for 10 non-dimensional times $t^*$ with the force $F_z$ turned on at time:

$$t^* = \frac{tu_\tau}{\delta} \simeq 10 \tag{2.35}$$

$$t = \frac{t^*\delta}{u_\tau} \simeq 3000s \tag{2.36}$$

In the second part the simulations were carried out for other $t^* = 10$ (from 3000s to 6000s) that corresponds to 500 time steps with a write interval of 40 $\Delta t$.

## 2.3 RESULTS

The following results have been obtained, for both meshes, considering the last 3000s, i.e. 500 time steps in which the forcing term $F_z$ is off. The simulation results were compared with the numerical data of (Kim et al. (1987), Moser et al. (1999), Vreman and Kuerten (2014a) and Abe et al. (2001)) and with the experimetal data of Eckelmann (1974). In the following plots are shown the data of the two simulations, the coarser(M1) and the finest (M2) compared with literature's results . It is useful to remember the coarser grid is the same used by (Kim et al., 1987), while the finest has a number of points doubled in x- and z-direction.

### 2.3.1 *Mean velocity profile*

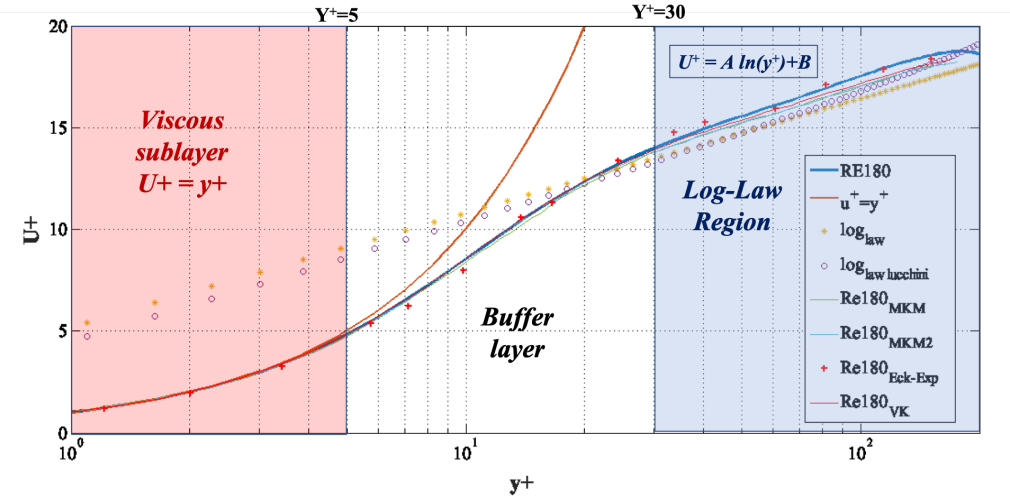


Figure 2.6: Mean-velocity profile with the definition of the sub regions of the boundary layer. The mean velocity profile of the finest mesh (RE180) is compared with numerical results of Kim et al. (1987) and Vreman and Kuerten (2014a) and experimental results of Eckelmann (1974). The Log-law was compared with that proposed by Luchini (2017).

The profile of the mean velocity non-dimensionalized by the wall-shear velocity of the finest mesh is shown in figure2.6 with the division of the three principal regions. In figure 2.7 there is a graphic convergence between the results of the two grids and a comparison with the data of (Kim et al. (1987), Moser et al. (1999), Vreman and Kuerten (2014a) and Eckelmann (1974)).

Moreover, the results were compared also with the new research made by (Luchini, 2017) that brought a correction on the turbulent velocity profile. As mentioned in (Mathieu and Scott, 2000), the pressure gradient influences the outer layer of the order of $p_x = O(1)$, whereas the viscous layer is relatively insensitive to perturbing effects. (Luchini, 2017) demonstrated that the mean velocity profile is influenced by the presence of the pressure gradient $p_x$ which in turn depends on the geometry of the problem. This problem can be solved adding a correction term in the log-law that depends on the pressure gradient that makes the low-law universal. Starting from the von Kármanʼs constant expression $\kappa = \frac{u_\tau}{y u_y}$, the correction with the pressure gradient leads to obtain:

$$\frac{u_y}{u_\tau} = \frac{1}{\kappa} - A_1 \frac{p_x}{\tau_w} \tag{2.37}$$

and, by integration, th velocity profile's law becomes:

$$u^+ = \kappa^{-1} \log(y^+) + A_1 g Re_\tau^{-1} y^+ B \tag{2.38}$$

where $A_1$ in a new universal constant, $g = -\delta p_x/\tau_w$ is a geometric parameter and $\delta$ the channel half-width. In the case of the turbulent channel flow $\kappa = 0.392$, $A1 = 1$ and $B = 4.48$.

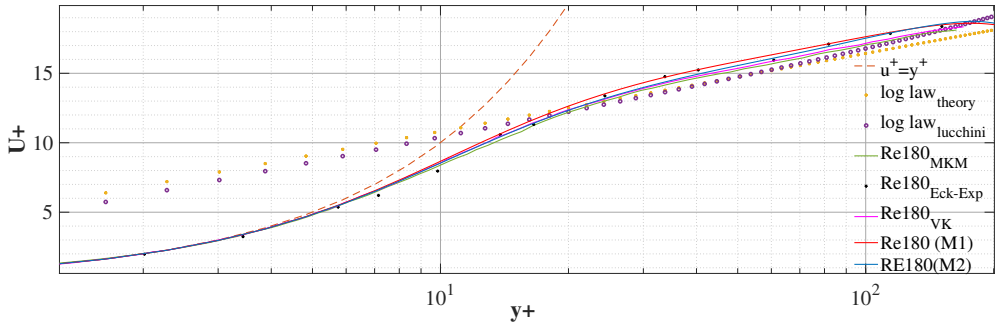


Figure 2.7: Mean-velocity profile - Coarser mesh (M1) finest mesh (M2). Comparison with numerical results of (Kim et al., 1987) and (Vreman and Kuerten, 2014a) and experimental results of (Eckelmann, 1974). The Log-law was compared with that proposed by(Luchini, 2017)

Looking at the figure 2.7 the simulations results agree much better with this new log-law. It is evident also the difference between the traditional log-law and the one proposed by (Luchini, 2017). Even if there isn't a noticeable discrepancy between the two grids, the finest one converges well with the reported results of (Kim et al. (1987), Moser et al. (1999), Vreman and Kuerten (2014a) and Eckelmann (1974) and Luchini (2017)). For the finer grid was plotted in figure 2.8 also the trend of the von-Kárman constant with this general expression :

$$\kappa = y^+ \frac{d\overline{u}^+}{dy^+} \tag{2.39}$$

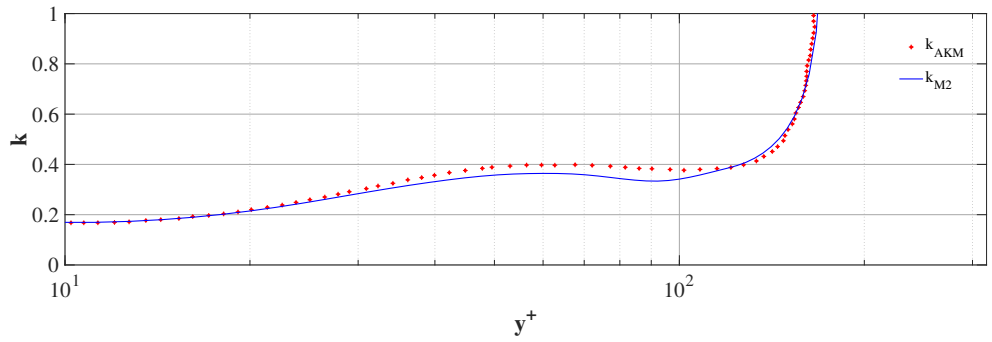


Figure 2.8: Von karman costant. Comparison with (Abe et al., 2001) results.

The skin friction coefficient $C_f$ is defined as:

$$C_f = \frac{\tau_w}{\frac{1}{2}\rho U_m} = 8 * 10^{-3} \tag{2.40}$$

and the empirical correlation proposed by Dean (1978)

$$C_f = 0.073 Re_m^{-0.25} = 8.4 * 10^{-3} \tag{2.41}$$

evaluated with simulations results that are in good agreement with (Kim et al., 1987) and (Abe et al., 2001).

### 2.3.2 *Turbulence intensities*

Turbulence intensities normalized by the wall-shear velocity are shown in figure 2.9. There is a little discrepancy in the symmetry of the profiles about the channel center-line probably given by not adequacy of the samples used for the average. The general shape is in a good agreement with the results of (Kim et al., 1987) where the finest grid matched quasi-completely.

Figure 2.10 shows the profile of root mean square pressure normalized by the wall shear velocity $p_{rms}/\rho u_\tau^2$ of the two simulations (M1) and (M2) together with the (Kim et al., 1987) results. As mentioned by (Kim et al., 1987) their results appear lower than experimental results compiled by (Willmarth, 1975) (see figure 2.11) which show that the r.m.s wall pressure in turbulent boundary layer varies between 2 and 3 as it can be seen in the figure 2.11.

It gives a good reason on the evident discrepancy between the present numerical results and ones of (Kim et al., 1987) and moreover the values increases passing from coarser to finest grid. The turbulence intensity I near the wall, is shown in figure 2.12 normalized by the local mean velocity, as a

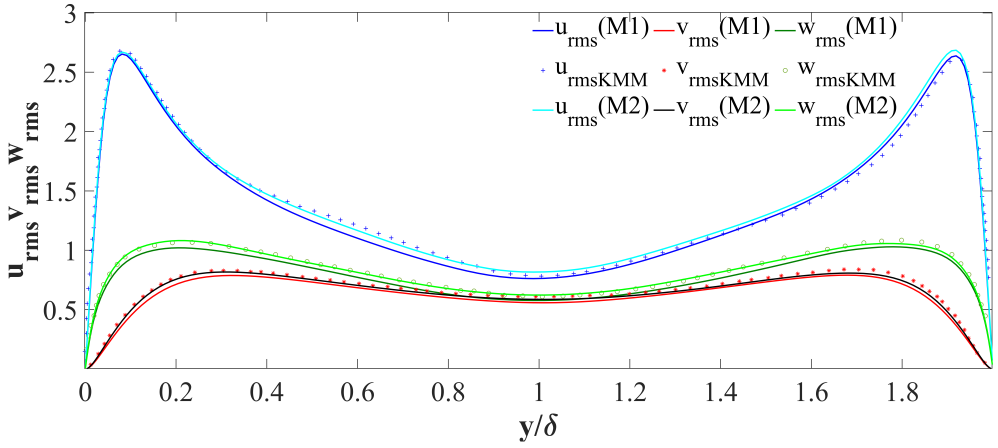


Figure 2.9: Comparison root-mean-square velocity fluctuations normalized by the wall shear velocity- In global coordinates. Compared with data of Kim et al. (1987)

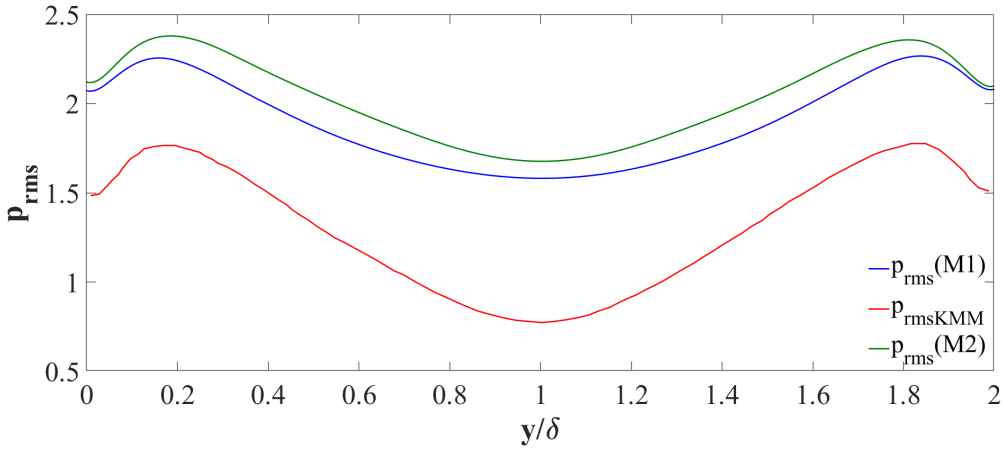


Figure 2.10: Comparison of r.m.s. pressure fluctuation normalized by the wall shear velocity.Compared with data of (Kim et al., 1987)

function of the non-dimensional wall distance $y^+$. It was evaluated for the finest grid M2 and for the three velocity components as:

$$\begin{aligned} I_u &= \frac{u_{rms}}{\overline{u}} \\ I_v &= \frac{v_{rms}}{\overline{u}} \\ I_w &= \frac{w_{rms}}{\overline{u}} \end{aligned} \tag{2.42}$$

where $\overline{u}$ is the local mean streamwise velocity as a function of the wall normal direction y. For comparison, the the DNS numerical results of (Kim et al., 1987) are shown in the same figure. It can be seen that there are weak discrepancies

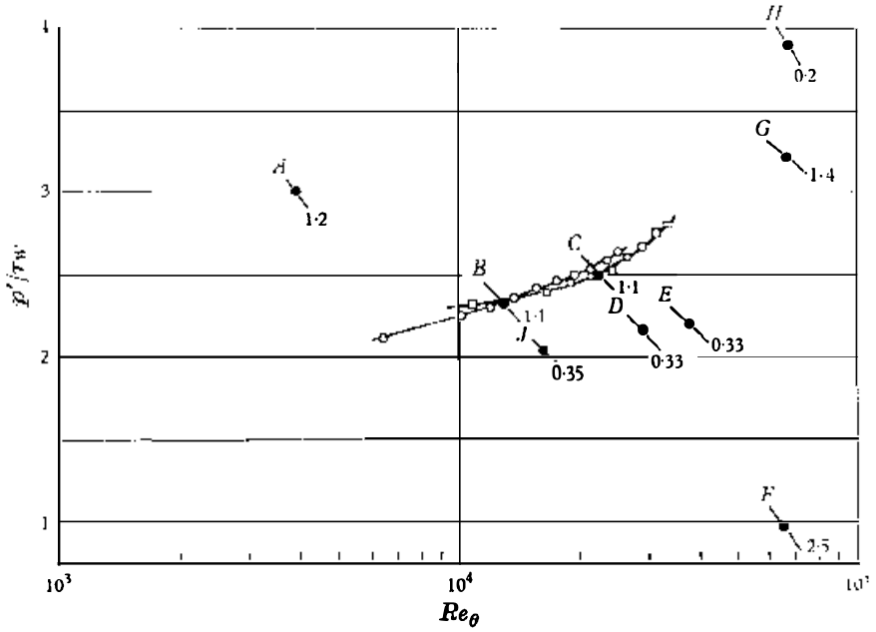


Figure 2.11: Variation of root-mean-square wall pressure with Reynolds number by (Willmarth, 1975)

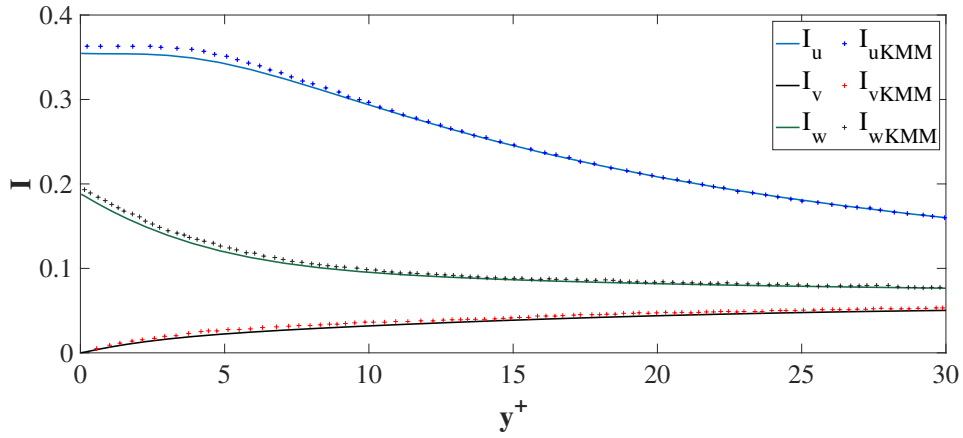


Figure 2.12: Turbulence intensity $I_u = u_{rms}/\overline{u}$ near the wall normalized by the local mean velocity. Evaluated on the finest mesh M2 and compared with the results of (Kim et al., 1987)

in the near wall region in the turbulence intensity $I_u$ (spanwise vorticity) and $I_v$ that decay moving away from the wall. It can be caused by the greater resolution at the wall given by the pseudo-spectral code and grid used by (Kim et al., 1987) . On the contrary, a better agreement is noticeable in the streamwise

vorticity intensity $I_w$ at the wall. The values of TI could suggest we are in weak turbulence condition.

### 2.3.3 *Two-point correlation and spectra*

The two point correlations in x- and z-direction at a location $y + 5.88$ are shown in figure 2.13 and 2.14. One can see the fall off of the correlation to vanishing values for large separations, demonstrating that the computational domain is large enough. For comparison, the results of (Kim et al., 1987) are also shown in the same figures.

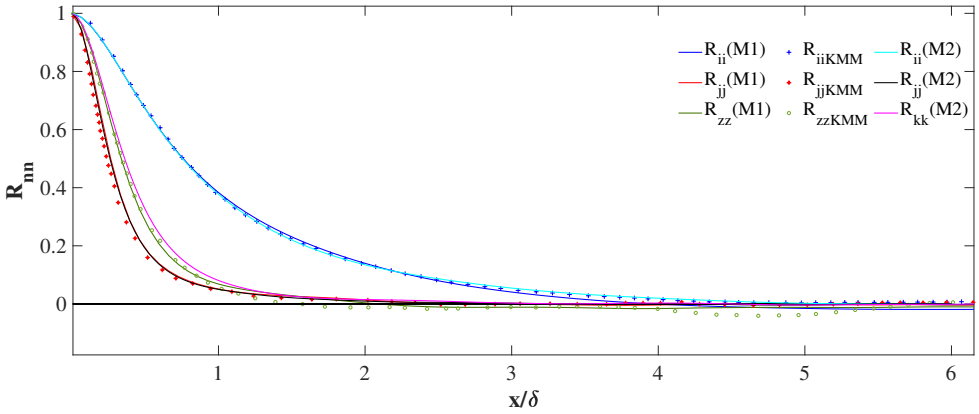


Figure 2.13: Two-point correlation of streamwise separations. Results of the two meshes (M1) and (M2) (straight line) are compared with data of (Kim et al., 1987) (dotted line)

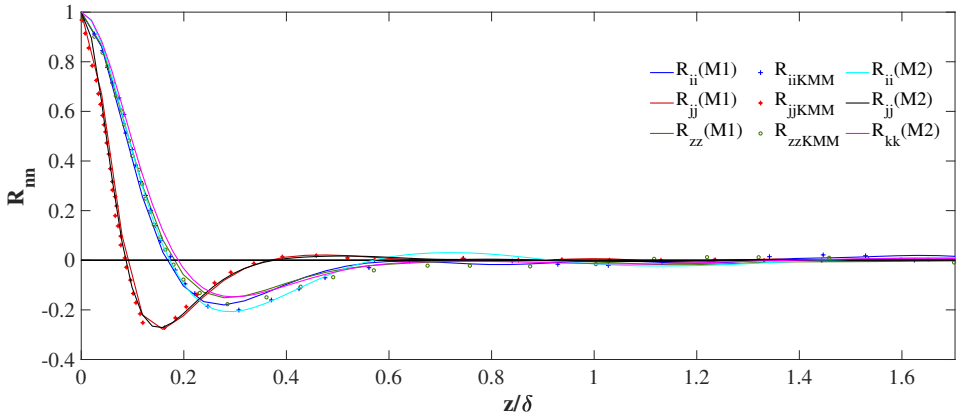


Figure 2.14: Two-point correlation of spanwise separations. Results of the two meshes (M1) and (M2) (straight line) are compared with data of (Kim et al., 1987) (dotted line)

The one dimensional energy spectra in streamwise and spanwise direction are respectively depicted in 2.15 and 2.16 as a function of the wave numbers $k_x$ and $k_z$. These quantity are necessary to understand the adequacy of the computational domain since the energy density associated with the high wave numbers is several decades lower that the energy density corresponding to low wave numbers and the absent of energy pile-up at high wave numbers. However, "the drop off of the computed spectra of high wave numbers is not sufficient evidence that the data are unaffected by the small scale motion neglected in the computation. It is not clear what significant dynamical roles, if any, these small scales would play if included in the computations" ((Kim et al., 1987)).

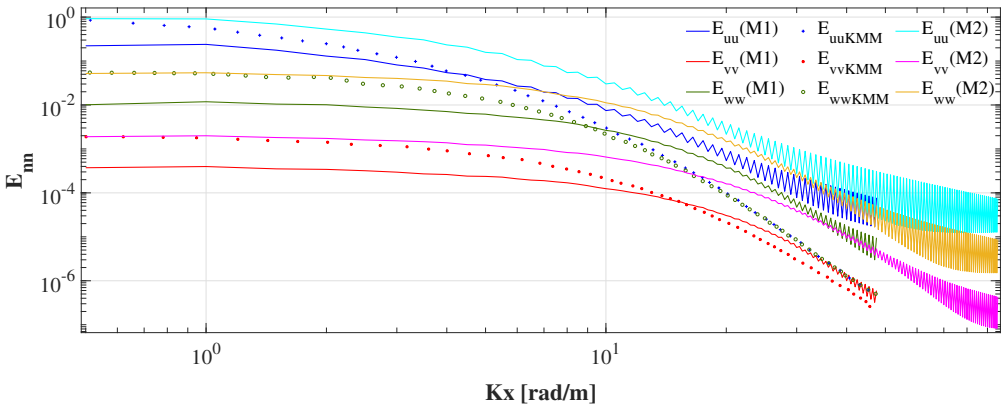


Figure 2.15: One dimensional energy spectra-Streamwise. Compared with data of (Kim et al., 1987)

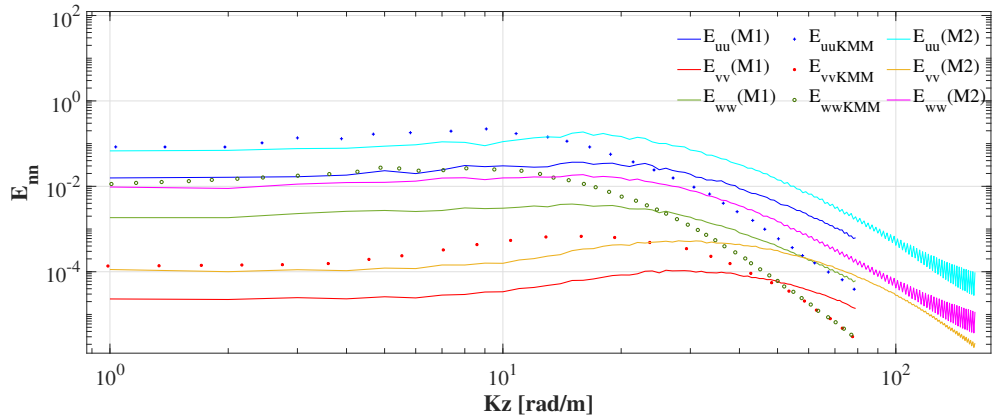


Figure 2.16: One dimensional energy spectra-Spanwise. Compared with data of (Kim et al., 1987)

The computed spectra have the same order of magnitude and the same trend of (Kim et al., 1987) but there isn't a total agreement. What is evident is that the finest grid is able to collect the energy spectra at higher wave numbers. It is presumably given by the capability of capturing smaller-scale than the coarser grid that stops at the same wave numbers. The decay of energy occurred in both the simulations,but with wave numbers higher than the KMM results. Moreover the finer grid agrees much better with the results of KMM at low wave numbers than the coarser one, indication that the doubling of the points was correct to compare better the two different codes. Both the simulations show also the oscillations at high wave numbers, that is more marked in the finer grid probably due to the not fully achieved steady-state or by an anisotropy produced by the forcing term that energize much more the small-scales.

### 2.3.4 *Energy cascade*

After demonstrating that the finest mesh converges better towards the comparison results, it is interesting to analyze the spectrum. In the turbulence theory, the energy cascade is valuable from the energy spectrum evaluation. It plays an important role to understand if the turbulence is fully developed because it involves the transfer of energy from the large scales to the small scales in the case of direct energy cascade. This transfer of turbulence kinetic energy is typical of the non-linear dynamic of the Navier-Stokes equation. The energy spectrum of turbulence is related to the mean turbulence kinetic energy as:

$$\frac{1}{2}(\overline{u'u'}) = \int_0^{inf} S(k)dk \tag{2.43}$$

The energy spectrum, $S(k)$, represents the contribution to turbulence kinetic energy by wavenumbers from $ktok + dk$. The largest eddies have low wavenumber, and the small eddies have high wavenumbers caused by their frequency. Looking at the figure 2.17 of $S(k)/S_{max}$, the inertial sub-range, where the transfer takes place, is well-visible with its trend $S(k)^{-5/3}$. In the last part of the spectrum, the dissipation section is visible where the turbulent kinetic energy is dissipated by viscosity in the small scales range.

### 2.3.5 *Dissipation rate* $\epsilon$

Since the diffusion goes as the Laplacian of velocity, the dissipation rate may be evaluated in terms of the energy spectrum:

$$\epsilon = 2\nu \int_0^{inf} k^2 S(k)dk \tag{2.44}$$

Looking at figures, 2.18 , 2.19 and 2.20, the dissipation $\epsilon$ in the three directions is compared with the results of (Vreman and Kuerten, 2014a). While in

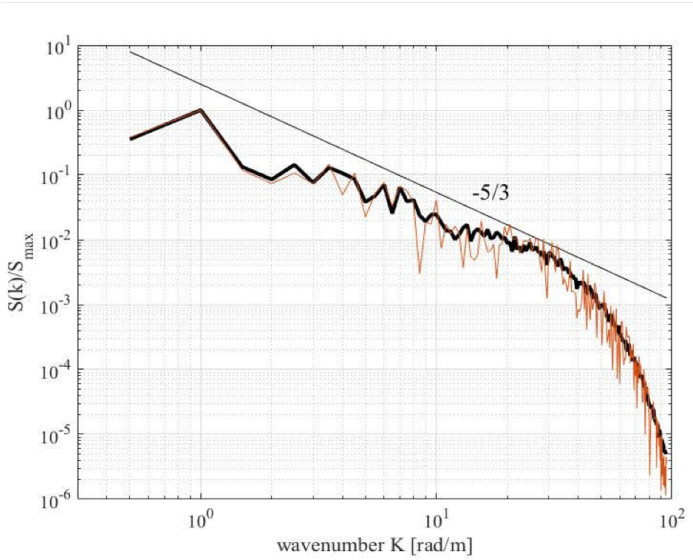


Figure 2.17: Energy cascade in the energy spectrum of turbulence of streamwise velocity

streamwise and spanwise there is a total agreement, a discrepancy is present in the wall normal direction. This may be due differences of the computational domain of (Vreman and Kuerten, 2014a). Their channel's dimensions are $4\pi \times 2 \times 4/3\pi$ and in the wall normal direction has the doubled number of points with a tangent hyperbolic function of the points stretching.

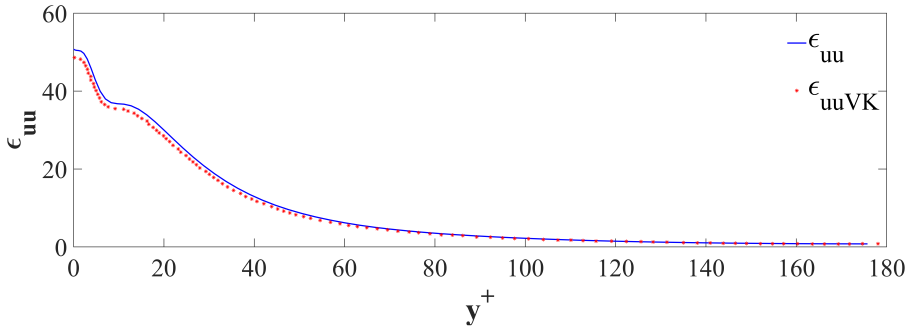


Figure 2.18: Component of the dissipation $\epsilon_u$. Comparison with (Vreman and Kuerten, 2014a) results.

## 2.4 CONCLUSIONS

Two numerical simulations of turbulent channel flow at $Re_\tau = 180$ were carried out compared with results obtained by spectral codes that are more accurate with the same grid. The comparison of the statistical quantities with the numer-

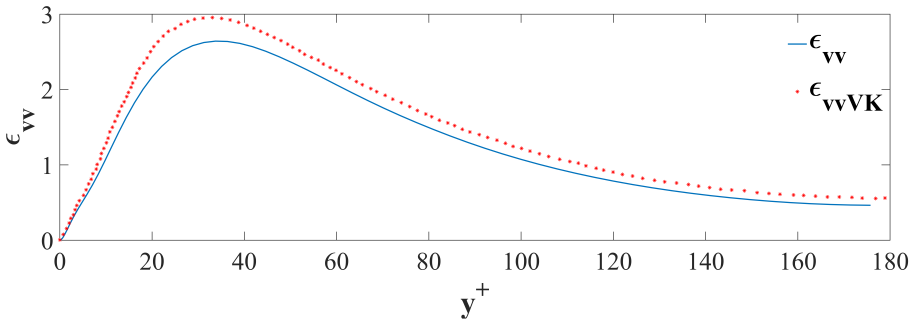


Figure 2.19: Component of the dissipation $\epsilon_v$. Comparison with (Vreman and Kuerten, 2014a) results.

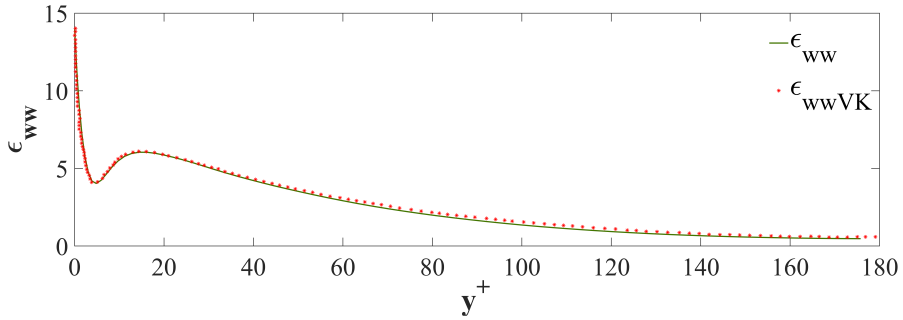


Figure 2.20: Component of the dissipation $\epsilon_w$. Comparison with (Vreman and Kuerten, 2014a) results.

ical and experimental results is satisfying. In order to increase the Reynolds number this code will be probably prohibitive caused by computational efforts for the available power.

# 3

# ON THE SYMMETRY OF PLANAR VORTICES

To introduce the concept of symmetry reduction, two discrete systems of planar (2D) inviscid vortices were taken into account, in particular i) leapfrogging vortices (Péntek et al. (1995); Shashikanth and Marsden (2003)) and ii) rotating planar vortices (Hernández-Garduño and Shashikanth, 2018). The Hamiltonian structure of the vortex dynamic equations can be exploited to desymmetrize the vortical motion. In fluid dynamics a vortex is a region where flow, or somethings that behaves as a fluid, turns around an axis line or a point in the case of spherical vortices. In nature is not so difficult to observe vortices, indeed they surround us. Sink vortex, tropical cyclone, tornado or dust devil, wingtip vortices of a airplane and whirlpools of the boat's wake and smoke rings are the most famous. Without being in conditions of turbulent flows, vortices are present in the wake behind bodies: interesting the atmospheric vortices flow past an island. Harder to see photon, electromagnetic and optical vortices as the mega cyclone on Jupiter planet. Vortices can be found in plants and animal reign in the form of plant's leaf, in a shell shape or in the way animals behave as schooling fishes or flock of birds.

Scientists recently discovered ring bubbles vortices of dolphins and belugas as way to play together (Burghardt (2005), Delfour and Aulagnier (1997), Jones and Kuczaj (2014)) and used to communicate each other (McCowan et al. (2000),Marten et al. (1996), Moreno and Macgregor (2019)) and in this video. Humpback whales use cylindrical ring of bubble-netting around the pray hunted (Friedlaender et al., 2011).

## 3.1 VORTEX AS A CAT AND A DANCER

Two physical examples, falling down cat and rotating dancer, are presented to introduce one of the main aspects of vortex motion, revealed by the symmetry reduction. The falling down cat is a problem that has interested scientists since the ancient times. Starting with R. Cartesio (1596-1650), it was studied by J.C. Maxwell (1831-79) and Sir. G. Stokes (1819-1903) but it remained unsolved since it was considered as a rigid body problem. A more rigorous study was conducted in 1984 by L. Lecornu and Étienne-Jules Marey that applied

Figure 3.1: Nature vortices

chronophotography to capture the cat's descent on film (Marey, 1894). The two physiologists G.G.J Rademaker and J.W.G. ter Braak in 1935 demonstrated that the secrets of the cat's reflexes consist of its capability of body deformation of bending and twisting. These 'blend and twist' give the cat the capability of flipping by 180° (Gerritsen and Kuipers, 1979). In the 1960s astronauts were trained to imitate the movements and twists of the cat in a vacuum.

While falling, the cat is safe because it can change its shape. But how do this shape-changing and rotation help the cat? It is able to right itself, as it falls, landing on its feet, irrespective of its initial orientation. The answer is in the conservation of angular moment:

$$L(t) = I(t)\omega(t) = 0 \tag{3.1}$$

There are stages as in figure 3.5b:

- Fist stage: Folding up - Both parts are moving in opposite directions $L = 0$
- Second stage: Flips - Each half in opposite directions $L = L_{back} + L_{front} = 0$
- Third stage: Unfold — same reason as the first stage $L = 0$

There are no external moments but only the gravitation force applied on its center of mass that doesn't produce a moment and remain fix on the vertical direction as show in figure 3.6 and in this video. As a direct consequence of the

Figure 3.2: Nature vortices

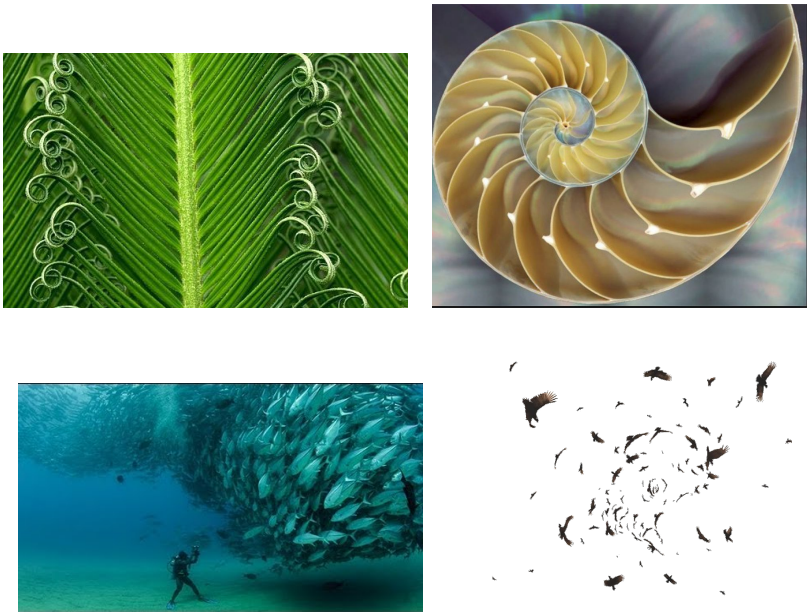

Figure 3.3: Nature vortices


Figure 3.4: Cetaceans vortices

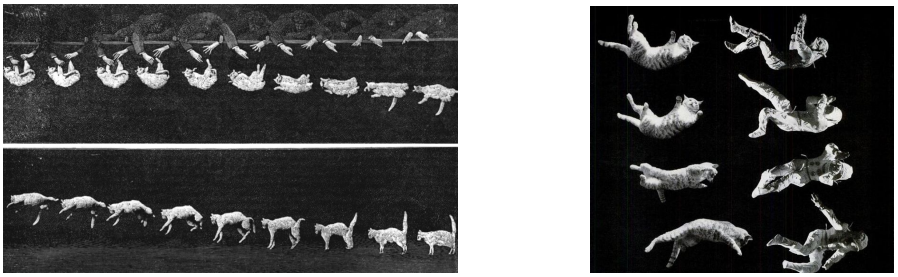

(a) Falling Cat Marey's images.

(b) Astronauts training in cat falling down

Figure 3.5: Falling cat images. In 3.5a the image was captured by a chronophotographic gun, a device of Marey's own invention. It appeared in the journal Nature in 1894 (Marey, 1894)

conservation of the angular moment, inertial moments $I(t)$, directly connected with its shape, and rotation velocity needs to change in time.

This is the same physical problem of the a spinning ballet dancer, as in figure 3.7, where the conservation of angular momentum, let him use his shape changing to increase his rotational speed, counteracting the frictional force. Thus, if the angular momentum is conserved, then the shape-changing produces a motion of the cat or dancer. This also holds for discrete systems of vortices.

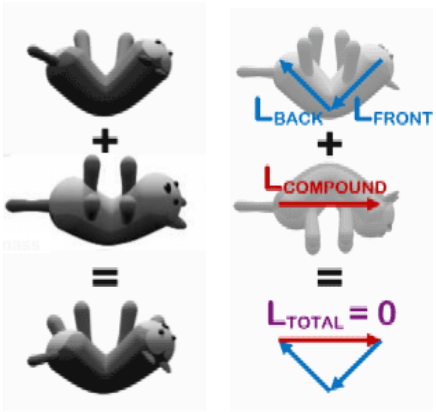


Figure 3.6: Cat falling down problem: decomposition of angular momentum L during the motion

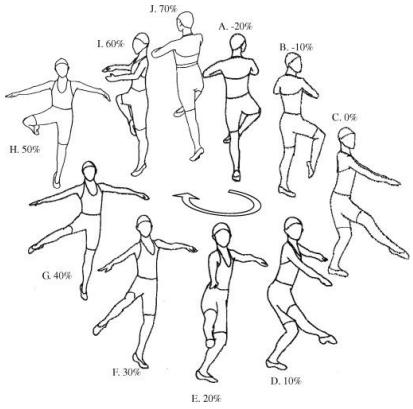


Figure 3.7: Spinning ballet dancer rotation

## 3.2 PLANAR VORTICES: HAMILTONIAN THEORY

The motion of a discrete set of planar vortices was revised. The present study reveals the pure shape-changing motion of vortices by exploiting their symmetry. Similarly to the motion of a jellyfish or swimmer, in absence of inertia the motion of vortices is uniquely determined by their shape-changing over time (Shapere and Wilczek, 1989). From a dynamical system perspective, if a translational or rotational symmetry exists, it must be used to reveals the self-induced vortical motion. In particular, the velocity $\mathbf{V}$ of each vortex is given by the sum of dynamical and geometric components:

$$\mathbf{V} = \mathbf{V}_{geometric} + \mathbf{V}_{dynamic} \tag{3.2}$$

In simple terms, the dynamic velocity is due to the inertia of vortices and to external forces. On the other hand, the added geometric velocity of a vortex is due

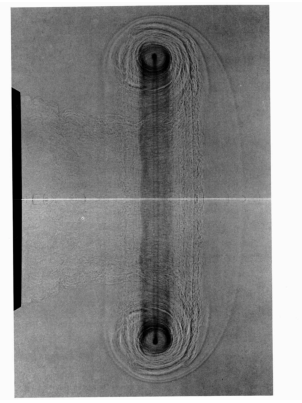

Figure 3.8: Vortex ring (Van Dyke and Van, 1982)

to the shape-changing motion caused by the interaction with the non uniform local flow ( e.g a second nearby vortex). As an application, a discrete system of planar (2D) inviscid vortex rings is considered, in particular leapfrogging vortices with null circulation (Péntek et al. (1995), Shashikanth and Marsden (2003)) and rotating vortices having non-vanishing circulation (Hernández-Garduño and Shashikanth, 2018).
The Hamiltonian structure of the vortex dynamic equations is used for a symplectic reduction of the associated symmetries, thus revealing the hidden motion induced by the shape-changing evolution of vortices. The kind of symmetry is different for the two considered discrete system of vortex rings. In particular, leapfrogging vortices have translational $T(1)$ symmetry whereas the non-zero circulation vortex system has rotational $U(1)$ symmetry. The Hamiltonian structure of the vortex dynamic equations can be exploited to desymmetrize the vortical motion as follows.

### 3.2.1 *Leapfrogging vortices*

The translational symmetry of leapfrogging vortices implies that if $\Psi(x, y, t)$ is the associated stream-function solution, so is $\Psi(x + L, y, t)$ for any $L$ shift along $x$. As a result, if $(x_k(t), y_k(t))$ is the coordinate position of the $k$-th point vortex, another admissible position is $(x(t) + L, y(t))$. Each vortex ring consists of a pair of contra-rotating point vortices with the same strength (figure 3.10a). Thus, the total circulation $\sum \Gamma_k = 0$, where $\Gamma_k$ is the vortical strength of each point vortex. In the absence of viscosity and external forces, an isolated vortex ring just advects without changing its shape as shown in figure 3.8, which depicts famous fluid dynamic photos of (Van Dyke and Van, 1982). However, in case of leapfrogging vortices, each vortex motion is affected by the flow induced by the presence of the other surrounding vortices. Assume the vortex rings travel along the axis $x$ as shown in figure 3.9.

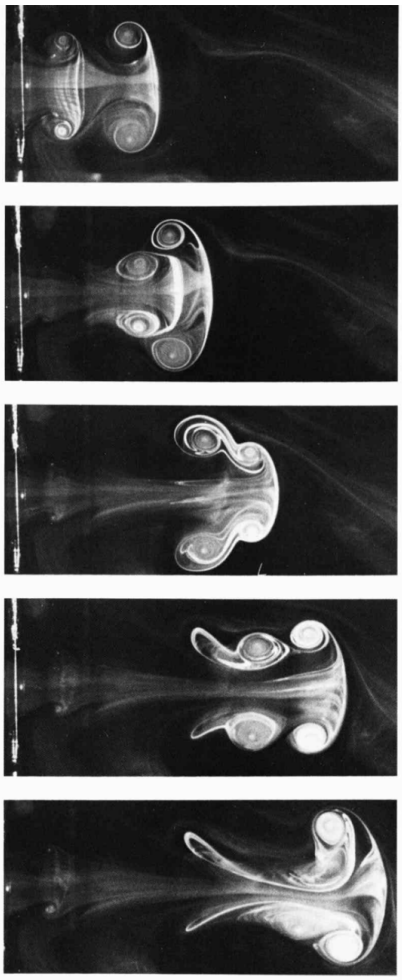

Figure 3.9: Leapfrogging vortices by (Van Dyke and Van, 1982)

The Hamiltonian of the system is:

$$\mathbf{H}(x_i, y_i) = \frac{1}{4\pi} \sum_{i \neq j} \Gamma_i \Gamma_j \log \|x_i - x_j\| \tag{3.3}$$

where the canonical variables $(x_1, y_1, x_2, y_2)$ make a phase space in $\mathbb{R}^4$, and the equations of motion follow as

$$\begin{cases} \Gamma_i \dot{x_i} = \frac{\partial H}{\partial y_i} \\ \Gamma_i \dot{y_i} = -\frac{\partial H}{\partial x_i}, \end{cases} \tag{3.4}$$

and $i = 1, 2$. See also Appendix A for a review of the Hamiltonian theory.

The two vortex rings alternatively leapfrogs each other, while advecting downstream as shown in this video. Advection is caused by the flow generated by each vortex (dynamical velocity) and that induced by the changing topology

of vortices, due to the mutual interaction with the other vortices (geometric phase velocity).

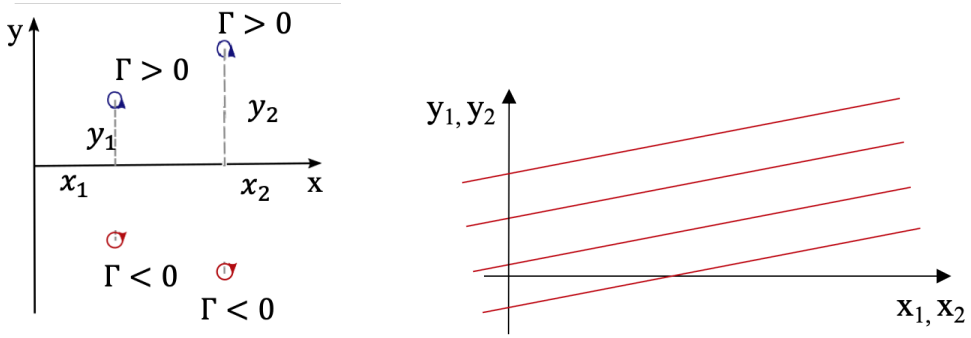


(a) Geometry of Leapfrogging vortices

(b) Hyperplanes in phase space

Figure 3.10: Leapfrogging vortices representation

The Hamiltonian in equation 3.3 is invariant to rotations and then it gives the following first integrals of motion:

$$\begin{cases} L = \sum_k \Gamma_k \|\mathbf{x_k}\|^2 \\ M_x = \sum_k \Gamma_k x_k \\ M_y = \sum_k \Gamma_k y_k \end{cases} \tag{3.5}$$

expressing, the conservation of angular momentum L and linear momentum $M = (M_x, M_y)$ on the plane, where $\|\mathbf{x_k}\|$ represent the magnitude of $x_k$. Conservation of momentum allows to remove one degree of freedom, reducing the phase space $\mathbb{R}^4$ to $\mathbb{R}^3$. In particular,:

$$\begin{cases} L = \sum_k \Gamma_k \|\mathbf{x_k}\|^2 = 0 \\ M_x = \sum_k \Gamma_k x_k = 0 \\ M_y = \sum_k \Gamma_k y_k = 2\Gamma(y_1 + y_2) = cost \end{cases} \tag{3.6}$$

Since $\Gamma_1 = -\Gamma_2$, $M_y = y_1 + y_2$. New canonical variables can be defined as follows. Consider the absolute "centre-of-mass" coordinates

$$\begin{cases} x_0 = \frac{1}{2}(x_1 + x_2) \\ y_0 = \frac{1}{2}(y_1 + y_2), \end{cases} \tag{3.7}$$

and the relative (to the centre of mass) variables

$$\begin{cases} x_r = x_2 - x_1 \\ y_r = y_2 - y_1. \end{cases} \tag{3.8}$$

The variable $y_0$ is an invariant of the system because of the conservation of the momentum $M_y$ from Eq. 3.6. So, the degrees of freedom are now $(x_1, x_r, y_r)$

and the dynamics is in $\mathbb{R}^3$. Note that the triplet $(x_2, x_r, y_r)$ or $(x_0, x_r, y_r)$ is a possible choice among others. Furthermore, the reduction of translational symmetry is attained by choosing a reference system that moves together with the first vortex. This further coordinate change permits to reduce the dimension of the state space from $\mathbb{R}^3$ to $\mathbb{R}^2$ by selecting one of the hyper-planes (leaves) in the full phase space shown in figure 3.10b and governed by the equation 3.7. Using the *"jargon"* of differential geometry, the 3-D space $(x_1, x_r, y_r)$ is the *"fiber bundle"*: the reduced 2-D space $(x_r, y_r)$ is called *"base manifold"*, a plane where the pure dynamics due to the shape-changing of vortices is projected and 1-D space $x_1$ makes *"fibers"*, the geometric representation of the symmetry. In simple terms, an observer moves together with the first vortex to watch the relative interaction with the other vortex. The variables $x_r$ and $y_r$ are canonically conjugate and the associated Hamiltonian is

$$H = \frac{1}{2}\ln\frac{(x_r^2 + 4y_0^2)(4y_0^2 - y_r^2)}{x_r^2 + y_r^2}. \tag{3.9}$$

Note that $H$ depends neither on $x_1, x_2$, nor on $x_0$. The horizontal velocity $\dot{x}_1$ of the first vortex can be split in the sum of a dynamical velocity $\dot{x}_d$ and a geometrical velocity $\dot{x}_g$, that is

$$\dot{x}_1 = \dot{x}_d + \dot{x}_g = \dot{x}_d + (\dot{x}_1 - \dot{x}_d). \tag{3.10}$$

There is no unique definition of the dynamical $\dot{x}_d$. In this case we choose it as the velocity of the centroid of the vortex system. This form yields to a symplectic definition of the geometric component $\dot{x}_g$, i.e. the area spanned by the orbit of the dynamics on the shape manifold $(x_r, y_r)$ as shown in figure 3.11 (See Shashikanth and Marsden (2003)). In particular, the dynamical phase velocity

$$\dot{x}_d = \frac{y_1\dot{x}_1 + y_2\dot{x}_2}{y_1 + y_2} \tag{3.11}$$

and from Eq. 3.10 the geometric phase velocity

$$\dot{x}_g = \dot{x}_1 - \dot{x}_d = -\frac{2y_0 + y_r}{2}\frac{\dot{x}_r}{2y_0}, \tag{3.12}$$

which simplifies to

$$\dot{x}_g = -\frac{\dot{x_r}}{2}\left(1 + \frac{y_r}{2y_0}\right). \tag{3.13}$$

Then, the geometric phase $x_g$ associated with the orbit or path $\gamma$ on the shape manifold is

$$x_g = \int_0^t \dot{x}_g dt = \frac{1}{4y_0}\oint_\gamma y_r dx_r = -\frac{Area_\gamma}{4y_0}. \tag{3.14}$$

Thus, the geometric phase is proportional to the area spanned by the orbit $\gamma$ on the shape manifold. Figure 3.11 depicts the contour levels of the Hamiltonian

in the *symplectic shape manifold* $(x_r, y_r)$. If $\gamma_i$ are the elliptic orbits, or contour levels of H, then the geometric phase associated with each orbit or configuration is proportional to the area spanned by the same orbit.

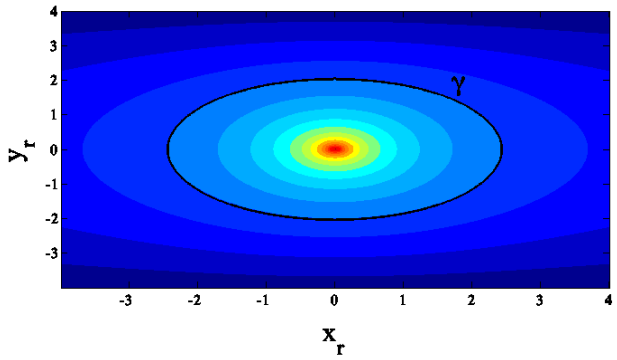


Figure 3.11: Base manifold in the relative coordinates $(x_r, y_r)$: contour levels of the Hamiltonian function.

The motion of the leapfrogging vortices were simulated in MATLAB by solving numerically the above mentioned equations. Two vortices are shown in figure 3.12 and video in the lab frame, whereas in the desymmetrized frame in the figure 3.13 and in the following videos. The symmetry was removed placing the coordinate system once on the center of mass of the vortices system in video n 1 and the other centered on a vortex in the video n 2 .

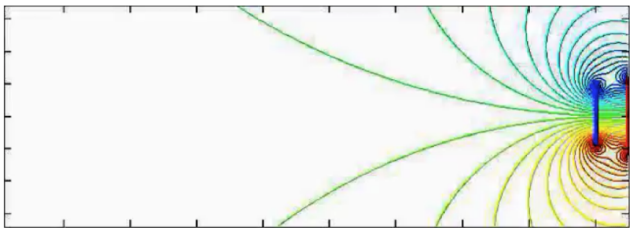

Figure 3.12: Two Leap Frogging vortices in Lab frame

In this video it is shown the motion of three leapfrogging vortices in the desymmetrized frame. Each vortex is located at the corners of a deforming triangle. The shape-changing of the vortices is given by the deformation of the triangles.

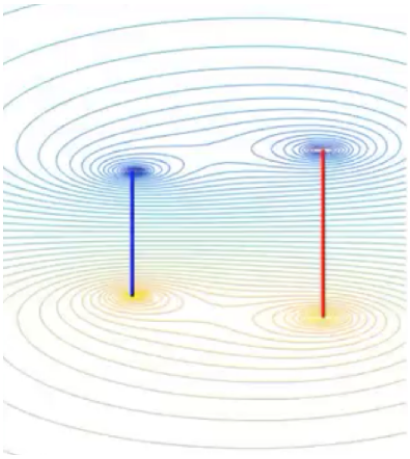

Figure 3.13: Two Leap Frogging vortices in desymmetrized frame

### 3.2.2 *Planar vortices*

Figure 3.14: Planar vortices scheme

Consider a planar system of N vortices that have the same value of circulation $\Gamma_k$ and $\sum \Gamma_k \neq 0$. Vortices are located at the vertices of a polygon. In absence of viscosity and external forces, an isolated ($N = 1$) vortex does not advect. For $N > 1$ vortices, the velocity of each point vortex is induced by the mutual flow generated by the other vortices. In simple terms, the vortex system as a whole advects while rotating around the 'centre of mass' of the vortices. To see this, consider the associated Hamiltonian from Eq. (3.5) written in complex form (Chorin et al. (1990)). Define the complex variable $z_\alpha = x_\alpha + iy_\alpha$ and the equations of motion of the N vortices follow as (Aref, 2007):

$$\begin{cases} \dot{z}_\alpha = \frac{\partial H}{\partial \overline{z}_\alpha} \\ \dot{\overline{z}}_\alpha = -\frac{\partial H}{\partial z_\alpha} \end{cases} \tag{3.15}$$

where $\partial\overline{z_\alpha}$ is the complex conjugate. Such dynamical system admits the so-called $U(1)$ symmetry associated with the conservation of angular momentum,

i.e. if $z_\alpha$ is a solution, so is $z_\alpha e^{i\theta}$ for any phase $\theta$. Vortices are free to rotate around the "center of mass" $z_c = \sum \Gamma_k \, z_k / \sum \Gamma_k$. A coordinate is made and a reference system moving with $z_c$ chosen, $z$ changed to $z - z_c$. The $U(1)$ symmetry can be quotiented out by reducing the dynamics onto a complex projective space $CP^n$, where we can describe the pure shape-changing motion of the vortices.

The motion of N vortices can be understood geometrically in a complex state space $\mathbb{C}^N$, which is isomorphic to $\mathbb{R}^{2N}$. Consider identical vortex strengths, i.e. $\Gamma_k = \Gamma$ for any k. Then, conservation of angular momentum constraints the dynamical orbits on a complex N-sphere

$$|z_1|^2 + |z_2|^2 + .....|z_N|^2 = 1, \tag{3.16}$$

where $z_k = x_k + ix_k$. For $N = 2$ the 2-sphere in $\mathbb{R}^4$ can be fibrated ala Hopf (Hopf (1930), Hopf (1935)) as a 1-sphere (base manifold) of $\mathbb{R}^3$ and 1-dimensional circular fibers attached to any point of base manifold, as shown in Figure 3.15. Thus, a dynamical orbit can be decomposed into a desymmetrized orbit on the base manifold and a drift along the fibers.

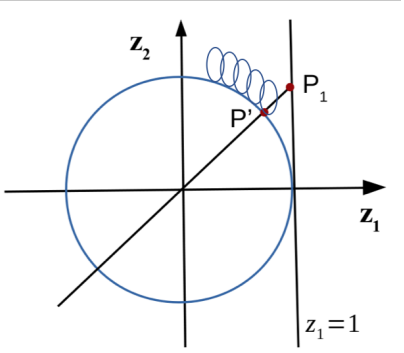


Figure 3.15: Schematization of complex projective space $CP^n$

A reduction map $\pi$, that is invariant under $U(1)$ symmetry, takes a full orbit and reduces it onto the base manifold. This can be represented by a chart shown in figure 3.15 made of the complex plane $z_1 = 1$. Then, $\pi$ takes the 1-D fiber attached to a point $P'$ of the sphere and reduce it to a point $P_1$ on the chart. The fiber is given by

$$z_2 = \lambda z_1 \tag{3.17}$$

where $\lambda = e^{i\alpha}$ is the symmetry parameter that is:

$$(z_1, z_2) \xrightarrow{\pi} \left(1, \frac{z_2}{z_1}\right) \tag{3.18}$$

Varying the value of $\lambda$, all the points of the sphere and their attached fibers are reduced on the complex plane and the symmetry is removed. In fact, points

$P'$ and $P_1$ belongs to the same equivalent class made by the fibers. In physical space, this is equivalent to choosing a reference frame moving on top of the first vortex. For $N > 2$, the map $\Pi$ generalized to:

$$(z_1, z_2 ... z_N) \xrightarrow{\pi} \left(1, \frac{z_2}{z_1} ... \frac{z_N}{z_1}\right) \tag{3.19}$$

As an application consider a system of 3 vortices ($N = 3$).

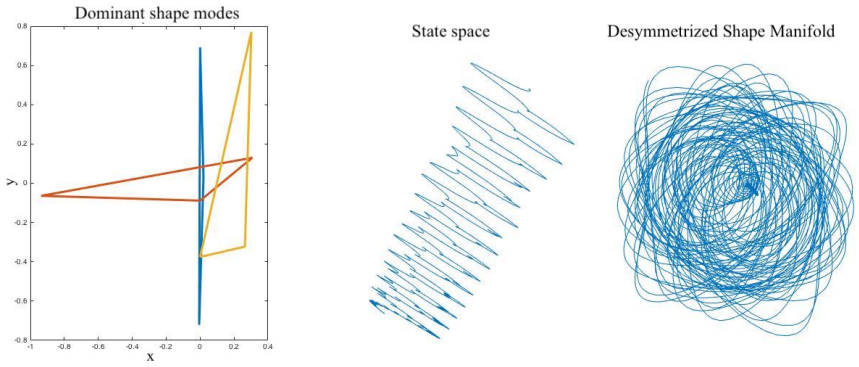


Figure 3.16: 3-vortex system

The left panel of figure 3.16 depicts the vortex system. Note that Liouville's theorem guarantees integrability of the N-vortex system problem for $N \leqslant 3$ (Aref (2007)). The trajectory or orbit in the full phase space appears to drift as it wanders around. Such drift is due to the $U(1)$ symmetry. Once symmetry is reduced, the desymmetrized orbit on the shape manifold has no drift and it appears quasi-periodic as it wanders on a torus typical of Hamiltonian systems. The left panel of the same figure 3.16 shows the dominant shape modes, obtained by Proper Orthogonal Decomposition (POD), of the desymmetrized vortex motion. It is an eigenvalue problem and it has been used to extract mode shapes. A review of POD theory is in Appendix B. In this particular case, POD reveals how the three vortices move with respect to each other in physical space in accord with a revealed dance choreography. The polygon, the triangle, connecting the point vortices deforms in time and they represents three different POD modes. Moreover, an 'elastic energy' can be associated with those deformations. Such elastic motion on the base manifold is hidden by the symmetry since it confuses together with the induced drift (rigid rotation) along the fibers. Once symmetry is removed the 'elasticity' of vortices is revealed. The dynamical velocity can be defined as the velocity of the frozen vortices as if the whole vorticity is concentrated in a fixed point. The same procedure was applied on a system of 4-Vortex which dynamics in Lab Frame and Hopf-Stereo Frame are shown in this video

## 3.3 CONCLUSION

Two different systems of planar vortices were studied in order to introduce and understand the concepts at the base of the symmetry reduction method. The simplicity of these discrete systems is in their Hamiltonian formulation that permits to reduced the symmetry and reveals how vortices interaction and their shape changing influence their motion.

# 4

# SYMMETRY REDUCTION METHOD

## 4.1 INTRODUCTION

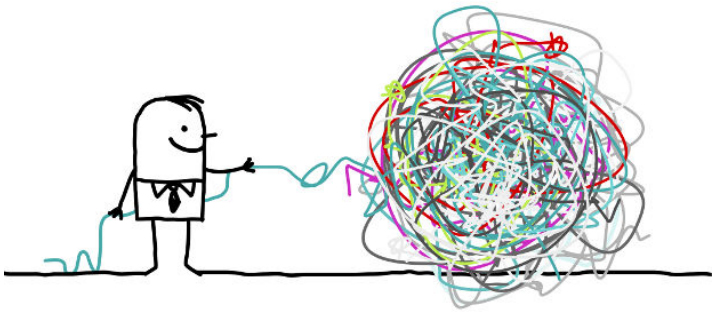

Figure 4.1: Schematization of a non linear dynamic system in Fourier domain

A turbulent channel flow can be seen as a generic chaotic dynamical system, governed by the NS equations:

$$\begin{cases} \nabla \cdot \mathbf{u} = 0 \\ \frac{\partial u}{\partial t} + (\mathbf{u} \cdot \nabla)\mathbf{u} = -\frac{\nabla p}{\rho} + \mu \nabla^2 \mathbf{u} + f \end{cases} \tag{4.1}$$

The physical space is $\mathbf{R}^3$. In "Chaos theory", this nonlinear dynamic system is studied in the "state space representation". It is a mathematical model of a physical system as a set of input, output and state variables related to the differential equations. The state space is an Euclidean space in which the variables on the axes are the state variables while the state of the system is represented as a vector within that space. State variables are variables whose values evolve over time in a way that depends on the values they assume at any given time and on the externally imposed values of input variables. Output variables values depend on the values of the state variables. The reason why it works in state space is that what happens in physical space sometimes is not always suggestive of the hidden laws of physics of the turbulent motion. In fact sometimes a dynamic system can seem chaotic in physical space while in

reality it is a sum of exact solutions and its behaviour in state space follows a periodic path called *orbit*. Indeed, " Writing about turbulence is a bit like writing about a ballet without seeing any" (Cvitanović and Gibson (2010)). It also clear in this video, where an apparent chaotic flow, in state space appear ordered following a periodic orbit. On the other hand, a symmetry reduction method approach allows to visualize a chaotic dynamics in physical space as a high-dimensional system in state space (Fedele et al., 2015) but with a more "ordinate" structure. It is not easy to visualize and interpret it and, at first sight, it can be seen as a ball of threads as shown in figure 4.1 .

## 4.2 DYNAMICAL SYSTEM GOVERNED BY A PDE

To introduce the methodology, consider the 1D linear advection equation

$$\frac{\partial u}{\partial t} + c\frac{\partial u}{\partial x} = 0 \tag{4.2}$$

with $c = 1m/s$. It is a partial differential equation (PDE) and it describes a linear dynamical system. The solution is unique if initial conditions and boundary conditions are defined unequally. The initial condition (IC) is a space function $f(x)$ and the boundary condition (BC) is periodic as in the following:

$$u(x, 0) = f(x) \tag{4.3}$$

$$u(-L, t) = u(L, t) \tag{4.4}$$

with L the length of the domain.

### 4.2.1 *Fourier space representation*

In order to move in state space, the general solution $u(x, t)$ can be expressed in the discrete Fourier domain through the discrete Fourier transform:

$$z_n(t) = \frac{1}{L}\sum_{-L/2}^{L/2} u(x, t)e^{-ik_0 nx} \tag{4.5}$$

Assuming $u(x, t)$ as real function, its complex conjugate is:

$$\overline{z_n}(t) = \frac{1}{L}\sum_{-L/2}^{L/2} \overline{u(x, t)}e^{+ik_0 nx} = \frac{1}{L}\sum_{-L/2}^{L/2} u(x, t)e^{-ik_0(-n)x} = z_{-n} \tag{4.6}$$

with $z_n$ are Fourier modes, N the number of modes, $n \in [-N, N]$, $k_0 = \frac{2\pi}{L}$ the smallest wave number and L the domain length. Doing the inverse Fourier transformation, it's possible to come back to the physical space:

$$u(x,t) = \sum_{-N/2}^{N/2} z_n(t) e^{ik_0 nx} \tag{4.7}$$

Applying the Fourier transform, the wave equation can be written as below:

$$\sum_{-N/2}^{N/2} \left(\frac{\partial u}{\partial t} + \frac{\partial u}{\partial x}\right) e^{-ik_0 nx} = 0 \tag{4.8}$$

In order to obtain the equation written in Fourier domain, one of the methods available consists of the scalar product method that assumes the meaning of a projection on the Fourier space functions (see also Appendix C ) that is:

$$\left\langle \left(\frac{\partial u}{\partial t} + \frac{\partial u}{\partial x}\right), e^{-ik_0 mx} \right\rangle = 0 \tag{4.9}$$

with $< \cdot >$ denotes the scalar product where the 4.7 was taken in account

$$\left\langle \left(\frac{\partial}{\partial t} \sum_{-N/2}^{N/2} z_n(t) e^{ik_0 nx} + \frac{\partial}{\partial x} \sum_{-N/2}^{N/2} z_n(t) e^{ik_0 nx}\right), e^{-ik_0 mx} \right\rangle = 0 \tag{4.10}$$

Performing time and space derivatives steps:

$$\left\langle \left(\sum_{-N/2}^{N/2} \dot{z}_n(t) e^{ik_0 nx} + \sum_{-N/2}^{N/2} ik_0 n z_n(t) e^{ik_0 nx}\right), e^{-ik_0 mx} \right\rangle = 0 \tag{4.11}$$

$$\left\langle \left(\sum_{-N/2}^{N/2} \left(\dot{z}_n(t) + ik_0 n z_n(t)\right) e^{ik_0 nx}\right), e^{-ik_0 mx} \right\rangle = 0 \tag{4.12}$$

$$\sum_{-N/2}^{N/2} \left\langle \left(\dot{z}_n(t) + ik_0 n z_n(t)\right) e^{ik_0 nx}, e^{-ik_0 mx} \right\rangle = 0 \tag{4.13}$$

$$\sum_{-N/2}^{N/2} \left(\dot{z}_n(t) + ik_0 n z_n(t)\right) \left\langle e^{ik_0 nx}, e^{-ik_0 mx} \right\rangle = 0 \tag{4.14}$$

$$\sum_{-N/2}^{N/2} \left(\dot{z}_n(t) + ik_0 n z_n(t)\right) \delta_{nml} = 0 \qquad \forall m \tag{4.15}$$

and the last equation is different than a trivial identity 0=0 only if $n = m$. The wave equation in Fourier domain is expressed as:

$$\dot{z}_m(t) + ik_0 m z_m(t) = 0 \qquad \forall m \in \{-N/2 \dots N/2\} \tag{4.16}$$

where $z_m$ are Fourier coefficients in the complex $\mathbb{C}$ domain assembled in a vector $z(t)$:

$$z(t) = \begin{bmatrix} z_{-N/2} \\ z_{-N/2+1} \\ \vdots \\ z_{-2} \\ z_{-1} \\ z_0 \\ z_1 \\ z_{-2} \\ \vdots \\ z_{N/2} \end{bmatrix} \tag{4.17}$$

The dynamical equation can also be written more compactly as :

$$\dot{z}(t) = F(z) \tag{4.18}$$

where $F(z)$ is a linear function of $z$:

where the vector $F(z)$:

$$F(t) = \begin{bmatrix} F_{-N} \\ F_{-N+1} \\ \vdots \\ F_{-2} \\ F_{-1} \\ F_0 \\ F_1 \\ F_{-2} \\ \vdots \\ F_N \end{bmatrix} \tag{4.19}$$

whose components $F_m(z) = -ik_0 m z_m$

### 4.2.2 *The geometry of chaos*

From a visual interpretation, $z(t)$ a trajectory, that moves in high-dimensional complex space as a function of time, whose n components belong to the vector in equation 4.17 . This dissertation does not claim to study dynamical system stability but its geometric representation and concepts necessary to understand

the geometry of chaos. In the state space there are several geometric entities that create the portrait of the dynamic system: stable and unstable equilibrium points, stable and unstable periodic orbits (circular or more complicated curves) that are invariant solution and manifolds (lines or curves that start and finish from equilibrium points and moves in state space). The trajectory $z_n(t)$ describes the behaviour of the dynamical system moving through these geometric entities. The set of invariant solution and the unstable manifold built a rigid structure of the state space that arrange the system dynamics (Cvitanović and Gibson, 2010).

## 4.3 DYNAMICAL SYSTEM WITH SYMMETRIES: WHEN DOES THE SYMMETRY EXIST?

Taking into account a non-linear dynamical system, passing from physical space to state space, its treatment becomes apparently more complicated. While in physical space is possible to visualize all the system evolving in time, the same procedure is not possible in state space. This is cause by the fact that human beings have experience of the physical world and understand it as the motion of a particle in three-dimensional space and time. On the other hand, the system in state space is a complex high dimensional space that our mind cannot easily figure out. In a dynamical system the degree of freedom coincides with the numbers of parameters that may vary independently. Taking into account the Navier Stokes equation in the continuum space and time, DOFa are 4 : the three components of velocity $\vec{u}(x, y, z, t)$ and the pressure $p(x, y, z, t)$. The system is defined in $\mathbf{R}^4$. In a discrete situation, as a numerical simulation, the DOFs are equal to the number of the grid points where velocity and pressure are defined. In this case the system has a dimension equal to $\mathbf{R}^{4N}$. Despite the size of the system, its visualization is understandable. Taking for example the vorticity field in the turbulent channel flow. What can be visualized is a chaotic flow that changes over time and space, with different colours. The dimension of the dynamical system in the state space is already given by the DOFs of the dynamical system. For example the number of DOFs of numerical simulation of the turbulent channel in the state space is equal to 2N the numbers of grid points that in the finest grid are $N = 10^6$. Visualize the whole system in state space is prohibitive because it is a complex high dimensional space $\mathbf{C}^N$. Only choosing a 3D subset on $\mathbf{C}^n$ it is possible to have a view of the system; but it is a subset of the system and in addition it could appear complicated similar to the figure 4.1. A way to reduce the complexity exists for some dynamical system; it is represented by a reduction of system's DOFs. In these systems, the DOF , that can be "removed", is represented by the continuous symmetry of the physical problem. It can be reduced in order to be able to observe the core of the dynamical system. As shown in the §3, planar

vortices had symmetries and the desymmetrization revealed the motion, given by the vortex shape-changing and their interaction. In mathematics the concept of continuous symmetry is provided by the Lie group. It is a symmetry group that encodes symmetry features of a geometrical object: the group consists of the set of transformations that leave the object unchanged. In particular Lie group is a continuous group: it is a group whose elements are described by real parameters and it is represented by a differentiable manifold. Lie group typically playing the role of a symmetry of a physical system such as rotational symmetry in three dimensions (given by the special orthogonal group $SO(3)$. What must be understood is the nature of 'small' transformations, for example, rotations through tiny angles, that link nearby transformations. The presence of continuous symmetries expressed via a Lie group action on a manifold places strong constraints on its geometry and facilitates analysis on the manifold. Lie groups are smooth manifolds, so have tangent spaces at each point. The most important symmetries characterized by Lie group are

- Continuous Translational symmetry=Toric group symmetry (T-Symmetry) $G_{x_0}$
- Rotational symmetry = $U(1)$ group symmetry $G_\alpha$

The $U(1)$ symmetry group $G_\alpha$ is that if $z \in \mathbf{R}^N$ is a solution of the dynamical system so is $G_\alpha = ze^{i\alpha}$. The continuous translational symmetry $G_{x_0}$ is that if $z \in \mathbf{R}^N$ is a solution of the dynamical system so is $G_{x_0(z)} = z(x + x_0)$. As will be explained better later these symmetries are represented by the fibers in the fiber boundle. In the present study the turbulent channel flow has a continuous translational symmetry and in physical space it is represented by the mean velocity that carries flow and eddies from upstream to down stream in streamwise direction. In state space this symmetry appears with a toroidal shape (T-symmetry). Removing symmetry may permit to understand how vortices change their shape and how it influences their motion. The fulcrum consists in the fact that *the desymmetrization is allowed only in the state space*.

### 4.3.1 *Dynamical system with Translation symmetries*

As mentioned previously, continuous translational symmetry has a different appearance passing from physical space to state space. It is a pure space translation in physical space and it is a Toric-symmetry (T-symmetry) in Fourier space cased by its toroidal shape as in figure 4.2

The Navier-Stokes (NS) equations are a non linear differential equation and for channel flows are dominated by continuous translational symmetry, that is if velocity field $u(x, y, z, t)$ and associated pressure field $p(x, y, z, t)$ are solutions of NS equation, so the space-shifted $u(x + \ell, y, z, t)$ and $p(x + \ell, y, z, t)$, where $\ell(t)$ is the shift, are solutions of the problem. This is true also in the state

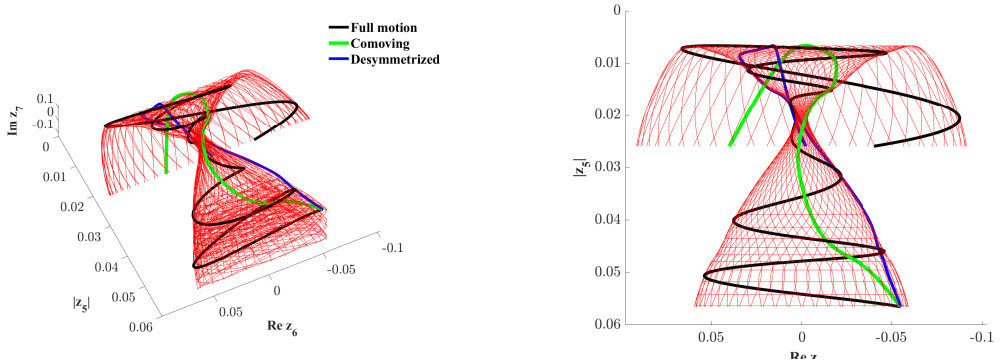


Figure 4.2: Group orbit of DNS turbulent channel flow

space where if the set $z_n$ of Fourier modes is a solution of 4.18, so is $(z_n e^{ik0\ell})$, for any shift $\ell$.

Considering again for simplicity the linear advection equation in the physical space:

$$\frac{\partial u}{\partial t} + \frac{\partial u}{\partial x} = 0 \tag{4.20}$$

A traveling wave:

$$u(x,t) = \sin(x-t) \tag{4.21}$$

is a solution of 4.20. Indeed, performing space and time derivative:

$$u_t(x,t) = -\cos(x-t) \tag{4.22}$$

$$u_x(x,t) = \cos(x-t) \tag{4.23}$$

and substituting them in equation 4.20, it yields:

$$\frac{\partial u}{\partial t} + \frac{\partial u}{\partial x} = -\cos(x-t) + \cos(x-t) = 0, \tag{4.24}$$

so equation 4.21 is a solution of the PDF in equation 4.20.
Considering the same solution shifted by a length $\ell(t)$:

$$u(x+\ell(t),t) = \sin(x+\ell(t)-t) \tag{4.25}$$

Then,

$$u_t(x+\ell(t),t) = -\cos(x+\ell(t)-t) \tag{4.26}$$

$$u_x(x+\ell(t),t) = \cos(x+\ell(t)-t)(1-\frac{d\ell(t)}{dt}) \tag{4.27}$$

$$u_t + u_x = \frac{d\ell}{dt}\cos(x + \ell(t) - t) = 0, \tag{4.28}$$

Imposing:

$$\frac{d\ell}{dt} = 0, \tag{4.29}$$

$$\ell(t) = \text{const} \tag{4.30}$$

and $\ell$ must be constant in time.
Now the solution $u(x,t)$ can be expressed as the Fourier series in the Fourier space:

$$u(x,t) = \sum_{-N/2}^{N/2} z_n(t) e^{ik_0 n x} \tag{4.31}$$

with $k_0 = 2\pi/L_0$ the wave number associated to the domain length $\ell_0$ and $z_n(t)_{n=1,N}$ are the Fourier coefficients in $\mathbb{C}^N$. The Fourier series shifted is:

$$\begin{aligned} u(x+\ell,t) &= \sum_{-N/2}^{N/2} z_n(t) e^{ik_0 n(x+\ell)} \\ &= \sum_{-N/2}^{N/2} \underbrace{(z_n(t) e^{ik_0 n \ell})}_{\tilde{z}_n(t)} e^{ik_0 n x} \\ &= \sum_{-N/2}^{N/2} \tilde{z}_n(t) e^{ik_0 n x} \end{aligned} \tag{4.32}$$

where we define:

$$\tilde{z}_n(t) = z_n(t) e^{ik_0 n \ell} = z_n(t) e^{in\alpha}. \tag{4.33}$$

Here the angle $\alpha$ is a *phase shift*

$$\alpha = k_0 \ell, \qquad -\infty \leqslant \ell \leqslant \infty \tag{4.34}$$

and

$$u(x+\ell,t) = \sum_{-N/2}^{N/2} z_n(t) e^{ik_0 n(x+\ell)} = \sum_{-N/2}^{N/2} \tilde{z}_n(t) e^{ik_0 n x} \tag{4.35}$$

is already a solution of the PDE in equation 4.20.

## 4.4 DYNAMICAL SYSTEMS

Consider a generic non linear dynamical system perspective, in the state space $\mathbf{C}^N$. The NS equations can be written in the form :

$$\frac{dz}{dt} = N(z_1, z_2, ..., z_N) \tag{4.36}$$

where $N(z)$ is a vector encoding the non linearity of the system. If $z = \{z_n(t)\}_{n=1}^N$is a solution of the dynamical system 4.36, so is $\{z_n(t)e^{in\alpha}\}$ a solution of that system, with $\alpha = k_0/L$ parameter connected with the space shift L. The translation L in the physical space becomes a phase shift in the state space. The state space $\mathbf{C}^N$ has the geometric structure of a fiber bundle. This can be imagined at first as a bamboo forest (see figure 4.3a). It is composed by the ground, where the bamboo are attached, called *base manifold*, and the bamboo sticks, called *fibers*. The fiber bundle is the geometric structure of the state space $\mathbf{C}^N$, where the continuous symmetry G, represented by the fibers, gives it a rigid backbone.

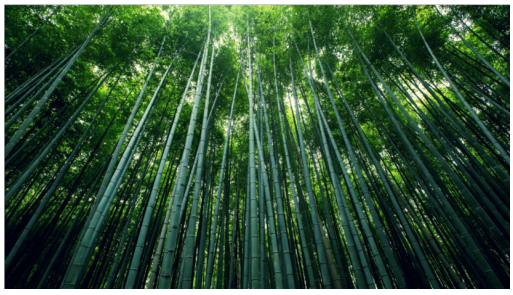

(a) Fiber bundle as a bamboo forest

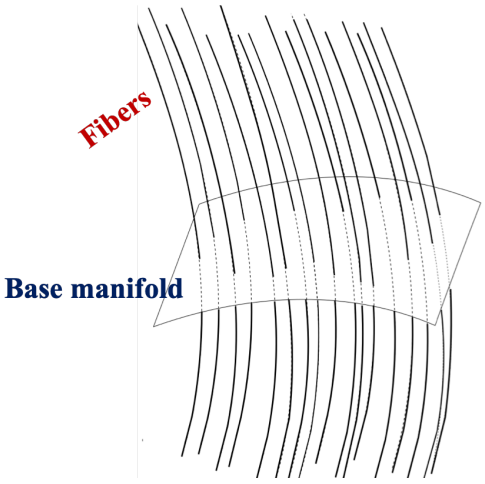


(b) Fiber bundle scheme

Properly, the fiber bundle is composed by a *base manifold* that is a complex hyperplane $B = \mathbb{C}^N|\mathbb{R}$ of dimensions $\mathbb{R}^{2N-1}$ and 1D fibers (direction of symmetry) that are attached to any point of B as depicted in figure 4.3b.

### 4.4.1 *Group orbit*

A group orbit is a subset of the fiber bundle.

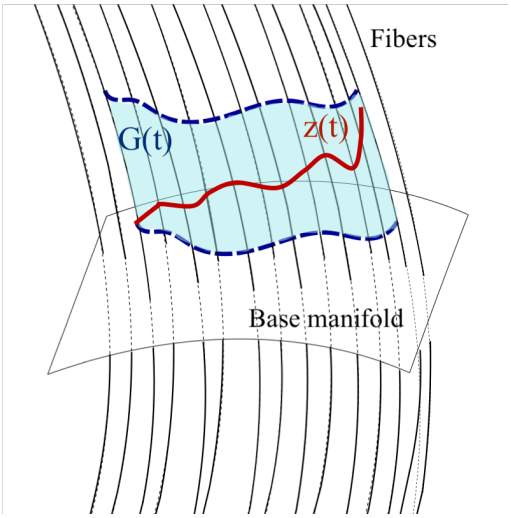


Figure 4.4: Group orbit scheme

This is defined as a sheet of the fiber bundle, as shown in figure 4.4, and it is the collection of all the shifted copies of a given solution $z(t)$ of the dynamical system, that is:

$$G(z) = \{G^{\alpha}(z(t)) \quad \forall\, \alpha \in \quad [0, 2\pi]\} \tag{4.37}$$

where, the shifted copy of $z(t)$ is:

$$G^{\alpha}(z(t)) = \{z^{\alpha}(t)\} \tag{4.38}$$

and

$$z^{\alpha} = \left\{z_n(t)e^{in\alpha}\right\} \qquad \alpha \in \mathbb{R} \tag{4.39}$$

The shift $\alpha = k_0 L$ is defined in $\mathbf{R}$ and it varies in $[0\, 2\pi]$, moving along the fibers. In order to understand easily the topological concepts it may be useful to do the reverse exercise of building a group orbit, as shown in figure 4.5. As mentioned before,it is not possible to visualize graphically the entire group orbits due to the high order dimensions of the state space. A subset of three components of the Fourier coefficients $z_n$ can be chosen as coordinate system and the trajectory expressed as a function of them as shown in figure 4.5a where $z(t)$ is the trajectory, function over time, and $\alpha$ is equal to zero over it. Fibers, that are 1D curves, has to be attached to any points of the trajectory and the fiber's shape is given by varying the value $\alpha$ as is shown in figure 4.5b. It is used to say also the trajectory is fibrated with the fibers. On the trajectory the value of $\alpha = 0$

The group orbit $G^{\alpha}$ represents the *full motion* and it is a collection of the possible solutions of the dynamical system. The *full motion* is the trajectory $z(t)$ that climbs over the fibers as in figure 4.6. As demonstrated before, if $z(t)$ is a

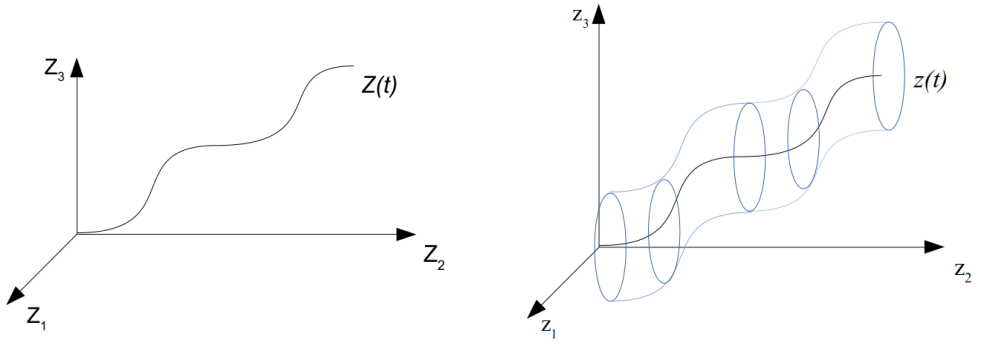


(a) Trajectory in state space

(b) Group orbits $G^{\alpha}$

Figure 4.5: Geometric construction of a group orbit $G^{\alpha}$ starting from the full trajectory z(t)

solution, so is $z(t)e^{in\alpha}$. It means that the translation, represented by the shift $\alpha$ is invariant under the symmetry of the physical problem.

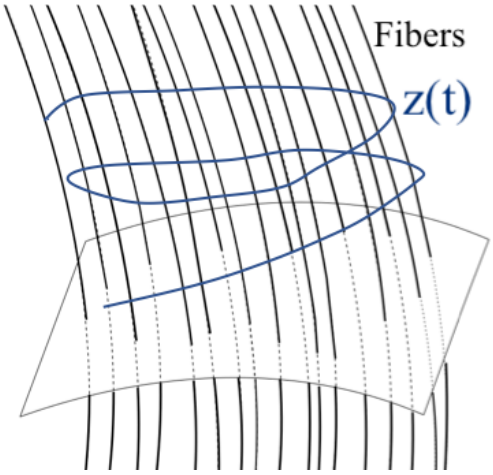


Figure 4.6: A schematic representation of a fiber bundle in state space composed the trajectory that climbs on the fibers and the base manifold.

As a consequence, the symmetry of the system is connected with the fibers, the Lie group G, function of $e^{in\alpha}$. In reality things are more complex than those schematized in the figures. The identification of the "full motion" is not possible because the entire system is a concatenation of a complicated full trajectory and fibers. Moreover, full motion inherently possesses the symmetry that is not clearly divisible by the motion due to the deformation. For this reason it is necessary to reduce the symmetry. The reduction of the symmetry means to pull out the dependence of the dynamic part connected to the symmetry and to find a "base" motion connected only with motion given by the deformation.

Given a group orbit, the tangent to the full trajectory is :

$$\dot{z}(t) = \frac{dz(t)}{dt} = F(z) \tag{4.40}$$

that is equivalent to :

$$\frac{dz_n(t)}{dt} = -nk_0 z_n(t). \tag{4.41}$$

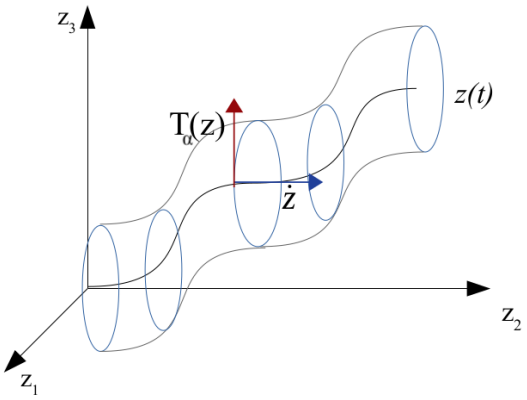


Figure 4.7: Group orbit with velocity $\dot{z}$ and tangent vector $T(z)$ depicted on it

The generic tangent $T_\alpha(z)$ to the orbits $z^\alpha(t)$ is a function of the angle $\alpha$ as shown in figure 4.8 and it is given by:

$$T_{n\alpha}(z) = \frac{\partial z^\alpha(t)}{\partial \alpha} = \left\{z_n(t) i n e^{in\alpha(t)}\right\} = in \underbrace{\left\{z_n(t) e^{in\alpha(t)}\right\}}_{z^\alpha(t)} = \{i n z^\alpha(t)\} \tag{4.42}$$

where $z^\alpha = \left\{z_n(t) e^{in\alpha(t)}\right\}$ is the full motion. If the base motion is a motion not connected with the symmetry and thus by the fibers, the full motion can be written as:

$$z_n^\alpha(t) = Z_n(t) e^{in\alpha(t)} \qquad \text{Full motion} \tag{4.43}$$

so the base motion is:

$$Z_n(t) = z_n^\alpha(t) e^{-in\alpha(t)} \qquad \text{Base motion} \tag{4.44}$$

Moving back to the tangent and posing $\alpha = 0$, the tangent to the trajectory $z(t)$ is:

$$T_{n,\alpha=0}(z) = T(Z) = \{z_n(t) i n\} \tag{4.45}$$

while the tangent along the group orbits, is:

$$T_{n\alpha}(z) = \left\{i n z_n(t) e^{in\alpha(t)}\right\}. \tag{4.46}$$

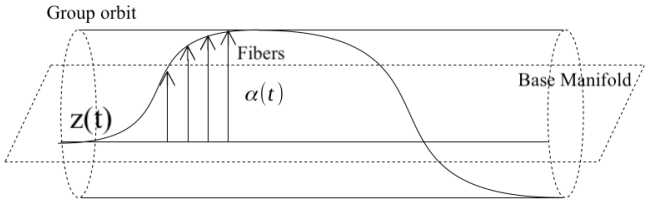


Figure 4.8: Phase shift translation of the full motion $z(t)$ as a function of the shift $\alpha(t)$

The velocity vector $\dot{z}(t)$ and $T_\alpha(z)$ and the tangent are not necessarily orthogonal. In order to remove the symmetry, the base motion should be locally transversal to the fibers as depicted in figure 4.8.

These concepts can be explained considering the example of a jellyfish motion in a current. The base motion corresponds to the motion due to the jelly's deformation, while the full motion is is due to the velocity of the current plus the translation motion induced by its deformation. The same phenomenon appears in turbulence: "The speed of coherent structures includes not only the comoving frame velocity, which accounts primarily for their inertia, but also a geometric component. This can be interpreted as a 'self-propulsion' velocity induced by the shape-changing deformations of the flow structures similar to that of a swimmer at low Reynolds numbers" (Fedele et al. (2015)).

## 4.5 PROJECTION METHODS

How can the symmetry be quotiented out? Depending on the type of symmetry, there are different methods of symmetry reduction. It depends on the symmetry and it leads to a projection problem.

Starting from the full motion $z(t)$, the symmetry reduction consists in finding a reduction map $\Pi$ that is invariant under the symmetry and maps the trajectory $z(t)$ of $\mathbb{C}^N$ on a base manifold $B$, finding the desymmetrized trajectory $Z_D(t)$. The same method may be applied on the entire group orbits $G^\alpha(z) = z_n e^{in\alpha} \longrightarrow Z_D = \pi(G^\alpha(z))$. The projection is not a reduction of the system dimension. It allows uncoupling motion due to the symmetry from the hidden dynamic motion due to a pure deformation of the flow.

A principal fiber bundle is said to be composed of a quadruplet: a total space $P \in \mathbf{R}^N$ or $\mathbf{C}^N$, the base manifold $B$, the group orbit $G^\alpha(z)$ with the parameter $\alpha \in \mathbf{R}$ and $\Pi$ the projection map. These mapping methods are a sort of parametrization of the system's variables, that removes the dependence from the symmetry of the problems. It is carried out through a projection of all the points of the group orbits on a hyper-plane. A complex geometry of the group orbit is reduced to a line or a point and the system is simplified.

### 4.5.1 *Property of the map* Π

In order to apply a projection method, the fibers have to be traversal to the base manifold, but they are not necessary to be orthogonal.

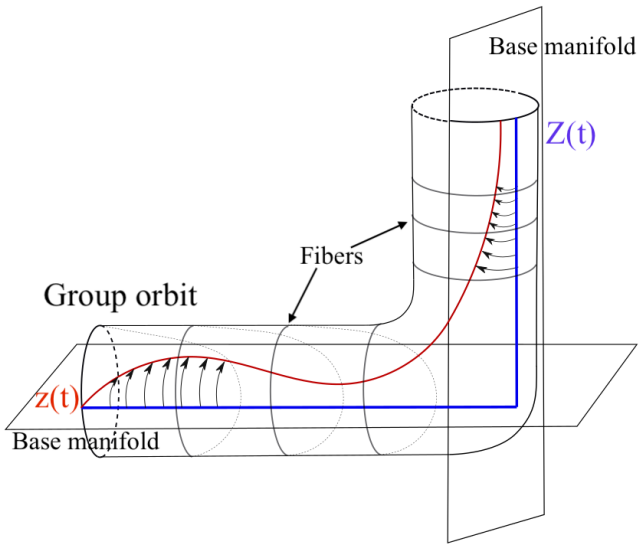


Figure 4.9: An example of geometrically complicated group orbits G(z) composed by the full motion $z(t)$ (red curve), the fibers and with more than one transversal base manifolds. The projection of the full motion $z(t)$ on the base manifolds is the desymmetrized trajectory $Z(t)$ (blue curve)

This is quite easy to understand. As shown in figure 4.9, the tube represents the entire group orbits, the red line is the full motion $z(t)$, the blue line the base motion $Z_D(t)$, the curved arrows are the fibers and there are two planes of projection. Figure 4.9 is a simplification of a real group orbit that can present more complicate geometries. Due to the different directions of fibers, the full motion has to be projected using two different hyperplanes that are two distinct base manifolds. When the direction of the fibers runs parallel to the plane of mapping, change the plane of projection becomes necessary.

Different projection methods exist and some of them will be described below. They are:

- Stereographic projection(Mercator's projection)
- Hopf reduction for U(1) and T(1) symmetries
- Fourier slice method

The map Π brings a trajectory in full space onto a base manifold, where symmetry is quotient out. The base manifold is also called the quotient space. In particular, some of the projective spaces in $\mathbb{C}$ are:

- The base manifold of a system which admits U(1) symmetry is the projective space $CP^n$ that is $CP^n+$ fibers = full space
- The base manifold of a system which admits T(1) symmetry is the projective space $TCP^n$ that is $TCP^n+$ fibers = full space.

### 4.5.2 *Stereographic projection*

In differential geometry, the stereographic projection is a particular graphical mapping function that projects a unit sphere onto a plane or a circle on a line. It is a particular case of the projective space $CP^n$ and it is useful to introduce it for being more intuitive. This method has benefits with some inevitable compromises. It maintains angles but it isn't isometric nor it preserves distances and areas. The projection is defined on the entire sphere, except at the projection point. In figure 4.10 is depicted a unit circle S projected on a line, where N is the projection point and $P'$ is the projection of the point P appertains to S.

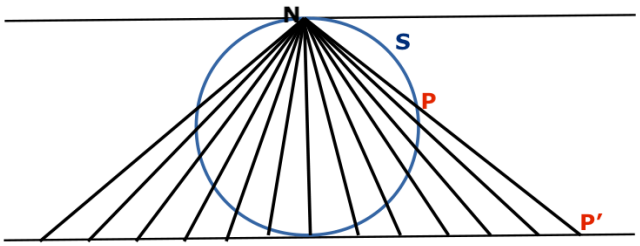


Figure 4.10: Schematization of the stereo graphic projection in 2D case

For any point P on S, there is a unique line through N and P, and this line intersects the plane exactly in one point $P'$. One of the most famous examples of stereo-graphic projection is Mercator's projection. It is the standard map projection used for navigation maps in which local directions and shapes are preserved. This projection increases the size of entities away from the equator. This enlargement is very small near the equator but increases with latitude to become infinite at the poles.

If the earth is simply thought as a sphere, each point of its surface is projected on a cylinder as sketched in figure 4.11a. As an analogy with fiber bundle, the cylinder represents the plane of projection, the base manifold, the earth is the full motion where the radial line of projection are the fibers. There are other ways of association with the fiber bundle :

- In $\mathbf{R}^4$ the $\mathbf{S}^3$ is locally fibrated in a $\mathbf{S}^2$ sphere and 1-D hyper-circles fibers attached on any point of $\mathbf{S}^2$ and they are projected on the cylinder as shown in figure 4.11b
- In $\mathbf{R}^4$ any point of the $\mathbf{S}^3$ sphere that lays on the same radius are projected on the cylinder and the radius are the fibers.

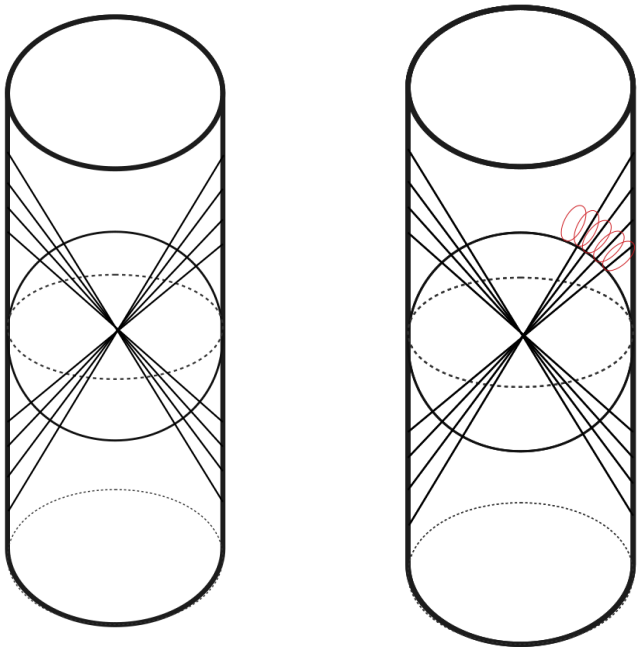

(a) General Mercator's projection (b) Mercator's projection: the fibration

Figure 4.11: Mercator's projection

- In $\mathbf{R}^4$ the $\mathbf{S}^3$ sphere is filled by 1-D hypercircles fibers.

From a mathematical point of view, the unit sphere may be a complex hyper-sphere that belongs to $\mathbb{C}^2 = \mathbb{R}^4$ and it is a set of point described by the equation:

$$x_1^2 + x_2^2 + x_3^2 + x_4^2 = 1 \tag{4.47}$$

where it has 4 independent variables $(x_1, x_2, x_3, x_4)$ and a DOF given by the radius. For this reason the sphere is said to be a geometric entity in three dimensional space $\mathbb{R}^3$ in a four dimensional space $\mathbb{R}^4$. The unit sphere is defined as sum of surface entity plus the radius as sum of $\mathbb{R}^2 \times \mathbb{R} = \mathbb{R}^3$. All the points of the volumes that lay on the same radius or any points of the surface and the corresponding fiber attached on it are projected with an only point on the cylinder. It said they are *equivalent* points or they belong to the same *equivalent class*. As the stereo-graphic projection, the projection is defined on the entire sphere, except at the poles where the radius is parallel to the cylinder. This projection method has a inner meaning of symmetry reduction. It removes the spherical symmetry projecting all the points of the sphere on the cylinder, that can be cut becoming a plane.

### 4.5.3 *HOPF reduction*

A famous non trivial projection method is the Hopf fibration represented by a $\mathbf{S}^3$ sphere fiber bundle, 1D circles $\mathbf{S}^1$ fibers and a base manifold $\mathbf{S}^2$. It is based on the stereo-graphic projection concepts. The Hopf fibration, like any fiber bundle, has the important property that is locally a product space, i.e. $\mathbf{S}^3 = \mathbf{S}^2 \times \mathbf{S}^1$

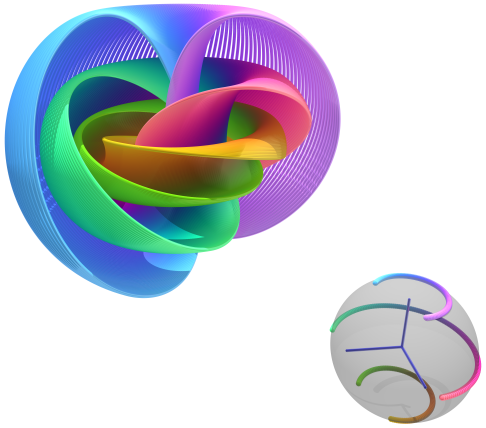

Figure 4.12: The Hopf fibration can be visualized using a stereographic projection of $S^3$ to $R^3$ and then compressing $R^3$ to the boundary of a ball. This image shows points on $S^2$ and their corresponding fibers with the same color.(wikipedia )

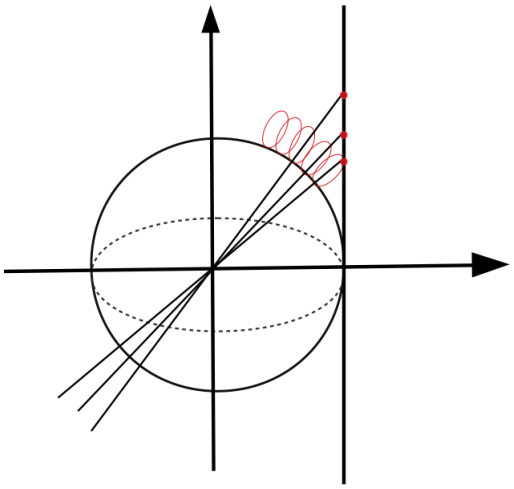

Figure 4.13: Schematization of Hopf fibration

The filling space with circle of the Hopf fibration is visible in this video. Clicking on a point on the sphere, it draws the fiber in the total space. The total space is stereographically projected onto $R^3$. Drawing an equator on the sphere it gives exactly a circle of circles — a torus.

There are numerous generalizations of the Hopf fibration. The unit sphere may be written in complex coordinate space $C^{n+1}$ naturally over the complex projective space $CP^n$ with 1D circular fibers as schematized in figure 4.13.The Hopf fibration joins into a family of four fiber bundles in which the total space, base space, and fiber space are all spheres.

### 4.5.4 *Fourier slice method*

The slice method consists in the slicing across the group orbits by a fixed hypersurface called *slice* and project the fiber bundle on it. The map function $\Pi$ is chosen to be invariant under the symmetry. The state space is sliced in such a way that an entire class of symmetry-equivalent points is represented by a single point that is the intersection with the slice Cvitanovic et al. (2005). While the slice fixes only the symmetry of the group orbits, the continuous full space trajectory remains a continuous-time trajectory in the symmetry reduce state space Willis et al. (2013). Mathematically it is a parametrization of the Fourier amplitudes of the system and each slice has its map function. Considering the trajectory in the complex full space, the components are the variables of the system:

$$z = (z_1, z_2, ..., z_n) \tag{4.48}$$

that are the complex Fourier amplitudes with phase $\phi_n$ and solutions of the dynamical system, whom expression is:

$$z_n = |z_n| e^{i\phi_n} \tag{4.49}$$

The projection is carried out through a parametrization that consists in dividing all the Fourier amplitudes by one of the $z_n$ components. Choosing the slice $Z_1 = 1$, that is the chart, with the map function in the form $Z_n = \frac{z_n}{z_1^n}$, the desymmetrized components are :

$$Z = (1, \frac{z_2}{z_1^2}, \frac{z_3}{z_1^3}, ..., \frac{z_N}{z_1^N}) \tag{4.50}$$

where $Z_1 = 1$ is the slice equation and it is a complex hyperplane where the fiber bundle is projected. This transformation caused a phase shift given by the phase of the first component. This is called First Fourier slice.

$$Z_n = \frac{z_n}{z_1^n} = \frac{|z_n|}{|z_1|^n} e^{i\phi_n - in\phi_1} \tag{4.51}$$

The corresponding desymmetrized orbit in the original state space is obtained by multiplying the map function (equation 4.50) by $|z_1|^n$ :

$$Z_D = (|z_1|, \frac{z_2\,|z_1|^2}{z_1^2}, ..., \frac{z_N\,|z_1|^N}{z_1^N}) \tag{4.52}$$

$$Z_{Dn} = z_n \frac{|z_1|^n}{z_1^n} = z_n \frac{|z_1|^n}{|z_1|^n\, e^{in\phi_1}} = z_n e^{-in\phi_1} = |z_n|\, e^{(i\phi_n - in\phi_1)} \tag{4.53}$$

The reduction is performed applying the map $\Pi$ that projects the full motion on the base manifold, doing a parametrization. If the n-solutions are shifted in phase with the multiple $n\phi_1$ of the first harmonic, it is a called First Fourier slice.

### 4.5.5 *Complex projective space* $CP^N$

The complex projection space $CP^n$ is a projective space under the action of the U(1) symmetry group; the rotational symmetry. It is represented by a quotient space of $S^{2n+1}$ hypersphere in $C^{n+1}$. For any natural number n, an n-dimensional sphere, or n-sphere, can be defined as the set of points in an $(n+1)$ dimensional space which are a fixed distance from a central point. The central point can be taken to be the origin, and the distance of the points on the sphere from this origin can be assumed to be a unit length. With this convention, the n-sphere, $\mathbf{S}^n$, consists of the points $(x_1, x_2, \ldots, x_{n+1})$ in $\mathbb{R}^{n+1}$ with $x_1^2 + x_2^2 + \ldots + x_{n+1}^2 = 1$

This is the case of Hopf fibration p : S3 → S2 of the 3-sphere over the 2-sphere

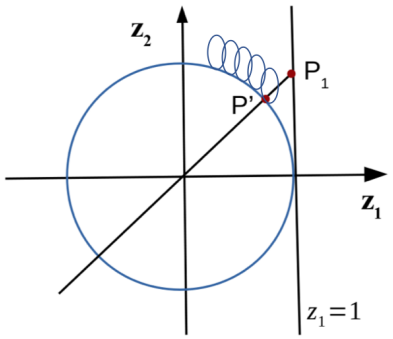


Figure 4.14: Complex projective plane $CP^2$

The unit hypersphere $\mathbf{S}$ in $\mathbf{C}^2 = \mathbb{R}^4$ is projected on a complex manifold. The sphere's points (x1, x2, x3, x4) in $\mathbf{R}^4$ satisfy the equation:

$$x_1^2 + x_2^2 + x_3^2 + x_4^2 = 1 \tag{4.54}$$

The identification of $\mathbf{R}^4$ with $\mathbf{C}^2$ and $\mathbf{R}^3$ with $\mathbf{C}$x$\mathbf{R}$, where $\mathbf{C}$ denotes the complex numbers, is possible with the complex relations:

$$(x1, x2, x3, x4) \leftrightarrow (z_1, z_2) = (x_1 + ix_2, x_3 + ix_4) \tag{4.55}$$

Thus $\mathbf{S}^3$ is identified with the subset of all ($z_1$,$z_2$) in $\mathbf{C}^2$ such that:

$$|z_1|^2 + |z_2|^2 = 1 \tag{4.56}$$

As schematized in figure 4.14, the projection hyperplane is $z_1 = 1$ and any points of the sphere $P'$ and the attached fiber $P$ belong to the same equivalent class. Any point of the sphere are projected by the radial straight lines, passing from origin, described by the complex number $\lambda = e^{i\alpha}$. It is the symmetry parameter and it varies with the $\alpha$ given by $tg\alpha = z_1/z_2$ and it is so $|\lambda|^2 = 1$ obtaining :

$$z_2 = \lambda z_1 \tag{4.57}$$

Projecting the point $P'$ on the complex plane $z_1 = 1$, the point $P_1$ has coordinates equal to:

$$P_1(z_1, z_2) = P_1(z_1, \lambda z_1) \xrightarrow{\Pi} P'(1, \frac{z_2}{z_1}) \tag{4.58}$$

where the dependence from the symmetry parameter $\lambda$ disappeared. The complex plane $z_1 = 1$ is a "cartography" of the base manifold and the projected points are non linear coordinate transformation (non physical), a distorted view of the physical space. Only after another mapping of any projected points of the $z_1 = 1$ onto the original physical space, you can obtain the desymmetrized trajectory in physical space.

Furthermore, if two points on the 3-sphere are mapped to the same point on the hyperplane, i.e., if $p(z_1, z_2) = p(w_1, w_2)$, then:

$$p(w_1, w_2) = (\lambda z_1, \lambda z_2) \in \mathbf{C} \tag{4.59}$$

The converse is also true; any two points on the 3-sphere that differs by a common complex factor $\lambda$ map to the same point on the hyperplane. These conclusions follow because the complex factor $\lambda$ cancels with its complex conjugate $\lambda^*$ in both parts of p. The projection of all the points of the sphere on the hyperplane $z_1 = 1$ allowed to removed the U(1) symmetry because they are independent from $\lambda$.

More in general, $CP^n$ is the quotient space of a $S^{2n+1}$ sphere in $C^{n+1}$ under the action of the $U(1)$ group ,

$$CP^n = S^{2n+1}/U(1) \tag{4.60}$$

Indeed, every line in $C^{n+1}$ intersects the unit sphere $S^{2n+1}$ in a circle $S^1$ and we obtain a point of $CP^n$ defined by this line by identifying all points on $S^1$. The projection $\Pi : S^{2n+1} \longrightarrow CP^n$ is called hopf mao. Since $CP^1 = S^2$ we obtain the classical Hopf bundle $S^3 \rightarrow S^2$ with fiber $S^1$. When $n = 1$, the complex projective space $CP^1$ is the Riemann sphere, and when $n = 2$, $CP^2$ is the complex projective plane.

### 4.5.6 *Translation complex projection* $TCP^n$

The $CP^n$ space can be generalized to the Toric space $TCP^n$ that is a projective space under the action of the T-symmetry group; the translational symmetry. It is a quotient space of $E^{2n+1}$ hypersurfaces i.e. in $C^{n+1}$ given by:

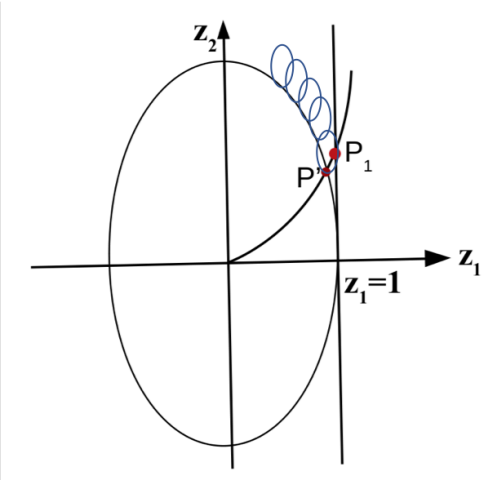


Figure 4.15: $TCP^N$ scheme

$$E^{2n+1} = \left\{ z = z_1 ... z_{n+1} \in C^{n+1} : \sum_{j=1}^{n+1} |z_j|^{\frac{2(n+1)}{j}} = 1 \right\} \tag{4.61}$$

under the action of the translational group $T(1)$. The circular fibers are attached to any points of the ellipsoid where any points are expressed by:

$$z = \{z_1, z_2, ..., z_N\} \in \mathbb{C}^n \tag{4.62}$$

An element z of $TCP^n$ is defined with $w$, the set of equivalent class and with the symmetry parameter $\lambda = e^{i\alpha} \in \mathbb{C}$ and $|\lambda| = 1$ that is:

$$w \sim (\lambda z_1, \lambda^2 z_2, ..., \lambda^n z_n) \in \mathbb{C}^n \forall \lambda \tag{4.63}$$

that is a parametrization of the system given by the maps $\Pi$ that is:

$$z \sim w \Leftrightarrow \exists \lambda \in \mathbb{C} \colon \left\{ w_j = \lambda^j z_j \right\}_{j=1,2...,N} \tag{4.64}$$

The reduction is given by the stereographic projection of any point of the hyper-ellipsoid on a complex plane $z_1 = 1$ trough parabolas. All the points of the parabola are also projected with a single point on the complex plane that is $\mathbb{C}^n = \mathbb{CP}^{n-1} \times \mathbb{C}$

In $n = 1$ case that is $\mathbf{C}^2 = \mathbf{C}x\mathbf{R}$, the parametrization returns:

$$|\lambda z_1|^4 + |\lambda^2 z_2|^2 = |\lambda|^4 (|z_1|^4 + |z_2|^2) \tag{4.65}$$

and

$$|\lambda|^4 Q = |w_1|^4 + |w_2|^2 \tag{4.66}$$

where $|\lambda| = 1$

## 4.6 T-SYMMETRY REDUCTION

Consider a non linear dynamical system with a real space-periodic state $u(x,t)$ and governed by the partial differential equation:

$$\partial_t u = N(u, \partial_x u, \partial_{xx} u) \tag{4.67}$$

The Navier-Stokes equations belongs to this class of partial differential equations. The dynamics satisfied the continuous translation symmetry $G_{x_0}$ that is if $u(x,t)$ is a solution of equation 4.67 so is $G_{x_0} = u(x + x_0)$.

As shown before it is convenient to work in Fourier space, thus the solution $u(x,t)$ is:

$$u(x,t) = \sum_{n=1}^{N} z_n e^{ik_0 nx} = \sum_{n=1}^{N} |z_n| e^{ik_0 nx + \phi_n} \tag{4.68}$$

where $z_n = |z_n| e^{i\phi_n}$ are the complex Fourier amplitudes with phase $\phi_n$ and $k_0 = 2\pi/L$ the minimum wave number with L the domain size. The dynamic of $z_n$ is governed by

$$\dot{z}_n = F_n(z_1, z_2, ..., z_n) \tag{4.69}$$

where $F_n$ is the discrete Fourier transform of $N(z)$ in 4.67.

The dynamical system admits the continuous T-symmetry if a phase shift $\alpha$ (a space translation in physical space) is applied to the system described by the equation :

$$\dot{z}_n e^{in\alpha(t)} = F_n(z_1 e^{i\alpha}, z_2 e^{2i\alpha} ... z_N e^{Ni\alpha}) \tag{4.70}$$

Multiplying both sides by $e^{-in\alpha}$

$$\sum_{n=1}^{N} e^{-in\alpha} e^{in\alpha} \dot{z_n} = \sum_{n=1}^{N} e^{-in\alpha} F_n(z_1 e^{i\alpha}, z_2 e^{2i\alpha} ... z_N e^{Ni\alpha}) \tag{4.71}$$

Since the system admits $T(1)$ symmetry, the $F_n$ satisfy the property:

$$e^{-in\alpha} F_n(z_1 e^{i\alpha}, z_2 e^{2i\alpha} ... z_N e^{Ni\alpha}) = F_n(z_1, z_2 ... z_N) \tag{4.72}$$

and

$$\dot{z}_n = \overbrace{e^{-in\alpha} F_n(z_1 e^{i\alpha}, z_2 e^{2i\alpha} ... z_N e^{Ni\alpha})}^{F_n(z)} \tag{4.73}$$

$$\dot{z}_n = F_n(z) \tag{4.74}$$

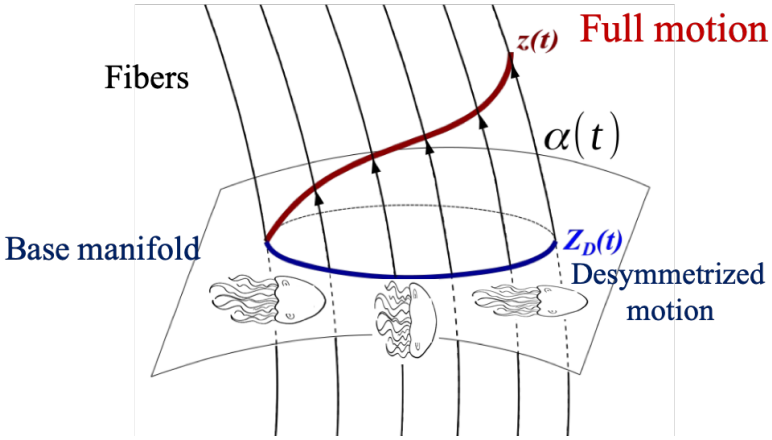


Figure 4.16: Fiber bundle composed by the full motion $z(t)$ (red line), fibers(narrow black lines), desymmetrized motion $Z_D(t)$ (blue line) and the base manifold (curved plane)

Thus, the initial equation is obtained again because the dynamical system admits a T-symmetry.

As explained in the previous sections, the continuous translation symmetry reduction is performed projecting the group orbits $G_\alpha(z)$, composed by the full motion and the fibers, on the base manifold. It removes the dependence on the symmetry returns a base motion using a map $\Pi$ that has to be invariant under the symmetry. The trajectory $z(t) = (z_1, z_2, ...z_N)$ moves in the state space $P \in \mathbf{C}^N$ which geometrically can be represented by a fiber bundle denoted with the quadruplet: the total space $\mathbf{P} \in \mathbf{R}^N$, the base manifold M, the group orbits $G^\alpha(z)$ expressed by:

$$G^\alpha(z) = (z_1 e^{i\alpha}, z_2 e^{i2\alpha} ... z_N e^{iN\alpha}) \tag{4.75}$$

the fibers, function of $\alpha \in \mathbf{R}$, and the map function $\Pi$. In figure 4.16 is shown how the full motion $z(t)$ is decomposed in a component on the base manifold, called desymmetrized motion $Z_D(t)$, and in a part along the fibers, the transversal motion, connected with the phase-shift $\alpha$ along the fibers.

The desymmetrized trajectory on the base manifold is given by the map function $\Pi$ that is:

$$Z = \Pi(z) = (Z_1, Z_2, ..., Z_N) \tag{4.76}$$

where each component is given by the projection method used. As explained before, the map function $\Pi$, already proved to be invariant under the symmetry $\alpha$, can be given by slice method by the relation:

$$Z_n = z_n \left(\frac{\overline{z_1}}{z_1}\right)^n = \frac{z_n |z_1(t)|^n}{z_1^n} = |z_n(t)| e^{i(\phi_n - n\phi_1)} \tag{4.77}$$

so all the desymmetrized components are:

$$Z = \Pi(z) = (|z_1|, |z_2|e^{i(\phi_2 - 2\phi_1),\ldots,|z_N(t)|e^{i\Phi_N - n\phi_1}}) \tag{4.78}$$

where $\phi_1$ is the phase of the first harmonic.

In a turbulent condition, the continuous translation symmetry is connected to a mean velocity of convection that brings the eddies from upstream to down stream. The desymmetrized motion is connected with a motion caused by eddies deformation and their interaction. As shown in figure 4.16 the desymmetrized motion $Z_D(t)$ may be imagined as jellyfish motion produced only from its shape-changing.

The core of the problem consists in the fact that at first only the full motion $z(t)$ is known and only performing the projection is possible to uncouple the full motion into the desymmetrized motion and the fibers. In order to understand the group orbit $G^\alpha$ it is useful to image of attaching onto any point of $z(t)$ a fiber. The desymmetryzed motion Z is the projection of the full motion on the base manifold. As demonstrated before, the full motion can be seen as a phase-shifting of the desymmetrized motion on the fibers. The shift is composed by the dynamical phase and the geometric phase. The shift along the fibers that brings the motion in the comoving frame is called dynamical phase. "Only dead fish go with the flow: comoving frame" Cvitanovic et al. (2005). For example it is the translational shift induced by the mean convective velocity in the channel flow and its projection on the base manifold is represented by a point. The shift along the fiber necessary to project the full trajectory on the base manifold includes a geometric phase and it allows to reduce a relative periodic orbit in a periodic orbit. The reducing of the symmetry allows to uncouple these two components of the motion: one connected with the dynamical phase and the other one to the geometric phase. In fact the dynamical phase increases with the time spent by the trajectory to wander around the state space of the dynamical system P and system's answer to: "how log did your trip take?". Instead, the geometric phase is independent of time and it depends only upon the geometry of P and system's answer to "where have you been?".

Sometimes, in order to desymmetrized the system should may be useful to perform more than a "projection" (as shown in figure 4.18) because some functions map hide the physical meaning of the variable. The slice method gives desymmetrized variables that are physical: for example setting the phase of the first harmonic of the full z to zero in the first-Fourier slice. In other projection method as the Hopf reduction for U(1) and the extension to T(1) the desymmetrized variables are nonlinear transformation of the original variables. However, another transformation of variables can be used that maps to physical variables as is shown in figure 4.18, where the first mapping is preformed with $\Pi_{chart}$ that projects the full motion on complex plane where the trajectory $Z_{chart}(t)$ (green line) lose their physical meaning. For this reason a second

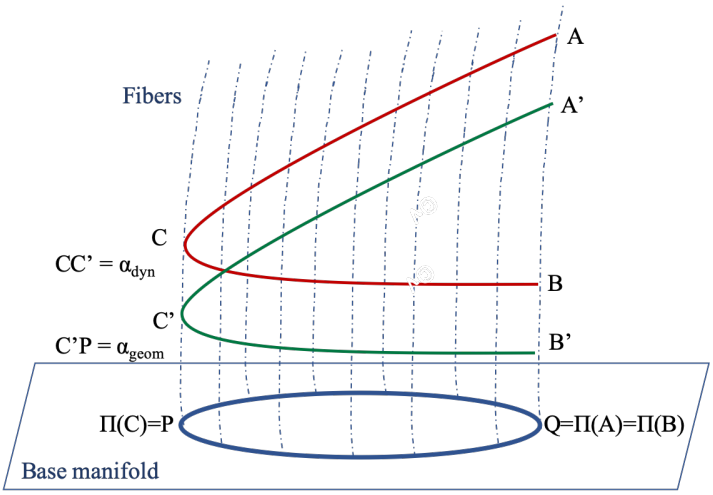


Figure 4.17: Principal fiber bundle. The relative periodic orbit ABC is reduced to a periodic orbit PQ in the base manifold by the phase shifting of the trajectory along the fibers. The shift is composed by the dynamical end geometric phases. The shift induced by the dynamical phase leads to the comoving trajectory A′B′C′ to be transversal to the fibers but its not closed. A further shift by the geometric phase leads the trajectory A′B′C′ to the closed PQ trajectory on the base manifold.

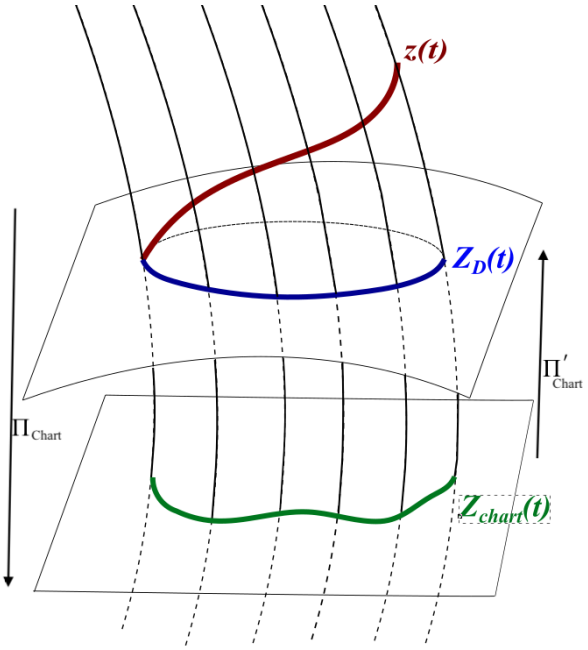


Figure 4.18: Example of more than a projection application

projection $\Pi'_{chart}$ maps the $Z_{chart}(t)$ to another complex plane providing the desymmetrized trajectory $Z_D(t)$ (blue line)

### 4.6.1 *Geometric and dynamical phases and velocities decomposition*

Once the projection was performed, the symmetry is demonstrated to be dependent from the fibers and the uncoupling of the phase shifting is allowed.

Taking into account the group orbit $z^{\alpha}(t,\alpha) = \left\{z_n(t)e^{in\alpha(t)}\right\}$ (see also

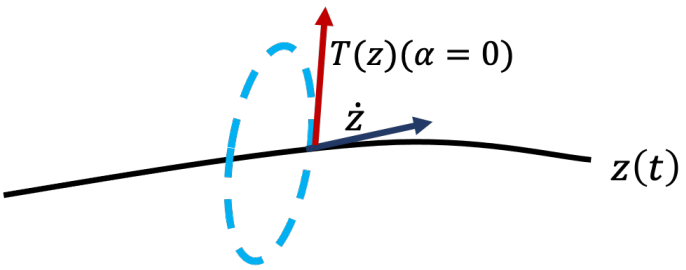


Figure 4.19: Schematization of a part of the group orbit $z_\alpha$ composed by the full motion $z(t)$ and the circular fiber attached on it. The tangents on the full trajectory $z(t)$ is $\dot{z}$ and to the fiber is $T(z)$ attached in that same point.

equation 4.39) composed by the full motion $z(t)$ and by the circular fiber attached to the trajectory as shown in figure 4.19. Choosing a point on the trajectory, $\dot{z}$ and $T(z,\alpha=0)$ are respectively tangents on the trajectory and on the fiber in that point where the tangent to the fiber is given by equation 4.42 that we rewrite for clarity:

$$T_n(z_1e^{i\alpha},\dots z_Ne^{iN\alpha}) = \frac{\partial\left\{z_ne^{in\alpha}\right\}}{\partial\alpha} = \left\{inz_ne^{in\alpha}\right\} = \{inz_n^{\alpha}\} \tag{4.79}$$

being $z^{\alpha}(t,\alpha) = \left\{z_n(t)e^{in\alpha(t)}\right\}$ the group orbit.

In the same way in the base manifold, tangents on desymmetrized motion $\dot{Z}$ and on the fiber $T(Z)$ are traced along the same fiber as shown in figure 4.20a. The tangent of the full motion $\dot{z}$ can be considered to be decomposed in two components: one orthogonal and one parallel to the fiber. As depicted in figure 4.20b, the two couple of components respectively $\dot{z}$ and $\dot{Z}$ and $T(z)$ and $T(Z)$ have the same modulus but different direction, caused by the curvature of the fiber. The derivative to the group orbit $z^{\alpha}(\alpha,t)$ is

$$\frac{dz^{\alpha}(t,\alpha)}{dt} = \frac{dz(t)}{dt}e^{in\alpha(t)} + inz(t)e^{in\alpha(t)}\dot{\alpha} = \dot{Z}(t) + T(z)\dot{\alpha} \tag{4.80}$$

As a results the tangent $\dot{z}$ to the trajectory is given by:

$$\dot{z} = \dot{Z} + T(z)\dot{\alpha} \tag{4.81}$$

where $\dot{Z}$ is the tangent on the base motion trajectory, while $T(z)\dot{\alpha}$ is the term connected to the symmetry. Once the full trajectory is projected on the base

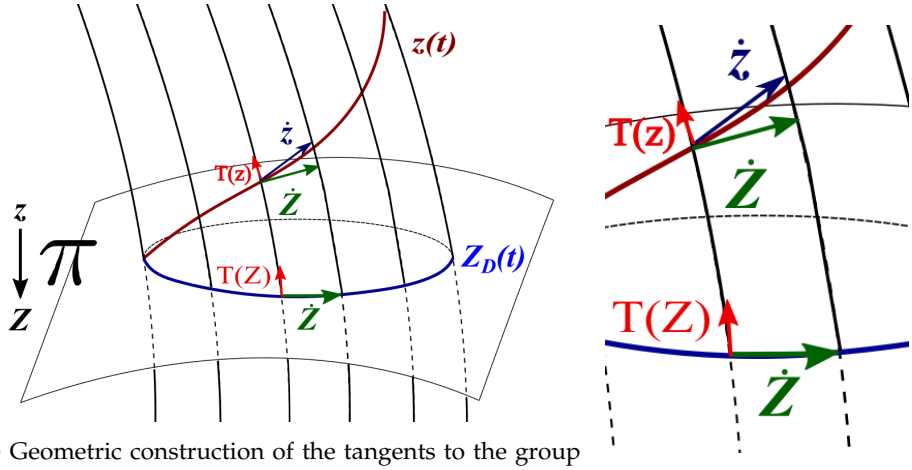


(a) Geometric construction of the tangents to the group orbits.

(b) Zoom

Figure 4.20: component decomposition of the tangents to the group orbits

manifold, the desymmetrized variables and the shift $\alpha$ are known. The next step is the determination of the phase velocity $\dot{\alpha}$ and its uncoupling as:

$$\dot{\alpha} = \dot{\alpha}_{dynamical} + \dot{\alpha}_{geometric} \tag{4.82}$$

where $\alpha_{dynamical}$ is the *dynamical velocity* and $\dot{\alpha}_{geometric}$ is the *geometric velocity*. Taking into account equation 4.81 and the equations of the dynamical system in Fourier space 4.40 and 4.41 and the base motion equation (4.44) written easily as

$$z(t) = Z(t)e^{-in\alpha} \tag{4.83}$$

it yields:

$$\dot{Z}_n e^{-in\alpha} - in\dot{\alpha}Z_n e^{-in\alpha} = F_n\left(z_1, z_2, ..., z_N\right). \tag{4.84}$$

Next step involves the projection of $\dot{z}$ along the fiber, multiplying equation 4.40 by $T(z)$ and exploiting the property of the scalar product (see also Appendix D ):

$$\dot{z} \cdot T(z) = F(z) \cdot T(z) \tag{4.85}$$

It means to multiply the equation 4.84 by $T(z)$, that is:

$$\sum_n \overline{T}_n(z)\left(\dot{Z}_n e^{-in\alpha} - in\dot{\alpha}Z_n e^{-in\alpha} - F_n(z_1, z_2, ..., z_N)\right) = 0 \tag{4.86}$$

Taking into account the tangent definition $T_n(z) = inz_n^{\alpha}$ and $Z_n = z_n e^{in\alpha}$ and applying the scalar product: (see also APPENDIX D), one obtains:

$$\Re \sum_1^N \overline{T}_n(z)\left(\dot{Z}_n e^{-in\alpha} - T_n(z)\dot{\alpha} - F_n(z)\right) = 0 \tag{4.87}$$

where $\mathbb{R}()$ is the real part of $z$.

The properties of complex numbers applied on the module of the two tangents :

$$|T(z)|^2 = \overline{T}(z)T(z) = \sum(-in\bar{z}_n)(inz_n) = \sum n^2 z_n \overline{z_n} = \sum n^2|z_n|^2 \quad (4.88)$$

and:

$$|T(Z)|^2 = \overline{T}(Z)T(Z) = \sum(-in\overline{Z}_n)(inZ_n) = \sum n^2 Z_n \overline{Z_n} = \sum n^2|Z_n|^2 \quad (4.89)$$

and beeing $|z_n|^2 = |Z_n|^2$ by definition, it allows to demonstrate that tangents have the same modulus but different direction, that is:

$$|T(z)|^2 = |T(Z)|^2 \quad (4.90)$$

Coming back to the equation 4.87 and by making multiplication explicit:

$$\Re\sum[\overline{T(z)}_n \dot{Z}_n e^{-in\alpha}] - \dot{\alpha}\Re\sum[\overline{T(z)}_n T_n(z)] - \Re\sum[\overline{T}(z)_n F_n(z)] = 0 \quad (4.91)$$

The first element is:

$$\sum \overline{T(z)}_n \dot{Z}_n e^{-in\alpha} = \sum -in\bar{z}_n \dot{Z}_n e^{-in\alpha} = \sum -in\overline{Z}_n \dot{Z}_n \Rightarrow \overline{T(Z)} \cdot \dot{Z} \quad (4.92)$$

given also by the equality

$$T(Z) \cdot \dot{Z} = \sum \Re(T_n(Z)\dot{\overline{Z}}_n) = \sum \Re(\overline{T_n(Z)}\dot{Z}_n) \quad (4.93)$$

applicable to the other terms obtaining the equation:

$$T(Z) \cdot \dot{Z} - \dot{\alpha}T(z) \cdot T(z) - T(z) \cdot F(z) = 0 \quad (4.94)$$

Finally the relation, mentioned before, is obtained where the phase velocity $\dot{\alpha}$ is uncoupled in two components, dynamic and geometric:

$$\dot{\alpha} = \frac{T(Z) \cdot \dot{Z}}{|T(Z)|^2} - \frac{T(z) \cdot F(z)}{|T(z)|^2} = \dot{\alpha}_{geom} + \dot{\alpha}_{dynamic} \quad (4.95)$$

If $T(Z) \cdot \dot{Z} = 0$ then the fibers are aligned with the base manifold and the geometric component disappears. For this reason the base manifold must be orthogonal to the fibers. It may be more convenient to express them as a function of the Fourier amplitudes, considering equations 4.79,4.89 ,4.93 and $|z(t)| = |Z(t)|$ and see Appendix E, so the geometric phase velocity is :

$$\dot{\alpha}_{geom} = \frac{\sum \Re[-in\overline{Z}_n \dot{Z}_n]}{\sum n^2|Z_n|^2} \quad (4.96)$$

and the dynamic phase velocity is:

$$\dot{\alpha}_{dynamic} = -\frac{\sum \Re[-in\overline{z_n}F_n(z)]}{\sum n^2|z_n|^2} \tag{4.97}$$

The first observation is that the dynamical phase velocity is written as a function of the original variables $F_n(z)$ and $z_n$ so it can be evaluated regardless of desymmetrization, while the geometric phase velocity one can be evaluated after the desymmetrizzation.

Considering the desymmetrized variables $Z_n$ (see equation 4.53 ) and substituting it in the two components (see Appendix E for details), the dynamic and geometric phase velocity are given by:

$$\dot{\alpha}_{geom} = \frac{\sum n\,|z_n|^2\,(\dot{\phi}_n - n\dot{\phi}_1)}{\sum n^2\,|z_n|^2}. \tag{4.98}$$

$$\dot{\alpha}_{dynamic} = -\frac{\sum n^2\,|z_n|^2\,\frac{\dot{\phi}_n}{n}}{\sum n^2\,|z_n|^2} \tag{4.99}$$

The term $(n\dot{\phi})$ of the dynamic phase velocity (equation 4.99) is a weighted average of the phase velocity of all the harmonics and higher frequencies have more weight on its value. Adding the two components (see Appendix E for details) we obtain that the $\dot{\alpha} = \dot{\alpha}_{tot} = \dot{\phi}_1$, that is the total phase shifting along the fibers to project the full motion on the base manifold

Taking into account only the dynamical phase, the comoving trajectory can be found shifting the trajectory $z(t)$ along the fiber by $\alpha_{dyn}$ that is:

$$Z_c(t) = z_n(t)e^{-ik_0 n\alpha_{dyn}} \tag{4.100}$$

The comoving trajectory $Z_c(t)$ moves through the fiber bundle locally transversal to the fibers as:

$$\frac{\Im \sum n\overline{Z}_n\dot{Z}_n}{\sum n^2\overline{Z}_nZ_n} = 0 \tag{4.101}$$

because in this condition of traversality to the fiber or group orbit the vectors $\overline{Z}_n$ and $\dot{Z}_n$ are orthogonal. This motion is referred to as horizontal transport through the fiber bundle. The trajectory $Z_c$ may experience a shift by the geometric phase $\alpha_{geom}$ and the desymmetrized trajectory $Z$ in the base manifold is obtained.

*In physical space*

Now the goal is finding the meaning of the dynamical and geometric phase velocity in the physical space. Considering the linear advection equation:

$$\frac{\partial u}{\partial t} + c\frac{\partial u}{\partial x} = 0 \tag{4.102}$$

where c is the convection velocity. The space and time derivative expressed in the Fourier domain:

$$\frac{\partial u}{\partial x} = \sum i n z_n e^{i n k_0 x} \tag{4.103}$$

$$\frac{\partial u}{\partial t} = \sum \dot{z}_n e^{i n k_0 x} \tag{4.104}$$

and the relation between Fourier components of the full and desymmetrized trajectory is given by:

$$z_n(t) = Z_n(t) e^{i n \alpha(t)}. \tag{4.105}$$

It follows that the sum of geometric phase velocity $\dot{\alpha}_{dynamic}$ (equation **??**) and geometric phase velocity $\dot{\alpha}_{geometric}$ ( equation **??** ) is the total velocity $\dot{\alpha}$ that can be written as:

$$\dot{\alpha} = \frac{\overbrace{< \frac{\partial U^D}{\partial t} \cdot \frac{\partial U^D}{\partial x} >}^{-\dot{\alpha}_{geom}}}{< \frac{\partial U^D}{\partial x} \cdot \frac{\partial U^D}{\partial x} >} - \frac{\overbrace{< \frac{\partial u}{\partial t} \cdot \frac{\partial u}{\partial x} >}^{\dot{\alpha}_{dynam}}}{< \frac{\partial u}{\partial x} \cdot \frac{\partial u}{\partial x} >}, \tag{4.106}$$

in terms of the full solution $u$ and the desymmetryzed solution $U^D$ expressed in the physical space, and where $< f(x) >= \frac{1}{b-a} \int_a^b f(x) dx$.

As demonstrated above, the dynamic velocity is a function of the full motion both in state variables $\{z_n\}$ and physical variables $u$ (4.106). On the contrary, the geometric component

$$\dot{\alpha}_{geom} = -\frac{< \frac{\partial U^D}{\partial t} \cdot \frac{\partial U^D}{\partial x} >}{< \frac{\partial U^D}{\partial x} \cdot \frac{\partial U^D}{\partial x} >} \tag{4.107}$$

can be evaluated only after the symmetry reduction because it is a function of the desymmetrized variables. Thus, symmetry reduction is necessary since it allows to discover the system's dynamics connected with the changing shape of vortices.

Moreover, the dynamical phase velocity is related to the convection velocity. In fact if $f(x)$ is a solution of the dynamical system $\frac{\partial u}{\partial t} = -c \frac{\partial u}{\partial x}$ then the dynamical velocity follows as:

$$U_d = -\frac{< \frac{\partial u}{\partial t} \cdot \frac{\partial u}{\partial x} >}{< \frac{\partial u}{\partial x} \cdot \frac{\partial u}{\partial x} >} = +\frac{< c \frac{\partial u}{\partial x} \cdot \frac{\partial u}{\partial x} >}{< \frac{\partial u}{\partial x} \cdot \frac{\partial u}{\partial x} >} = c \tag{4.108}$$

In the case of turbulent flow, in condition of weak turbulence the contribution of the rotation and the shape changing of vortices is negligible respect to the convective velocity: they can be considered as frozen and carried by the current with a velocity *c*. This is the Taylor hypothesis, the velocity c is called *Taylor velocity* and it coincides with the convection velocity (Taylor, 1938).

For the general dynamical system:

$$\frac{\partial u}{\partial t} = N(u) \tag{4.109}$$

the advection by a velocity c can occur only approximately, that is

$$\frac{\partial u}{\partial t} + c\frac{\partial u}{\partial x} \simeq 0. \tag{4.110}$$

In order to find c, the ordinary least square is used to find the value of c that minimize

$$E = \int \left(\frac{\partial u}{\partial t} + c\frac{\partial u}{\partial x}\right)^2 dx \tag{4.111}$$

Find c that minimizes E,

$$\frac{\partial}{\partial c}\int \left(\frac{\partial u}{\partial t} + c\frac{\partial u}{\partial x}\right)^2 dx = \int 2\left(\frac{\partial u}{\partial t} + c\frac{\partial u}{\partial x}\right)\frac{\partial u}{\partial x} dx = 0, \tag{4.112}$$

or obtain:

$$\int \frac{\partial u}{\partial t}\frac{\partial u}{\partial x} dx + c\int \frac{\partial u}{\partial x}\frac{\partial u}{\partial x} dx = 0 \tag{4.113}$$

The expression for the velocity c, follows as:

$$c = -\frac{\int \frac{\partial u}{\partial t}\frac{\partial u}{\partial x} dx}{\int \frac{\partial u}{\partial x}\frac{\partial u}{\partial x} dx} \tag{4.114}$$

that is the same expression of the dynamical phase velocity.

Otherwise, in condition of strong turbulence the equality is not more verified:

$$\frac{\partial u}{\partial t} + c\frac{\partial u}{\partial x} \simeq 0 \tag{4.115}$$

In condition of strong turbulence the Taylor's hypothesis is not enough to describe the total motion. This is due to the dynamical velocity plus a component, the geometric phase velocity, given by the deformation of vortices.

## 4.7 CONCLUSION

The symmetry reduction theory was explained in details in order to be able to applied it to the turbulent channel flow and find the hidden motion of vortices produced by their shape-chaining and their interaction.

# 5

# SYMMETRY REDUCTION OF TURBULENT CHANNEL FLOWS

## 5.1 INTRODUCTION

Turbulent flow is generally characterized by a chaotic motion of the fluid particles that are advected in an irregular flow varying in time and space. However, if we look at the turbulent structures, i.e. the vortices in the field (see figure 5.1 and video), they seems mainly advected by the mean flow.

More in detail, the vortical structure borns at the wall where large velocity gradient occurs, then it is advected toward the center of the channel where it continues its travel advected by the mean flow, merging with or splitting by interacting with other vortices and finally dissipating on the small scales. This is also the mechanism at the base of the direct energy cascade. This classical vision of the turbulence obscures some features of the turbulent structures, that can be revealed by looking with a closer view and by following in a Lagrangian way the single vortex. This is highlighted in figure 5.2, which shows an enlarged view of an isolated vortex (identified through a suitable spatial windows moving in time), among the others in the turbulent channel. It is well evident as the flow structure, while being advected along the channel, it changes continuously its shape by focusing and defocusing its energy content through a modulation of its amplitude. This simple observation suggests a new vision of the turbulence structure which needs novel theoretical tools able to reveal the shape of the turbulence, that is the main objective of this thesis work. The tool here proposed is the symmetry reduction method, originally proposed by (Siminos and Cvitanović, 2011) and developed by (Fedele et al., 2015).
This implied to study it as a chaotic non-linear system in state space of a high-dimensional system.

In physical space (see figure 5.2 and video), translational symmetry of turbulent channel flow, connected with the fluid convection in x-direction, makes it difficult to identify the breathing turbulent structures: vortices travel with their own velocity, deforming as they are advected downstream. Working in the state space allows to remove or quotient out the symmetry (see chapter §4) and unveil only the motion given by vortex shape changing. From a dynamical

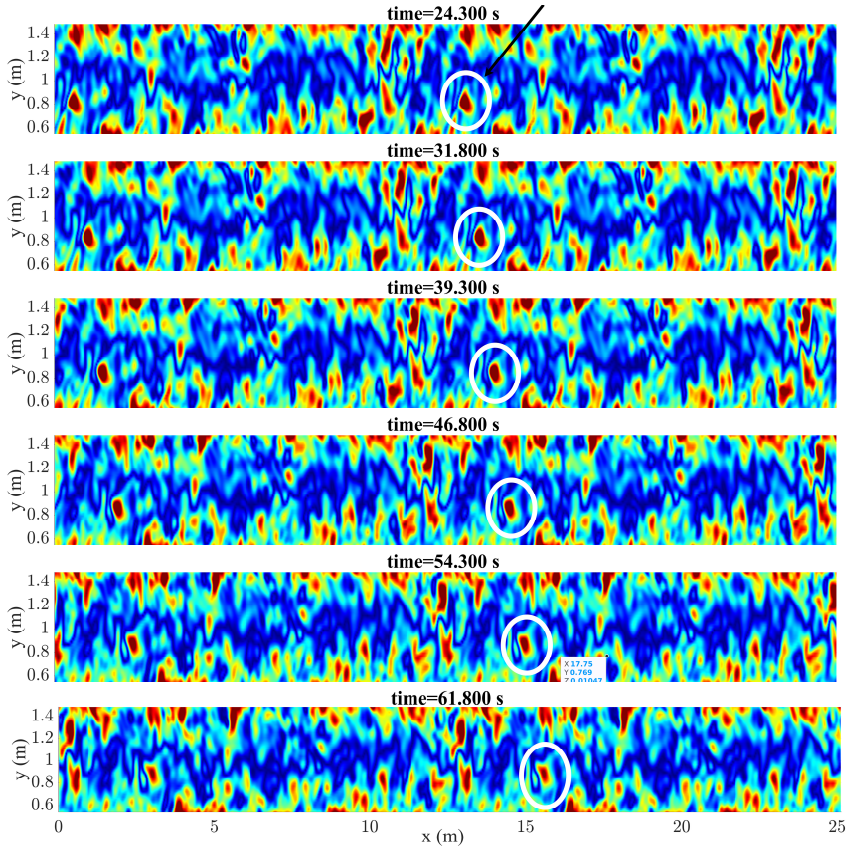


Figure 5.1: Time frames of global spanwise vorticity field $\omega_z(x, y, t)$

system perspective, if symmetry is present, the total velocity $V$ of the vortical motion can be uncoupled in a dynamical and a geometric component (Fedele et al., 2015)

$$V = V_{dyn} + V_{geom} \tag{5.1}$$

The dynamical velocity $V_{dyn}$ is connected to the inertia of the turbulent flow, to its vortex interactions, and to the external forcing such as pressure gradients. The geometric velocity $V_{geom}$ is induced by the intensity of the shape-changing dynamics of vortices. Once symmetry is removed, the dynamic and geometric phase velocities can be uncoupled. The desymmetrized state space reveals how: i) vortices change shape in time and ii) their shape-changing influences their own motion. Conceptually this is what was performed on leapfrogging vortices (Chapter §3), where the continuous translational symmetry was removed in order to distinguish dynamically the motion given by the shape changing and by the vortices interaction. Here the difference is related to the viscosity and to the non-linearity of this dynamical problem that needs the application of a more general approach. The approach followed in this chapter is to look from the

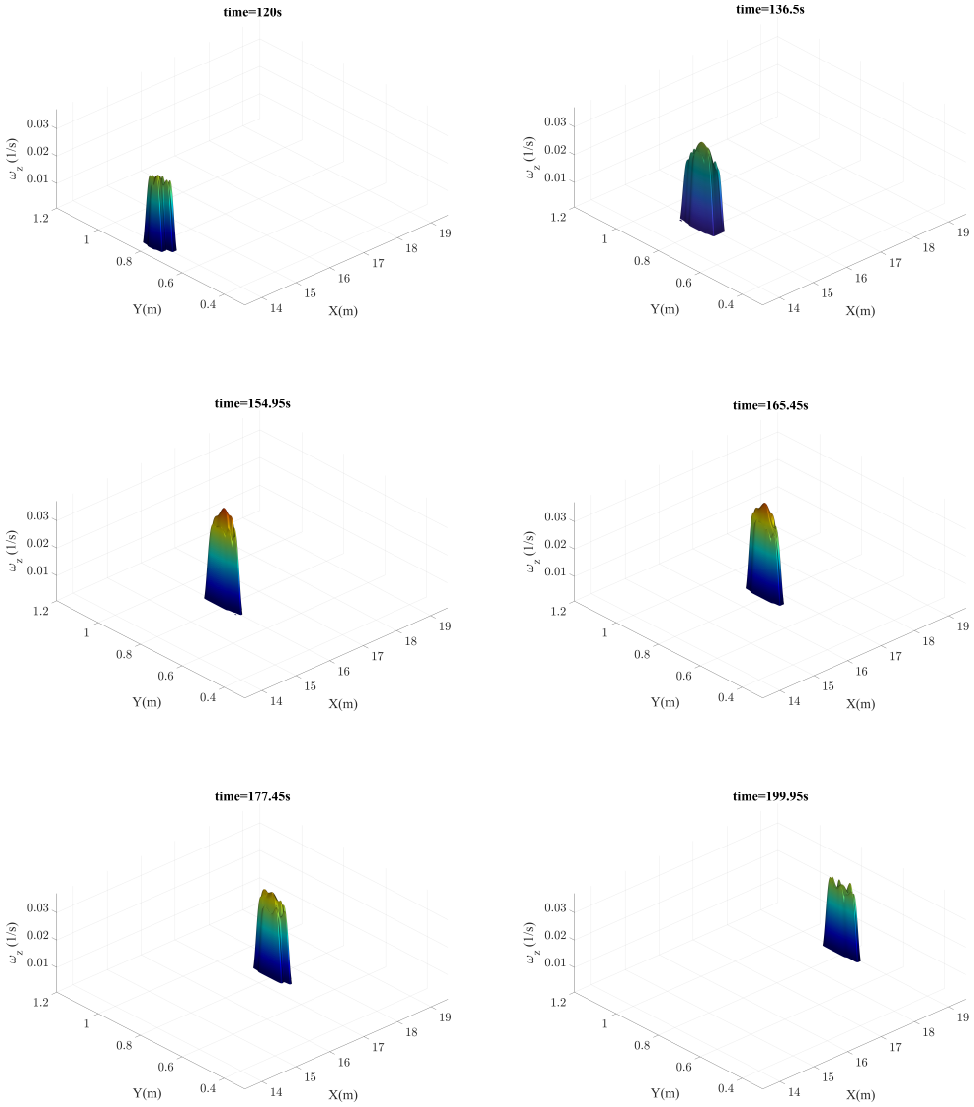


Figure 5.2: Time frames of a vortex dynamics

global to local view. This means that the turbulence is a phenomenon involving all the energy scales through the energy cascade. The evolution at the global scale, necessary for an overall comprehension of the turbulent flow in line with the classical statistical approach, indeed, can hide or simply average some local details of the simmetry reduction occurring on the single vortex dynamics. This motivates the investigation approach used in this chapter: the first part focuses on the results of the symmetry reduction applied to global fields of the streamwise velocity and of the spanwise vorticity of the turbulent channel flow; the second part analyzed the results of tracking a group of vortices during their

motion in the channel. Because of the limit of the computational resources and to bound the computational burden, all the considered fields are averaged along z-direction and are defined on a time window as large as to 202 s, which corresponds to 1347 time steps.

## 5.2 SYMMETRY REDUCTION OF THE CHANNEL FLOW: A GLOBAL VIEW

The symmetry reduction is applied to global fields of streamwise velocity and spanwise vorticity of the turbulent channel flow. The procedure and the results are described in detail.

### 5.2.1 *Overcoming the Taylor Hypothesis: the comoving frame.*

Consider the incompressible three dimensional flow field $U(x, y, z, t) = (U_0, V_0, W_0)$ that satisfies the NS equation with the proper boundary conditions.
The continuous translational symmetry is such that given a solution

$$U(x, y, z, t),$$

the

$$U(x - \ell, y, z, t)$$

is still a solution of the NS equations for any arbitrary value of $\ell$. The presence of the continuous translational symmetry permits the definition of the shift $\ell$ and to introduce new reference systems from which the flow can be observed. The comoving frame is $(x - \ell_{dyn}(t), y, z, t)$ with $\ell_{dyn}$ the dynamical shift. The time derivative of the dynamical shift it is the dynamical velocity:

$$U_d = \frac{d\ell_{dyn}}{dt} \tag{5.2}$$

already derived in Chapter 4, that is

$$U_d = -\frac{< \partial_t U \partial_x U >_x}{< \partial_x U \partial_x U >_x} \tag{5.3}$$

The desymmetrized frame is $(x - \ell_{dyn}(t) - \ell_{geom}, y, z, t)$ with $\ell_{geom}$ the geometric shift. The time derivative of the geometric shift is the geometric velocity

$$U_g = \frac{d\ell_{geom}}{dt} \tag{5.4}$$

later defined. The brackets $< \cdot >$ denote the space average in x-direction.
Consider the spanwise vorticity $\omega(x, y, z, t) = \omega_0$ as a passive scalar field advected and dispersed by $U_0$ in accord to:

$$\frac{\partial \omega_0}{\partial t} + U_0 \nabla \omega_0 = D_m \nabla^2 \omega_0 + f_0 \tag{5.5}$$

where $D_m$ is the diffusion coefficient and f the sources and sinks. In the pair $(U_0, \omega_0)$, the $U_0$ evolves according to the NS equations with no-slip condition at the wall boundary and $\omega_0$ evolves according to eq 5.5. Streamwise translation symmetry implies that if $(U_0, \omega_0)(x, y, z, t)$ is a solution, so is $(U_0, \omega_0)(x - \ell, y, z, t)$ for an arbitrary and fixed shift $\ell$. The dynamical velocity 5.3 can be used to minimize, on average, the material derivative:

$$\frac{D\omega_0}{Dt} = \frac{\partial \omega_0}{dt} + U_d^{3D} \frac{\partial \omega_0}{\partial x} \tag{5.6}$$

that is:

$$\left\langle (\frac{\partial \omega_0}{dt} + U_d^{3D} \frac{\partial \omega_0}{\partial x})^2 \right\rangle_{x,y,z} \tag{5.7}$$

and it is the smallest possible if

$$U_d^{3D}(t) = -\frac{\langle \partial_t \omega_0 \partial_x \omega_0 \rangle_{x,y,z}}{\langle (\partial_x \omega_0)^2 \rangle_{x,y,z}} \tag{5.8}$$

where $\langle \cdot \rangle$ denote space average in x,y and z. When $\frac{D\omega_0}{Dt} = 0$ the diffusion term, source and sink are in balance and 5.10 can be written as:

$$U_d^{3D}(t) = -\frac{\left\langle U_0(\partial_x \omega_0)^2 + \partial_x \omega_0 V_0 \partial_y \omega_0 + W_0 \partial_x \omega_0 \partial_z \omega_0 - D_m \partial_x \omega_0 \nabla^2 \omega_0 - f \partial_x \omega \right\rangle_{x,y,z}}{\langle (\partial_x \omega_0)^2 \rangle_{x,y,z}} \tag{5.9}$$

This equation shows that the dynamical velocity is a weighted average of the local flow velocities, source and sink and for periodic boundary conditions the diffusion term is negligible. Averaging along x and z direction only, the equation 5.10 become the vertical dynamical velocity profile:

$$U_d(y, t) = -\frac{\langle \partial_t \omega_0 \partial_x \omega_0 \rangle_{x,y,z}}{\langle (\partial_x \omega_0)^2 \rangle_{x,z}} \tag{5.10}$$

and in the Fourier domain it is:

$$\widehat{U}_d(k_x, k_y, y, t) = \frac{Re\left[ i\partial \widehat{\omega}_0(k_x, K - z, y, t) \overline{\widehat{\omega}}_0(k_x, K - z, y, t) \right]}{k_x \left| \widehat{\omega}_0(k_x, K - z, y, t) \right|^2} \tag{5.11}$$

where $\overline{\widehat{\omega}}_0$ is the complex conjugate of $\widehat{\omega}_0$, $k_x$ and $k_z$ are the streamwise and crosswise wavenumbers and $Re()$ denote the real part. The dynamical velocity $\widehat{U}_d$ is the same as the convective velocity cited by Del Álamo and Jiménez (2009) in regards of Taylor's hypothesis Taylor (1938) on the turbulent flows as fields of frozen vortices advected by the flow. As a matter of fact, the definition of comoving frame and dynamical velocity recalls the Taylor hypothesis concept. In the Taylor's hypotesis (Taylor, 1938), turbulent flow is filled by frozen vortices convected downstream. This happens in weak turbulence regime, when

turbulent fluctuations are small compared to the larger-scale flow and they are advected at a velocity close to the time average of a mean flow velocity $U_m$ at a fixed point. As a first evaluation, it usually happens when the variation of the flow speed due to turbulence is less than $1/2$ of the mean flow speed and eddies can be considered advected with a velocity close to the mean flow velocity $U_m$. However, in figure 5.3 the comparison between the mean velocity profile $U_m$ and comoving frame velocity $U_d$, computed on the spanwise vorticity $\omega_z$, shows that they are not exactly the same. This excess of velocity $U_m - U_d$ is just related to the geometric velocity, as will be assessed in the following. A large excess of velocity, i.e. a large geometric velocity means that we are in strong turbulence regime and the Taylor's hypothesis is not satisfied at all (Fedele, 2014). From its definition 5.3, the dynamical velocity doesn't depend on the desymmetrization method; being governed by the advection phenomena it is computed in the physical space.

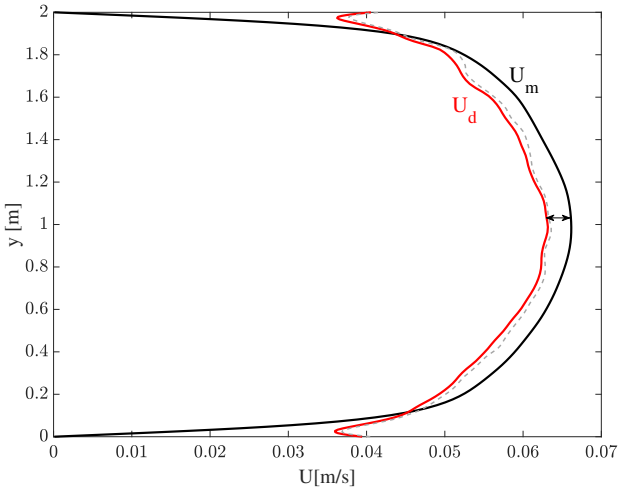


Figure 5.3: Comparison between mean velocity profile $U_m(y)$ (black line), the convective $U_d(y)$ (Taylor) velocity (red line) and its std (gray dashed line) computed on the $\omega_z$ vorticity. The difference proves the presence of a geometric component of velocity

In contrast, the geometric component is affected by the vortices shape deformation. In this global analysis, the geometric velocity is a sort of space average of the geometric velocity of all the vortices within the field, then possibly smoothed and weakened.

### 5.2.2 *Desymmetrization by slicing*

According to §5.1, the coherent structures in a turbulent channel flow are advected downstream with a velocity that depends on both inertia and their shape changing dynamics. The geometric velocity, related to this deformation,

can be interpreted similarly to the fish propulsion and recoil induced by the body deformation (Lighthill, 1960), as a self propulsion of the vortex. Without a desymmetrization process, the motion given by their deformation couldn't be known a priori. The Fourier Slice method enables to unveil the shape of turbulence of the global fields. Slicing returns a symmetry-reduced frame from which the shape-changing of coherent structures can be observed in a reference system fixed with the geometric center of the structure, i.e. without any drift. While the relative velocity between the full motion and the comoving frame is the dynamical velocity, the velocity difference between the comoving frame and the desymmetryzed frame is the geometric phase velocity. The dynamical phase velocity has the meaning of convective velocity and is defined in the ground fixed reference frame; the geometric phase velocity provides the shape deformation and is striclty dependent on the definition of the symmetry-reduced frame. Different slices yield different symmetry-reduced frames. Hereinafter two different slices are chosen to desymmetrize the vorticity field $\omega(x, y, t)$: the first Fourier slice and the 14-th Fourier slice. Before going ahead, it is useful to recall the main steps to perform a symmetry reduction, as explained deeply in §4:

1. Consider the Navier-Stokes dynamical system in the state space $\mathbb{C}^N = \mathbb{R}^{2N}$ of Fourier modes, by Fourier-transforming the Navier-Stokes equations. We moved from the physical space $\mathbb{R}^3$ to the state space of Fourier modes $\mathbb{C}^N$.

2. the state space $\mathbb{C}^N$ has the geometric structure of a fiber bundle as it is made of a base (shape) manifold $B = \mathbb{C}^N|\mathbb{R}$ of dimensions $\mathbb{R}^{2N-1}$ and 1D fibers (direction of translational symmetry (T-symmetry)) attached to any point of $B$ (see figure 4.17).

3. We find a reduction map $\pi$, that is invariant under the T-symmetry and maps trajectories $z(t)$ of $\mathbb{C}^N$ to desymmetrize trajectories $Z_D(t)$ in the base manifold $B$, reducing the T-symmetry.

4. We apply the reduction map $\pi$ and find the motion in the desymmetrized state space, or base manifold $B$.

5. We evaluate the geometric and dynamical velocities that reveals the anatomy of vortices in the desymmetrized frame.

*Step 1 and 2*

The Fourier-transform of the fields finds N Fourier modes $z_n \in \mathbb{C}^N = \mathbb{R}^{2N}$ in the state space, that can be expressed as a truncated Fourier series:

$$\begin{aligned}\omega(x,y,t) =& \omega_0(y,t) + \frac{1}{2}\sum_{m=1}^{N} z_m(y,t)e^{imk_0x} + c.c = \\ &= \omega_0(y,t) + \sum_{m=1}^{N} |z_m(y,t)|\cos(mk_0x + \theta_m(y,t))\end{aligned} \tag{5.12}$$

where $\omega_0(y,t)$ is the mean, $k_0 = \frac{2\pi}{L_x}$ is the minimum wavenumber for the domain of length $L_x$ and $z_m(y,t) = |z_m(y,t)|\, e^{i\theta_m(y,t)}$ is the m-th complex Fourier mode with amplitude $|z_m|$ and phase $\theta_m$. In differential geometry, the evolution of the vector $z(y,t) = \{z_m(y,t)\} = (z_1(y,t), z_2(y,t), ..., z_m(y,t))$ is the orbit that travels in the state space $P \in \mathbb{C}^n$ and it represents the dynamics of the full system.

*Step 3 and 4*

The choice of the slice. Different slices yield different desymmetrized frame and there is not a unique way to reduce the symmetry. No one knows a priori the best Fourier slice, a series of test is needed. "A good reduction requires that the amplitude of $z_j$ to be dominant in comparison to the other Fourier components" (Fedele et al., 2015). Moreover, a proper choice of the slice should yield a reduced field in which the shape-changing dynamics of the vortices can be observed without a drift. The desymmetrized orbit $Z(y,t)$ is defined by the following expression:

$$Z = \Pi_j(z) = \{Z_m\} = \left\{ z_m \left( \frac{\overline{z_j}}{|z_j|} \right)^{m/j} \right\} = \left\{ |z_m|\, e^{i\phi_m} \right\}, \tag{5.13}$$

whose phases are:

$$\phi_m = \theta_m - \frac{m\theta_j}{j} \tag{5.14}$$

The reduction map $\Pi_j(z)$ is a function of the number of slices chosen to perform the projection. The number of slices is defined by the value of j: with $j = 1$ the desymmetrization scheme was achieved with the First Fourier Slice, while with $j > 1$ it was an high order Fourier slice.

The reduction map $\Pi$ applied to $z(y,t)$ shifts the full trajectory by the total shift

$$\ell_{tot} = -\frac{\theta_m}{k_0 j} \qquad j \geqslant 1, \tag{5.15}$$

that returns the desymmetrized complex trajectory:

$$Z_m = z_m e^{-imk_o \ell_{tot}} \qquad m = 1, ..., N \tag{5.16}$$

Coming back to the physical space we can write the desymmetrized vorticity field as:

$$\omega_D(y,t) = \omega_0(y,t) + \sum_{m=1}^{N} |z_m(y,t)| \cos(mk_0 x + \Phi_m(y,t)) \tag{5.17}$$

*Step 5*

The total shift related to the total phase $\theta_m$ is the sum of the dynamical ($\ell_{dyn}$) and geometric shift ($\ell_{geom}$):

$$\ell_{tot} = \ell_{dyn} + \ell_{geom} \tag{5.18}$$

We can get a second definition of the corresponding velocities: the total, dynamical and geometric velocities are respectively

$$U_{tot} = \frac{d\ell_{tot}}{dt} \tag{5.19}$$

$$U_{dyn} = \frac{d\ell_{dyn}}{dt} \tag{5.20}$$

$$U_{geom} = \frac{d\ell_{geom}}{dt} \tag{5.21}$$

If $U_{dyn}$ is known by 5.3, from 5.19 we can derive the dynamical shift:

$$\ell_{dyn}(y,t) = \int_0^t U_{dyn}(y,\tau) d\tau \tag{5.22}$$

Similarly, once the slice has been chosen, the geometric phase velocity yields from the desymmetrized components

$$U_{geom}(y,t) = -\frac{< \partial_t \omega_D \partial_x \omega_D >_x}{< \partial_x \omega_D \partial_x \omega_D >_x} \tag{5.23}$$

and the geometric shift comes from:

$$\ell_{geom}(y,t) = \int_0^t U_{geom}(y,\tau) d\tau \tag{5.24}$$

The geometric drift and velocity can be also evaluated from, respectively: $\ell_{geom} = \ell_{tot} - \ell_{dyn}$ and $U_{geom} = U_{tot} - U_{dyn}$ that is consistent with the previous relations.

The application of the above procedure to the spanwise vorticity field allows to get the results that are summarized in figures 5.4 and 5.5, related to,

respectively, the slice $j = 1$ (fig. 5.4) and $j = 14$ (fig. 5.5). More in detail, the first two panels of both figures, show, respectively, the field evolution in space and time as seen in the earth fixed lab frame (left panel) and in the comoving frame (center panel). They shown two different ranges of time of the same vorticity field $omega(x, t)$ (averaged in y and z direction): in figure 5.4 field goes from $t = 0s$ to $t = 100s$ while in figure 5.5 from $t = 100s$ to $t = 200s$ in order to empathize the desymmetry features, shown in the third panel. Despite the dynamical velocity is quotiented out, in the comoving frame we still observe a mean velocity field. The latter is removed in the desymmetrized frame (third panel of each figure). The motion in desymmetrized frame depends on the slice chosen. Since the choice of the Fourier slice is arbitrary, the space time evolution shown in figure 5.4 by considering the first Fourier slice yields an imperfect reduction in the desymmetrized frame; the field shows a weak deformations. It means this slice is not able to project all the full motion on it. High order slice, in particular the 14-th, is then used to reduce the vorticity field and the results are shown in the third panel of figure 5.5 with the drift almost disappeared.

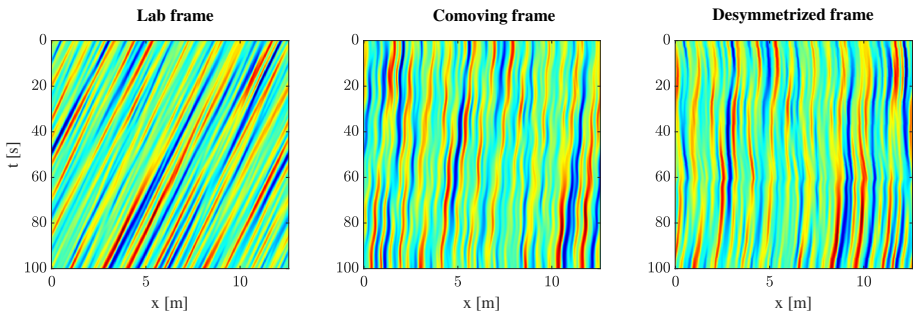


Figure 5.4: Symmetry reduction of $\omega_z$ with the first Fourier slice. Space-time evolution in lab frame (left) $\omega(x, t)$, comoving frame $\omega(x - \ell_{dyn}, t)$ (center), desymmetrizzed frame $\omega(x - \ell_{dyn} - \ell_{geom}, t)$(right)

By summarizing, figures 5.4 and 5.5 are used to assess that:

- in the lab frame there is a high drift given by the sum of the dynamical and the geometric drift. This drift potentially obscures the shape of the vortices evolving in the field.
- in the comoving frame there is still a drift given by the geometric component;
- in the desymmetrized frame the drift disappears and the motion is only due to the pure deformation of the coherent structures.

In figure 5.6 total, dynamical and geometrical shift and velocities are shown for both the reduced-symmetry frames: first and 14-th Fourier slices. The

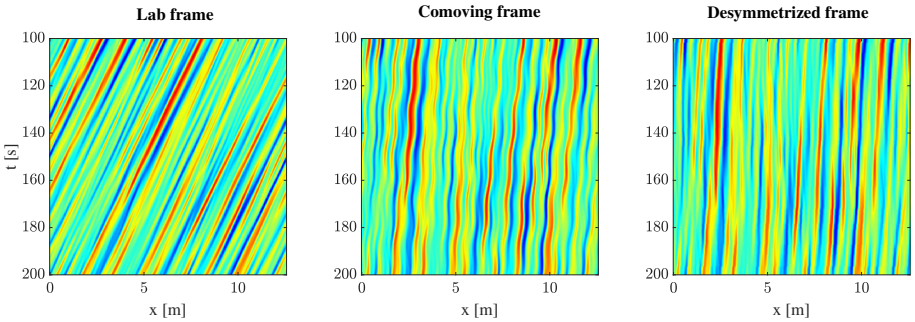


Figure 5.5: Symmetry reduction of $\omega_z$ with the 14-th Fourier slice. Space-time evolution in lab frame (left) $\omega(x,t)$, comoving frame $\omega(x-\ell_{dyn},t)$ (center), desymmetrizzed frame $\omega(x-\ell_{dyn}-\ell_{geom},t)$(right)

dynamical velocity and shift (blu lines) are the same while the total velocity and shift (black lines) are affected by the choice of the slice (eq. 5.15). The geometric drift $\ell_{geom}$ and the associated velocity $U_{geom}$ are different, confirming the importance of the correct choice of the slice. The reduction achieved with the 14th slice (see figure 5.6 (bottom)) yields more suitable results in term of shifts and velocity. Even if the dynamical velocity is almost equal to the total one, the geometric velocity is greater than zero, even if slightly. In figure 5.6, velocities $U_tot$ and $U_{geom}$ show lots of oscillations. It is caused by the derivative of the $\ell_{tot}$ and $\ell_{geom}$, while the $U_{dyn}$ (see equations 5.19) is obtained by using the equation 5.3.
It is worth to remark that the reduction was performed on the global spanwise vorticity field: the dynamical phase velocity has the meaning of convective velocity, while the geometric phase velocity is the mean velocity due to the shape-changing of all vortices. This implies that the deformation of each vortex contributing to the mean geometric speed, produces a motion which does not necessarily have the same direction of the mean motion. The velocity contribution of each vortex induced by its own shape deformation can be summed up with a destructive interference so that the mean geometric velocity can results near to zero.

This motivates why the geometric shift and velocity appear to be close to zero (see figure 5.6 (red lines)).

### 5.2.3 *Group orbits and desymmetrized trajectory*

A whole representation of the $\mathbb{C}^N$ dynamical system in the space state is a pure abstraction of thought; a subspace representation becomes then a must. Group orbits are a geometric representation of the dynamical system in the complex domain. As mentioned in Chapter §4, in the state space only a subspace of

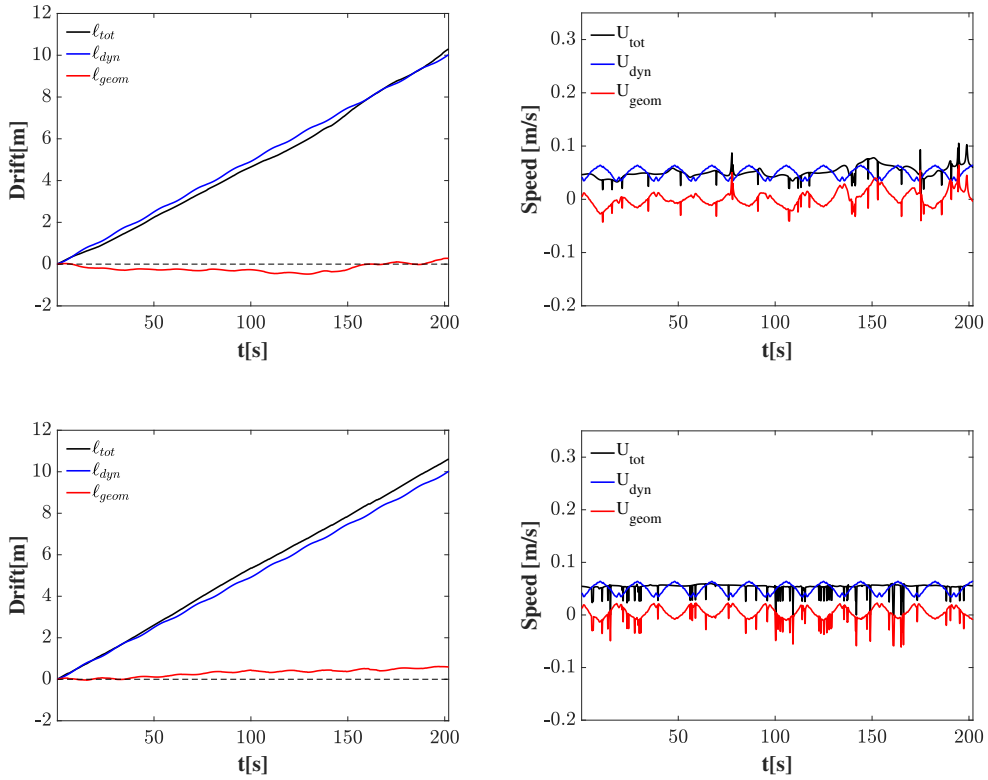


Figure 5.6: Total, dynamical and geometric drift and phase speeds of reduced using First (top) and 14-th Fourier slices(bottom)

the entire $\mathbb{C}^N$ system can be represented by choosing, among infinite possible coordinate systems, three different Fourier modes or a combination of their real and imaginary parts. Each combination returns different shapes of group orbits as shown in figures 5.7 and 5.8 where the The 14th Fourier slice was applied on the spanwise vorticity $\omega_z$, averaged in y-direction. The group orbits are composed by:

- the full trajectory $z(t) = \left\{|z_m(t)|\, e^{i\theta_m(t)}\right\}$ (black lines),
- the fibers (red lines) attached to any points of the full trajectory functions of phase $\theta_m$,
- the comoving trajectory (green lines)$Z_{com}(t) = z(t)e^{-imk_0\ell_{dyn}}$,
- the desymmetrized trajectory (blue lines) $Z(t) = z(t)e^{-imk_0\ell_{tot}}$.

The base manifold is not drawn but it can be imagined as a complex hyperplane with a intricate shape that cuts the group orbits where the desymmetrized trajectory is projected.

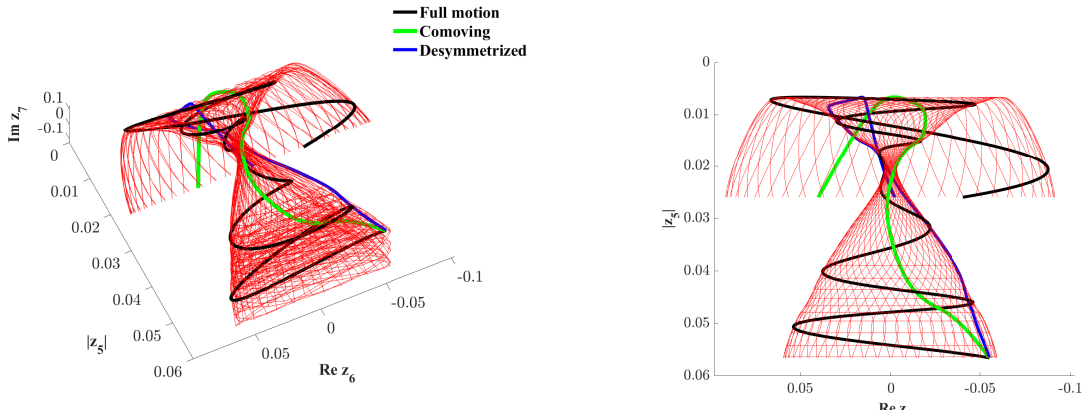


Figure 5.7: Groups orbits in a 3D subspace of $\mathbb{C}^n$ composed by $|z_5|$, $\Re z_6$, $\Im z_7$ : spanwise vorticity field $\omega_z$. the full trajectory $z(t)$ (black lines), the fibers (red lines) attached to any points of the full trajectory , the comoving trajectory (green lines) and the desymmetrized trajectory (blue lines

As explained in Chapter 4 (sections §4.4.1) and in this Chapter (section §5.2.2), the transition between lab frame, comoving frame and desymmetryzed frame provides respectively the dynamic $x(t) - \ell_{dyn}(t)$ and total shift $x(t) - \ell_{dyn} - \ell_{geom}(t) = x(t) - \ell_{tot}$. These shifts are hyper-dimension phase shift (eq. 5.15), on the fibers; the fibers are the geometric representation of the symmetry of the dynamical system. The depiction of the group orbits can be more helpful in understanding these concepts where the transition between the trajectories is represented by a space shift on the fibers. In particular, they can help to understand how much is complex the dynamical system in the complex domain. They are the geometric representation of the mathematical formulation without a proper physical meaning.

## 5.3 INSIDE THE FLOW: SYMMETRY REDUCTION OF THE TRACKED VORTICES

In this section the method created to track a discrete system of vortices is explained. The goal consists in finding a way to follow vortices in order to do a more detailed analysis of the vortex behavior. In particular, the aim of this section is to add details in the characterization of the vortices, going inside the dynamical system and revealing how much the shape-changing and the interaction between vortices contribute to their motion. The characterization of turbulence was enriched by going into the vorticity field following each vortex in time and space. The analysis was executed on the vorticity field $\omega_z$ averaged in z direction $\omega = \omega_z(x, y, t)$, which is the same field used for the previous

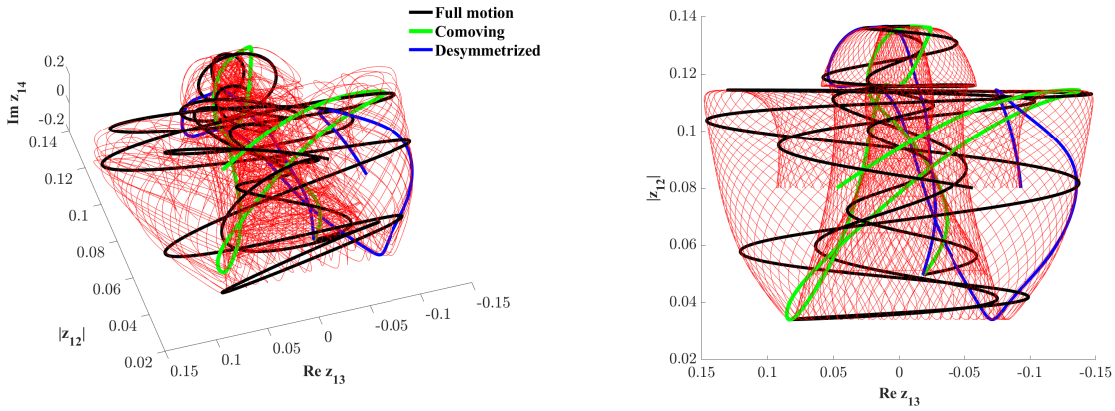


Figure 5.8: Groups orbits in a 3D subspace of $\mathbb{C}^n$: spanwise vorticity field $\omega_z$, in the subspace composed by $|z_{12}|$, $\Re z_{13}$, $\Im z_{14}$

global analysis. Consider the *vorticity transport equation* for three-dimensional incompressible and viscous flow with a uniform and constant viscosity

$$\frac{D\omega}{Dt} = (\omega \cdot \nabla)\, u + \nu \nabla^2 \omega. \tag{5.25}$$

The term $(\omega \cdot \nabla)$, called stretching and tilting, is connected with the contribution of vortex deformation (e.g atmospheric tornado or drainage vortex into a tank, see figure 5.9 ). They come directly from the conservation of angular momentum, seen in chapter §3, and are induced by the high gradient of velocity aligned to vorticity vector. Stretching is given by the parallel component while tilting by the orthogonal one.

The use of a two dimensional field $\omega_z(x, y, t)$ (hereinafter referred to as $\omega(x, y, t)$), averaged in z-direction, partially hides the vortex deformation in z-direction; however, the informations about the stretching and tilting components are not completely lost. They are potentially hidden in the vorticity value in the plane xy, as a consequence of the solution of the whole 3D field, i.e. equation 5.25 and the subsequent average along z.

In order to identify an interesting system of vortices, within an area with an homogeneous and isotropic turbulence, the zone near the walls is removed. A contour function, containing the isolines of the matrix $\omega(x, y, t)$, enables to highlight and track vortices in their space-time motion in the channel. Nevertheless, the use of the $\omega(x, y, t)$ is not the most suited approach to define coherent vortical structures in general, because vorticity also characterizes shear layers. Later it will be shown that the Okubo-Weiss criteria indicate that for the cases under examination vorticity can be used for tracking vortices. However one of the the goal of this dissertation was to create a numerical method of tracking. Once it works it can be applied to every kind of physical quantities.

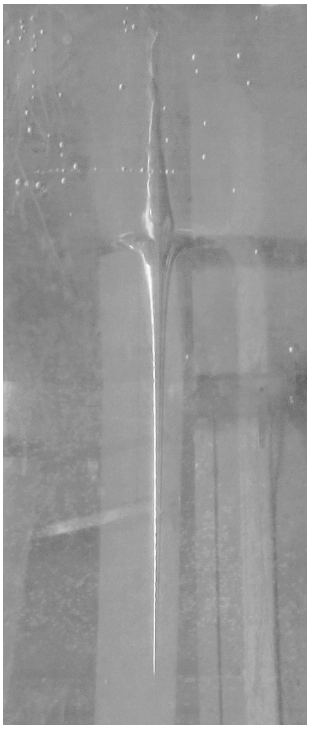

Figure 5.9: Water-Drainage air vortex in a circular tank - CNR-INM

### 5.3.1 *Methology of tracking vortices*

For the tracking of the vortices we take into account the periodicity of the channel flow along the horizontal direction.

The tracking procedure is based on the following steps:

- step 1) a threshold value $\omega_{lower}$ on the vorticity value is used to filter out the small vortices in the field and to emphasize the larger ones (see figure 5.10);
- step 2) at the time $t_0$ all the remaining vortices have been labeled through a sequential number "$n = 1, 2, ...$" based on the initial position along the channel (see figure 5.10b ).
- step 3) a well defined vortex n is selected and the maximum initial value is measured;
- step 4) based on a given minimum value of contour function (corresponding to 10% of the maximum value at time $t_0$), a squared window is designed and moved with the velocity field estimated as average of the particles velocity within the window.

- 5) At each time step, the maximum vorticity and the corresponding position within the window is identified allowing the update of a novel window according to the step 4 (see figure 5.11)

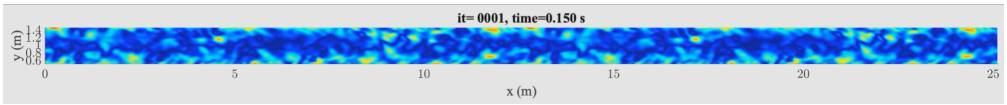


(a) Vorticity field unfiltered

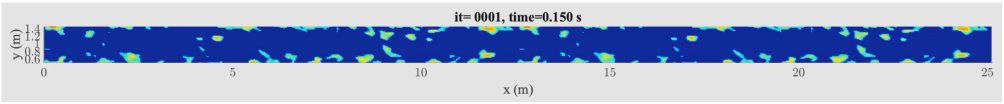


(b) Vorticity field filtered

Figure 5.10: Graphic comparison between filtered and unfiltered vorticity field

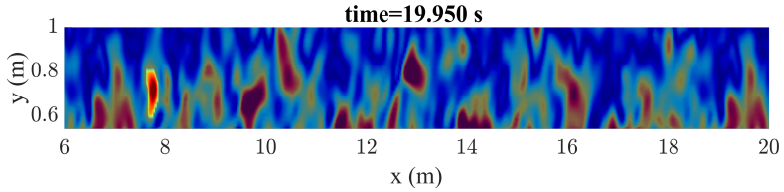


Figure 5.11: One isolated vortices during its motion

The above procedure, repeated for all the vortices within the field, enables tracking the vortices in space and time. This allows also for the identification of the geometrical properties:

- surface
- moments of inertia

necessary for understanding the shape deformation of the vortex core, and the kinematic properties,

- maximun of vorticity in time and space
- velocity and acceleration

essential for a full comprehension of the vortex dynamics. In particular :

- Zero moment-Geometric center
- First moment-Center of vorticity
- Second moment-Vortex's area
- Third moment-Inertial moments

corresponding to:

$$\begin{aligned} X_g &= \frac{\int x\,dS}{S} \\ Y_g &= \frac{\int y\,dS}{S}, \end{aligned} \qquad \text{Geometric center} \tag{5.26}$$

$$\begin{aligned} X_v &= \frac{\int x\delta\omega\,dS}{\int \delta\omega\,dS} \\ Y_v &= \frac{\int y\delta\omega\,dS}{\int \delta\omega\,dS} \end{aligned} \qquad \text{Vorticity center} \tag{5.27}$$

where $\omega$ is the vorticity distribution in Cartesian coordinates. The matrix of the moment of inertia in Cartesian coordinate is:

$$I = \begin{bmatrix} I_{xx} & I_{xy} & 0 \\ I_{xy} & I_{yy} & 0 \\ 0 & 0 & I_{zz} \end{bmatrix} \qquad \text{Inertial moments matrix} \tag{5.28}$$

with

$$\begin{cases} I_{xx} &= \int (y - y_v)^2 dS \\ I_{yy} &= \int (x - x_v)^2 dS \\ I_{zz} &= Ixx + Iyy \\ I_{xy} &= -\int (x - x_v)(y - y_g) dS \end{cases} \tag{5.29}$$

where the $x_v$ and $y_v$ are the coordinates of the center of vorticity and $I_{xz}$ and $I_{yz}$ are equal to zero since we are in the xy plane. Diagonalizing the matrix of moment of inertia, the principal moments of inertia and the rotation angle $\alpha$, associated with the rotation of the principal axis reference system with respect to the Cartesian axis were found, being respectively the eigenvalue and the eigenvector of principal axes :

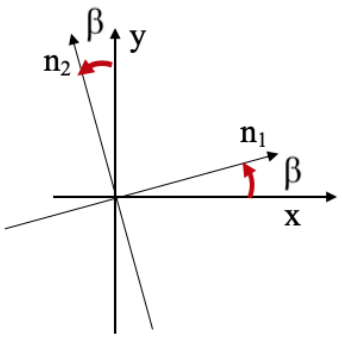


Figure 5.12: Angle of rotation $\alpha$ between Cartesian and principal axis

The i-th eigenvector is given by:

$$n_i = \begin{Bmatrix} X_i \\ Y_i \\ 0 \end{Bmatrix} \tag{5.30}$$

so the $\beta$ rotation is:

$$\beta = arctg(\frac{Y_i}{X_i}) \tag{5.31}$$

Inertial moments are necessary for two different considerations. The first is connected with the vortex shape. In fact $I_{xx}$, $I_{yy}$ or $I_{11}$ and $I_{22}$ are the measures of how vortex area is distributed, in space and time, along the axes as schematized in figure 5.13

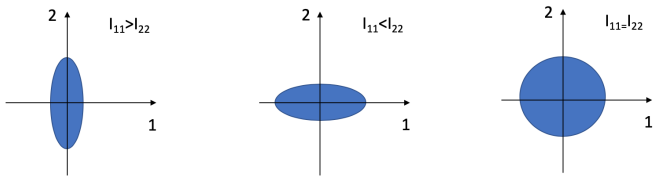


Figure 5.13: Inertial Moments as a proof of area distribution

The $I_{zz}$ and $I_{33}$ are connected with the conservation of the angular moments and the rotation of vortex:

$$L = I\omega = I \begin{bmatrix} 0 \\ 0 \\ \omega_z \end{bmatrix} = I_z \omega_z \tag{5.32}$$

Finally, the circulation $\Gamma$ was calculated

### 5.3.2 *3 vortices*

During the evolution of the vortices in the field, we found of particular interest the evolution of two vortices that during their motion merge to originate a third vortex. This particular setup will be analized in the following: the analysis of the single vortex tells us how it deforms over time, the interaction analysis between vortices is useful to understand their mutual influence as shown in figure 5.14.

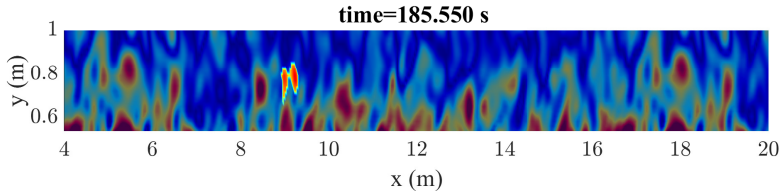


Figure 5.14: Two isolated vortices put together to study their interaction

More precisely, there are two vortices (called 1 and 2 as shown in figure 5.14) that meet and merge together during their motion creating a third one

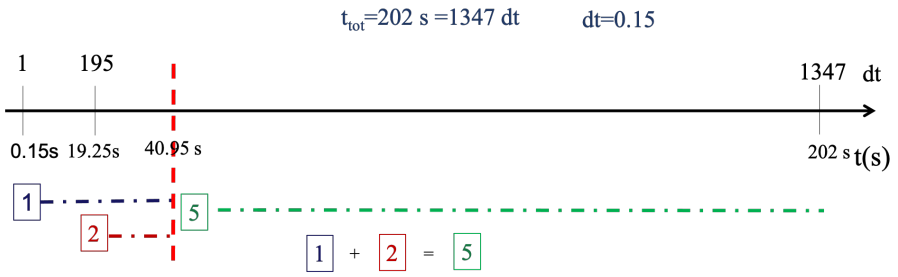


Figure 5.15: Temporal scheme of vortices evolution in time

called 5. The timing of their motion is shown in figure 5.15, with the vertical red line shows the time instant of merging.

*Kinematic properties*

Figure 5.16 shows the position of the maximum of vorticity 'max' (dashed line), of the geometric center 'g' (solid line) and of the center of vorticity 'v' (dotted line) for the three vortices $1, 2, 5$ (blu, red, green, respectively). Their evolution in channel flow is also shown in this video.

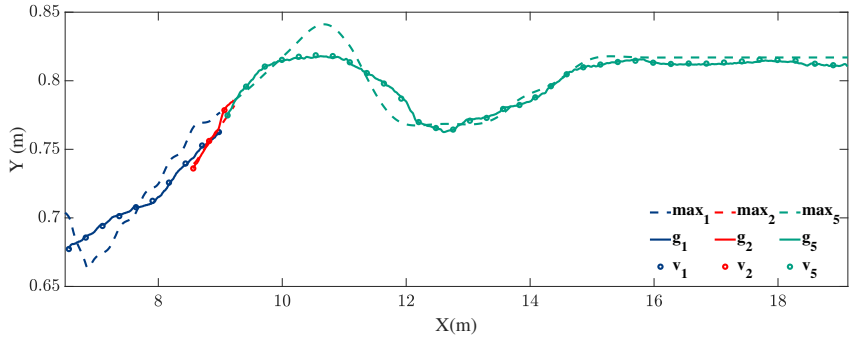


Figure 5.16: Vortices displacements in the channel. For any vortex there are the displacement of the maximum of vorticity (max), the geometric center (g) and the center of vorticity (v)

The motion of the geometric center (g) and of the center of vorticity (v) coincides; however it differs from that of the maximum of vorticity. This is probably related to the small size of the vortex with respect to the discretization used as well as to the value of $\omega_{lower}$ chosen. A more refined technique will be used as a next step so to emphasize the differences related to the local value of the vorticity. In any case, in the actual analysis, from here on, we will report only the quantities related to the center of vorticity.

### 5.3.3 *Vortices interaction*

Figure 5.17 shows displacements (panel (a)) of the three vortices in time along x (first panel) and y ( second panel) as well as their trajectory within the channel (third panel). To proper understand their evolution, the time history of the vorticity in the center of the vortex is also reported in panel (b) of the same figure 5.17.
The motion of the first two vortices, before and after their merging is dominated by the mean longitudinal flow which advects the vortices along the longitudinal direction of the channel. In contrast, their transversal motion, i.e. along the wall-normal direction, although bounded between 0.66m and 0.88 m (which is still closer to the center of the channel than to the wall), shows a clear trend to approach the center of the channel, at least before the merging time instant. Then, we observe an oscillation in the wall-normal position of the resulting vortex (green line), at a first glance associated with the variation of the vorticity in the center of the vortex field (see panel (b)) and probably related to the interaction phase. However, after a first oscillation, the vortex continues its travel in a rectilinear path.

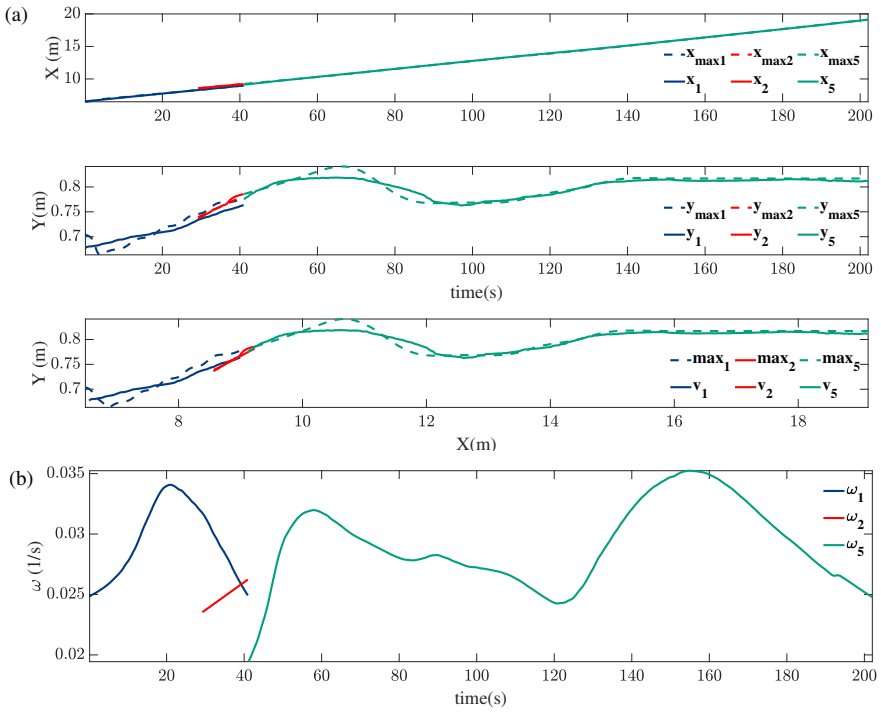


Figure 5.17: Vortices displacements (a) of three vortices compared with the vorticity of the center of vorticity (b). The center of vorticity (solid lines) and maximum of vorticity (dash line)

However, by using the kinematic and geometrical information reported in figure 5.17 and 5.18, we can further inspect the dynamics of this vortical structure. In particular, the motion of vortex 1 can be split in two parts: the first part going from $t = 0$ s to $t = 20$ s and the second from $t = 20$ s to $t = 30$ s. In the first part (figure 5.18), the vorticity $\omega_1$ increases , while its surface $S_1$ decreases. This behavior can be related to the tilting phenomenon. By tilting, indeed, the vortex could reduce its projected area in the x-y plane, which is the one given by the average procedure along z, and increase the mean value of the vorticity: the vortex tube becomes thinner and the vorticity larger. The angle of rotation $\beta$ in the xy plane is constant (see fig 5.19, that is Cartesian and principal axes are not changing in time. Since $I_{22} > I_{11}$ the vortex is stretched ( see fig. 5.19 (i)).

In the second part, after vorticity has reached its maximum value, it decreases according to the trend of the vortex surface. As a consequence, the shape of the vortex is reducing in size and amplitude. It is interesting to note that during the last stage of the diffusion process the vortex assumes a symmetric shape, i.e. $I_{22} = I_{11}$. However the principal axis reference system is rotating with respect to the fixed ground axis which needs a further investigation.

The second vortex of the system has a quite short evolution before merging with the previous one and originating vortex 5. However, its geometrical and kinematic description is important to understand the borning of vortex 5. This is evident by observing the results in figure 5.16 and 5.17. The merging of vortex 1 and 2 occurs through various stages and some energy transfer occurs from 1 to 2. This becoming evident around t=42s when the intensity of the vorticity of 2 is larger than that of 1. The time history of the maximum vorticity, indeed shows as the vortex 5 comes directly from vortex 2, with vortex 1 weakening and providing a negligible contribution in terms of the maximum vorticity of the vortical structure. (Meunier et al., 2005) analysed the interaction of two 2D identical co-rotating vortices and identified four different stages in merging process. The first stages corresponds to the condition when the separation distance between two centres of vorticity remain constant while the core size increases by viscous diffusion of vorticity. When the critical core size is exceeded the vortices become unstable and merge, leading to a rapid decrease of the their distance. This second stage appears to be driven by advection of vorticity. The merging is not complete because the two vortices are next to each other but still have two separate centre of vorticity. The diffusion of vorticity and the rotation of the rotation center lead to an axisymmetrization of the vortex center in the third stage. In the fourth and last stage, the vortex diffuses again due to viscosity and its size increases with time. The merging phenomenon highly depends on the ration between the core size and the separation distance. In this case vortex 1 and 2 are not equal vortices. Their merging can be considered the so-called "straining merging" that happens when a small vortex (vortex 2) gets close to a strong vortex (vortex 1) and it is

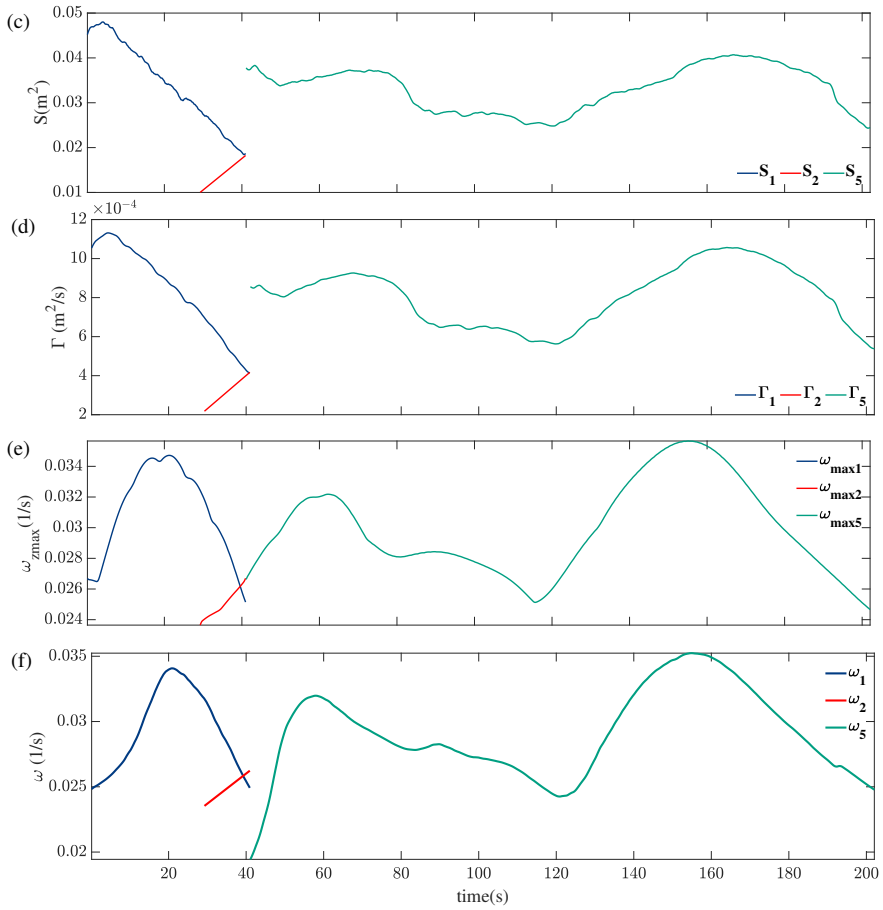


Figure 5.18: Vortices surfaces and its time derivative (c), the circulation Γ (d) and the maximum of vorticity (e) as a function of time and compared with the vorticity of the center of vorticity (f)

stretched and transformed into a vortex sheet which is wrapped around the larger vortex. As shown in figure 5.19 the circulation Γ of vortex 5 is the sum of that vortex 1+2. However, the interaction between vortex 1+2 is meaningful in terms of the geometrical parameters time history, indicating a dominant role of the shape deformation both at the merging instant (see the jump which characterizes the several quantities) and during the whole evolution of vortex 5. In particular, for the latter, we can observe both the geometric (transversal position, surface and inertia moment) and the dynamic quantities change almost in phase as a possible consequence of the shape deformation. Further a periodic behaviour with a period of about 80 s is observed.

Despite a objective identification of vortices is still unanswered, to be further sure that the use of vorticity in this 2D vortex tracking was a suitable method to identify coherent structure, the Hua-Klein criterion (HK) (Hua and Klein (1998)) was applied to vortex 5, the longest in terms of time history and the

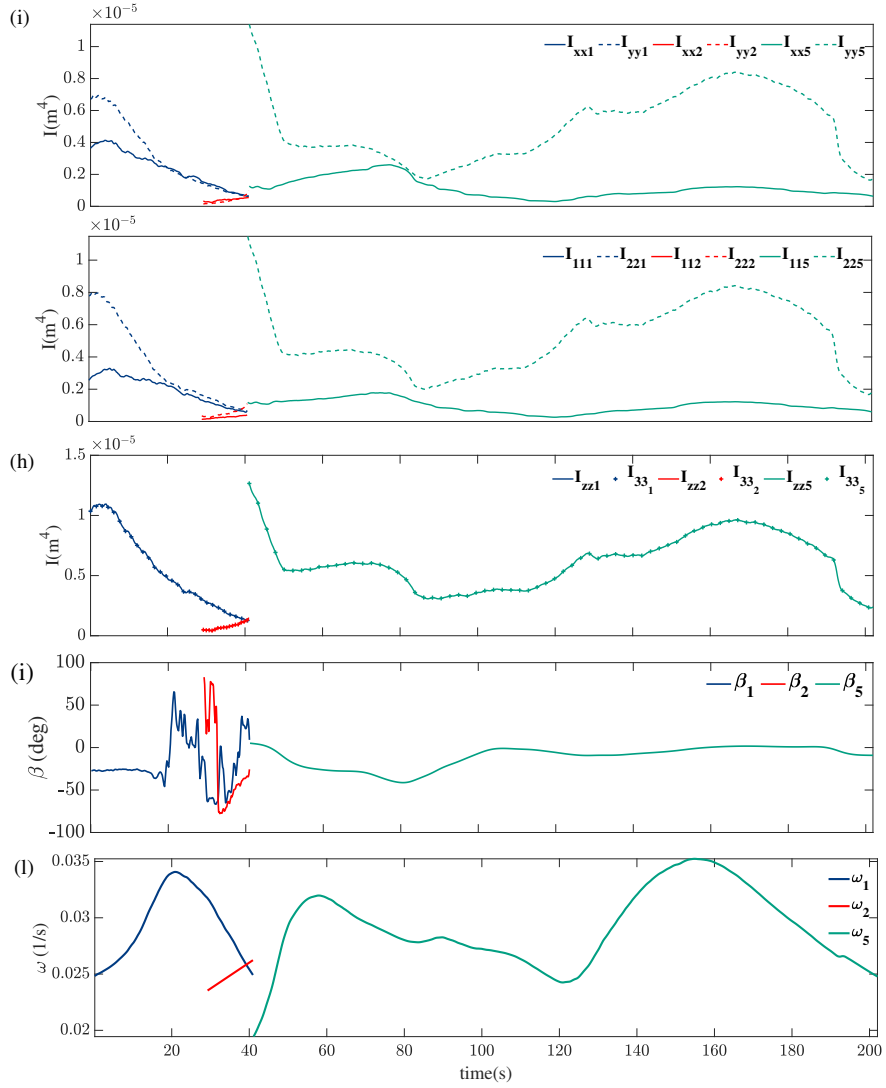


Figure 5.19: Cartesian and principal moments of inertia (g and h), the rotation angle $\alpha$ (i) as a function of time compared with compared with the vorticity of the center of vorticity (l)

farthest from the wall. In particular, the Hua-Klein criterion is an extension of the Okubo-Weiss criterion (OW), that is more appropriate for steady flow. Both represent exact criteria for partitioning fluid with different dynamical properties: strain dominated regions from vorticity dominated ones. The OW parameter is:

$$OW = \lambda_0 = \frac{1}{4}(S_n^2 + S_s^2 - \omega^2) \tag{5.33}$$

where $S_n = \partial_x u - \partial_y v$ are the stretching rate, the $S_s = \partial_x v + \partial_y u$ the shear component of the strain and $\omega$ the relative vorticity. The OW weights the

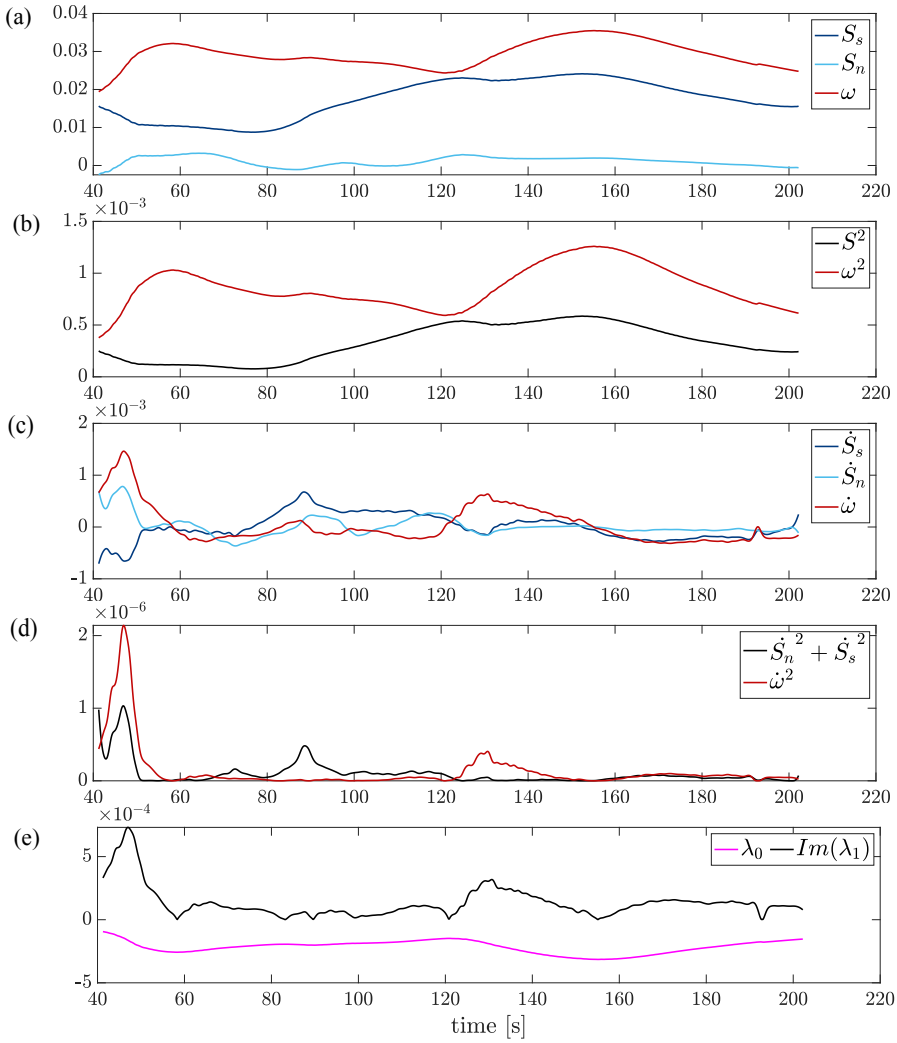


Figure 5.20: Okubo-Weiss and Hua-Klein parameters and terms evaluated in the centre of vorticity of Vortex 5 as a function of time. In particular (a) $S_s$ (blu line), $S_n$(azure line) and $\omega$ (red line), (b) the Okubo-Wiess terms $S^2 = S_n^2 + S_s^2$ (black line) and $\omega^2$ (red line), (c) the Hua-Klein terms $\dot{S}_s$ (blu line), $\dot{S}_n$ (azure line) and $\dot{\omega}$ (red line), (d) $\dot{S}_n^2 + \dot{S}_s^2$ (black line) and $\dot{\omega}$ (red line) terms and (e) $\lambda_0$ (magenta line) and $Im(\lambda_1)$ (black line)

strain properties of the flow against the vorticity properties and thus separates vorticity-dominates areas from strain-dominated one (Vortmeyer-Kley et al., 2016). While the OW is related to the eigenvalues of the Eulerian velocity gradient tensor, the HK is defined as the largest of the eigenvalues of the acceleration gradient tensor. Thus the HK criterion adds the not stationary effects :

$$HK = \frac{1}{4}(S_n^2 + S_s^2 - \omega^2) \pm \frac{1}{2}\sqrt{\dot{S}_n^2 + \dot{S}_s^2 - \dot{\omega}^2} \tag{5.34}$$

with $\lambda_1 = \frac{1}{2}\sqrt{\dot{S}_n^2 + \dot{S}_s^2 - \dot{\omega}^2}$ . In figures 5.20 all the terms of HK equation 5.34, evaluated in the centre of vorticity of Vortex 5, are plotted separately in order to understand their own role. In figure 5.20 (a) are shown respectively the Okubo-Weiss terms, where the vorticity $\omega$ (red line) appears to be greater than the shear stress $S_s$ (azure line), the stretching rate $S_n$ (blue line) and thus then the sum of squares $S^2 = S_n^2 + S_s^2$ (black line) in figure 5.20 (b). The value of the OW $\lambda_0$ is shown also in 5.20 (e) (magenta line) that is always less than zero: it means vorticity exceeds the amplitude of strain that usually happens in the vortex core. The derivative of vorticity $\dot{\omega}$ is greater than the strain derivative and also then the sum of squares $\dot{S}_n^2 + \dot{S}_s^2$ in some ranges of time. As a consequence $\lambda_1$ is imaginary as shown in figure 5.20 (e) (black line). In particular, taking into account also the value of surface in figure 5.18 (c) the dynamic of the vortex can be split in some time regions. From $t = 40s$ to around $t = 50s$ there is the completion of the merging phase where the stretching $S_n$ and vorticity $\omega$ increase while the shear $S_s$ and the surface decrease. The lack of symmetry is visible also in the value of principal inertial moments of vortex 5 in figure 5.19 where $I_{22} >> I_{11}$. At $t = 50s$ the time derivatives $\dot{\omega}$ and $\dot{S}$ reach the maximum. From $t = 50s$ to $t = 70s$ the variation of vorticity $\dot{\omega}$ decreases together with the variation of $\dot{S}^2$ remaining greater than the last while the surface S in figure 5.18 (c) (green line) increases reaching a first maximum at $t = 70s$. At $t = 70s$ a dissipation process starts until to $t = 122s$: $S_s$ increases while the vorticity $\omega$ and the surface decrease; the time derivative of vorticity is less than the strain ones so that $\lambda_1$ is imaginary. From $t = 120s$ to the end there is another increment of vorticity and the surface of the vortex. Looking at this video from $t = 100s$ there is another vortex behind vortex 5 that is coming from the wall and, while it is moving towards the centre of the channel, it interacts with vortex 5 and gives it energy.

### 5.3.4 *Symmetry reduction of tracked vortices*

Because of the observations done on the tracking of vortices, they seem good candidates for the application, for the first time, of the symmetry reduction method to a single vortex. From the conceptual point of view, it is formally identical to the method described in section 5.2 for the global field, and then we do not linger on that.
In this way we trust on the possibility to extract the two mean velocity components of the vortex, related to advection (dynamical velocity) and to shape deformation (geometric velocity).
As total velocity of the vortex, $C_{tot}$, we considered the velocity of the vortex center; while $C_{dyn}$ has been calculated through formula 5.3 applied to the vorticity field.
It is interesting to observe that, in this case, the temporal and the spatial derivatives have been estimated on the global field and then filtered through the application of the window fitting the vortices and following them.
This corresponds to the calculation of time derivative in an eulerian way, but in the instantaneous position of the vortex. From $C_{tot}$ and $C_{dyn}$, the geometric velocity comes directly as $C_{geom} = C_{tot} - C_{dyn}$. The corresponding shifts ($\ell_{tot}$, $\ell_{dyn}$, $\ell_{geom}$ ) are directly calculated as the time integral, according to equations 5.15, 5.22 and 5.24.

Figure 5.21 shows the trends of extracted velocity components (left column) and of the corresponding shifts (right column) for all the three vortices: 1 (first row), 2(second row) and 5 (third row).
In contrast to the results observed for the global analysis, here the geometric velocity component assumes a value which is comparable with the dynamic velocity component, for all the vortices considered, i.e. $C_{tot}/C_{dyn}$ almost equal to 2. This means that the vortex motion is equally influenced by the shape deformation and the flow advection.
A possible explanation of the different local/global behavior lies, in our thinking, in the different "glasses" used for the analysis. Global analysis is looking from far away, by averaging the behavior of the whole flow field, which includes some vortices, but also non vortical structures, the latter dominated by the advection. In contrast, local analysis is looking only at the details of the local flow within a single vortex and then properly weighting the advection and the shape deformation of the local flow structure.
Once the dynamic and geometric velocity components have been identified, we can look at each vortex with an even more sophisticated "optical instrument", a filter applied on the global field, able to properly follow the single vortex and then observe closely its structure and its dynamics.
In order to understand this theoretical concept, figure 5.22 shows the space-time evolution of each vortex (1, 2, 5 from top to bottom, respectively) composing the vortical structure under investigation, in the three reference systems identified

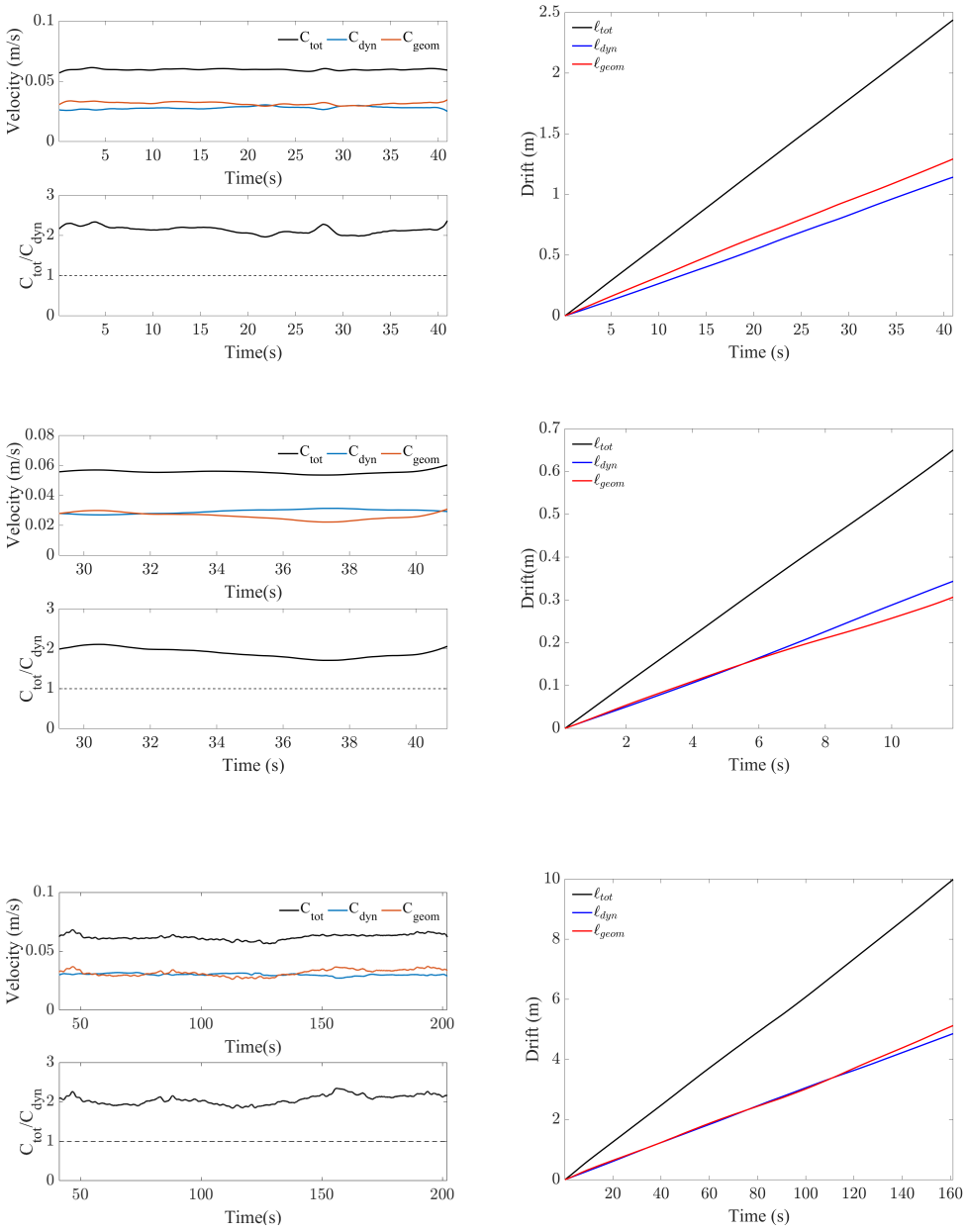


Figure 5.21: Velocities (left) and shifts (right) decomposition. Vortex 1 (top), Vortex 2 (center), Vortex 5 (bottom)

in section §5.2: earth-fixed lab frame (first column), comoving frame (second column) moving with the only dynamic velocity component and desymmetrized frame (third column), moving with the whole $C_{tot}$ and then closely following the vortex. Fourth column shows an enlarged view of the vortex in the last reference frame (dashed rectangle in the desymmetrized frame), which helps

to understand the variation of the vorticity strength along x, meaning that the vortex is changing its shape.
In particular, in Vortex 5 ,the reduction of the vortex surface seems to imply, as a consequence, an increase in the vortex strength.
This view is only partial; the whole shape deformation also depends on the deformation along y that will be fuhrer confirmed and highlighted in the next Chapter §6 of this thesis. However, the present analysis assesses that the vortex shape deformation induces a variation of the average velocity field of the vortex itself.
Then, according to the results of the global analysis and to those results shown in picture 5.21 in the lab frame the drift is given by the sum of the dynamic and geometric shifts. In the comoving frame, a smaller drift is given by the geometric component that is produced by the shape changing of the vortex. In the geometric frame the drift disappears and the system of reference is moving with the total velocity of the vortex. In the last frame, the pure deformation of the vortex is now revealed.

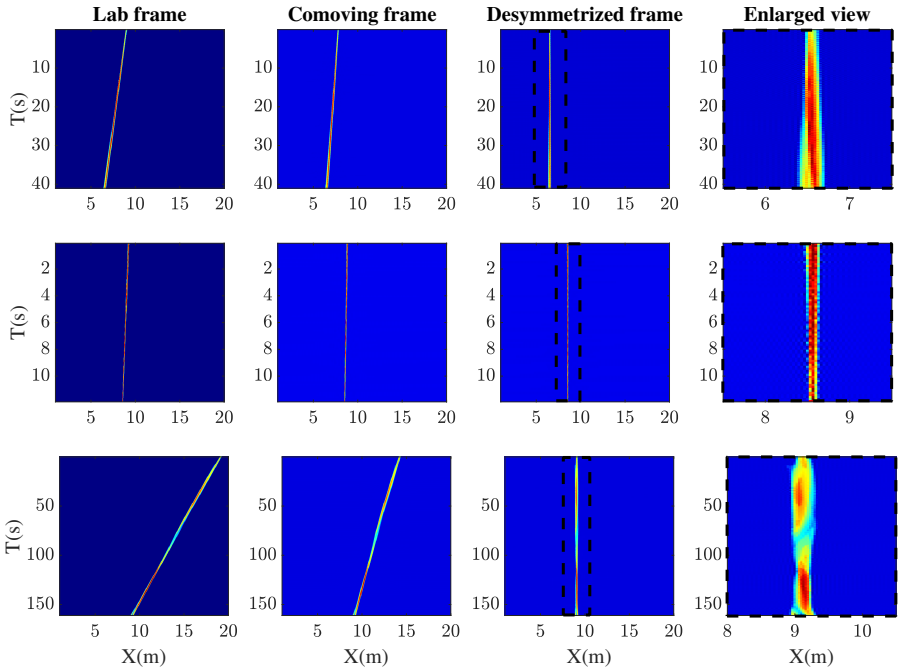


Figure 5.22: Space-time evolution of vortices in x-direction and time respectively in lab (left), comoving (center) and desymmetrized frame (right): Vortex1 (a), Vortex 2 (b) and Vortex 5 (c)

Summarizing all the results, we can assess that:

1. the differences between the dynamical and global velocities calculated on the single vortex and on the global flow field are mainly related to the different points of view. The global view, indeed, considers a flow

field partially filled by vortices. There are flow regions with only advective flow; the spatial average probably hides the single vortex behavior. Furthermore, the difference in the geometric velocity may be related to possible destructive interference of the vortices deformations;

2. the shape-changing dynamics of the vortices, induces a geometrical drift which is added to the dynamical drift induced by the flow advection.

The former might be related to a wave-like dispersive nature of the turbulence. This is what will be further investigated in Chapter §6

## 5.4 CONCLUSION

Large scales to small scale approach was applied to the study of turbulence of the channel flow, in order to reach an additional characterization. Symmetry reduction was applied first on the total spanwise vorticity $\omega_z(x, y, t)$. The Taylor hypothesis was verified to be not consistent with this range of turbulence where a component of the vorticity dynamics has due to the vortices shape-changing. A group of vortices were tracked and their dynamic were studied as a rigid body immersed in the flow. This allowed the application of the symmetry reduction also on the single vortex. The discovery was that as much as 50% of the vortex's velocity is caused by its deformation. It is not negligible and it is the novelty of this study.

# 6

## WAVE-LIKE DISPERSION OF TURBULENCE

The 'shape' changing dynamics of turbulence, besides the distorsion induced by the advection, might be related to a wave-like dispersive nature of turbulence like in water waves. In ocean waves, the geometric phases are induced by wave dispersion (Fedele, 2014). The objective of this chapter consists in assessing a possible correlation between turbulence and ocean wave; this is based on the insight that the turbulence evolution can hide a wave-like dispersion behaviour. To the purpose, it is helpful to introduce and quickly describe the formation process of the waves.

When the wind blows on an initially flat sea surface, it generates first capillary waves, i.e. short waves (from about few millimetres and until a couple of centimetres) whose propagation is dominated by the surface tension. Though small, under the action of the wind, capillary waves tends to be grouped and grow in size, both in wavelength and amplitude, originating gravity waves above a certain wavelength (typically larger than few centimetres), for which the gravity acceleration dominates their propagation. The different restoring mechanism (surface tension and gravity) determines their durability: capillary wave soon flattens as the wind stops blowing, while gravity wave, once formed by the wind, continues its propagation for long time even without any forcing wind. But more interesting is the different dispersion relationship, i.e. the dependence of the wave celerity from the frequency and wavelength, which characterizes the two different waves: for the capillary waves, it is proportional to $\sqrt{(}k)$, while for gravity waves in deep water it is $O(1/\sqrt{(}k))$.

This means that shorter wave components are faster than longer one for capillary waves while the opposite occurs for gravity waves. Since ocean waves typically travel by grouping, they exhibit a complex propagation which can become locally highly nonlinear during the focusing process (Fedele et al., 2019). In water waves theory, crest speeds are connected with their phase speeds. In deep water gravity waves the generic crests cyclically slowdown, focus and possibly break and then speed up. Because of the different dispersion behaviour, in capillary waves, crest first speeds up and then slows down. These phenomena are a direct consequence of the natural dispersion of waves and it is connected with their capacity to exchange energy while changing their shape (Fedele et al.,

2019). Wave nonlinearities may modify the slowdown and speed up process since they affect dispersion and the phase speed (Fedele, 2014). Our research question is first about the possible role of a wave-like dispersion behaviour in the Navier-Stokes flows and then the possible link between the wave-like dispersion nature and shape deformation of the vortices (Fedele and Dutykh, 2013a). In other words, we wondered if turbulence behaviour is analogous to that of ocean waves. We think that this is possible through a combined and comparative analysis of waves and turbulence dispersion, which is the core of the present chapter.

## 6.1 AN ANALYTIC SOLUTION OF WAVE PACKETS

We have mentioned that ocean waves propagate as wave groups. Then, the evolution of a wave packet with capillary and deep-water gravity waves dispersion relationship is here studied analytically.

The time-space evolution of a capillary wave is shown in figure 6.1. Here the

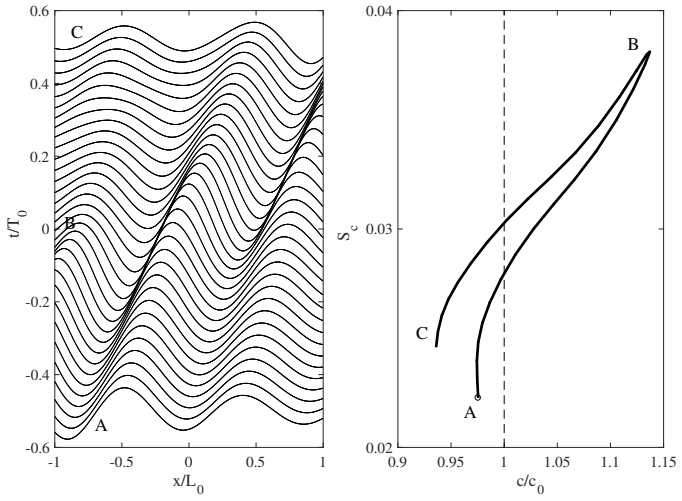


Figure 6.1: Capillary wave: Time-space evolution of wave elevation $\eta$ (left). Wave is moving from left to right. Hysteresis curve of the crest steepness $S_c$ as a function of phase velocity $c/c_0$ (right). Perfect focusing from (Fedele et al., 2019)

central crest of the group changes shape. In particular three essential phases are noticeable: a speedup phase (A) before focus, with the maximum crest speed attained at the focusing (B), followed by a slowdown (C) after a focus. The shape changing of the crest is the result of the shorter waves being before the longer waves before focus at (A), then they reach the longer waves at focus time in (B) and surpass them after focus (C).

In figure 6.2, the perfect focusing of a deep-water gravity wave was reported.

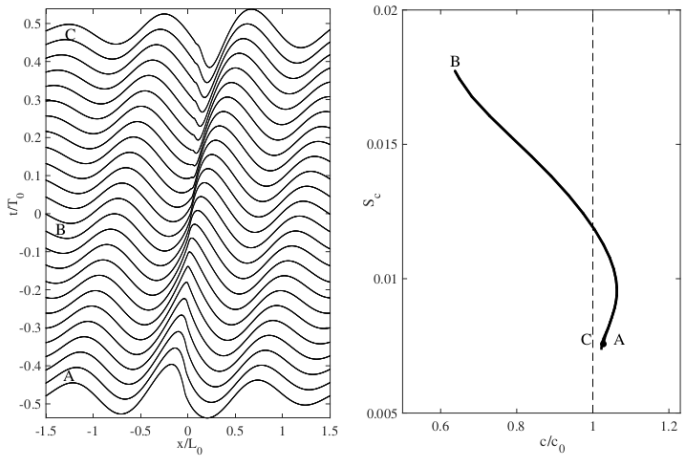


Figure 6.2: Deep water wave: Time-space evolution of wave elevation $\eta$ (left). Wave is moving from left to right. Hysteresis curve of the crest steepness $S_c$ as a function of phase velocity $c/c_0$ (right). Perfect focusing from (Fedele et al., 2019)

The three phases are: a slown down (A) before focus, with the minimum crest speed attained at the focusing (B), followed by a speed up (C).
The crest shape-changing here is the result of the longer waves being before the shorter waves before focus at (A), then they reach the shorter waves at focus in (B) and surpass them after focus (C).
Thus, the shape change of the crest is the manifestation of the dispersion of the wave group.
According to (Fedele, 2014), the crest slowdown phenomenon, which occurs when unsteadiness plays a role in the wave group propagation, has its theoretical origin in the geometric phase framework in quantum mechanics. The forward/backward leaning or asymmetry of the evolving crest of a focused wave is due to a linear phenomenon related to their dispersive nature. It can be explained in terms of geometric phases (Fedele et al., 2019). At focus point ($x = 0$) the profile becomes symmetric, the crest reaches its maximum height and the potential energy growth is zero. The focusing occurs at the point when the tallest wave in the group reaches its maximum possible crest height given by a superposition of elementary harmonic waves whose height depends on the packet amplitude spectrum. The crest speed of the largest wave in the group may be assumed to be the sum of a dynamical velocity (phase speed at the spectral peak) and a geometric component which depends on the shape changing of the crest (Fedele, 2014), that is

$$c_{crest} = c_{dynamic} + c_{geometric} \tag{6.1}$$

where the $c_{dynamic} = c_0 = \frac{w_0}{k_0}$, where $k_0$ is the wave-number of the spectral peak and $w_0$ is the associated frequency computed via the dispersion relation.

Let the wave elevation $\eta(x,t)$ with a dispersion law $\omega(k)$ and the Gaussian shaped spectrum $S(k)$ with variance $\sigma^2$ be:

$$\eta(x,t) = \int_{-\infty}^{\infty} S(k) e^{i(kx - w(k)t)} dk \tag{6.2}$$

where

$$S(k) = \frac{1}{\sqrt{2\pi\sigma^2}} e^{-\frac{1}{2}\frac{(k-k_0)^2}{\sigma^2}} \tag{6.3}$$

(Fedele et al., 2019) demonstrated that, for linear dispersion waves with $w(k) \sim k^n$ the crest speedup in capillary wave regime occurs for $n = 3/2 > 1$, while the slowdown in deep water gravity wave regime occurs for $n = 1/2 < 1$ . Analytical integration of the Gaussian integral yields the simplified form (see details in Appendix F)

$$\eta(x,t) = \frac{1}{\sqrt{2\pi\sigma^2}} \sqrt{\frac{\pi}{A}} e^{(\frac{B^2}{4A} + C)} \tag{6.4}$$

where

$$A = \frac{1}{(2\sigma^2)}(1 + 2i\sigma^2 w_0/k_0^2 t) \tag{6.5a}$$

$$B = 1/(2\sigma^2)(2k_0 + 2ix\sigma^2) \tag{6.5b}$$

$$C = -1/(2\sigma^2)k_0^2 \tag{6.5c}$$

By reversing the axes $\eta(-t,-x)$ gives packet for $k = w^2$ deep-water gravity waves. The largest wave crest of amplitude $h$ is observed at $x = 0$ and $t = 0$, according to quasi-deterministic theory (QD) (Boccotti, 2000). The QD theory shows that as $\sigma \longrightarrow \infty$, the largest crest belongs to a well-defined wave group that passes through $x = 0$ and reaches its maximum focus at time $t = 0$. The wave elevation of the group around the focusing point is described by (Fedele et al., 2020)

$$\eta_{QD}(x,t) = \Psi(x,t)h \tag{6.6}$$

where the largest wave crest of height h occurs at $x = 0$ and $t = 0$, and:

$$\Psi(x,t) = \int_0^{\infty} S_n(k)\cos(kx - wt)dk \tag{6.7}$$

is the space-time covariance of the surface elevation $\eta$, with $w$ the angular frequency. The crest speed c of the tallest crest of the stochastic wave group is:

$$c_{crest} = \frac{dx_c}{dt} \tag{6.8}$$

where $x_c(t)$ is the crest location at time t. From the condition that $\eta_x$ must vanish at $x = x_c(t)$ at any time t, that is

$$\eta_x = \eta_x(x = x_c(t), t) = 0 \tag{6.9}$$

it follows by expanding in Taylor series $\eta_x(x,t)$:

$$\eta_{xt} + \eta_{xx}\frac{dx_c}{dt} = 0 \tag{6.10}$$

from which

$$c_{crest} = -\frac{\eta_{xt}}{\eta_{xx}}, \tag{6.11}$$

As shown in figure 6.1, the ratio $c/c_0$ in the focusing point (B) is close to 1.15. This means that the geometric component is 15% and the shape changing is not negligible in the wave motion.

## 6.2 WAVE-LIKE DISPERSION OF TURBULENCE IN CHANNEL FLOWS

In order to find out the dispersion of turbulence, vorticity field of turbulent channel flow was analyzed at first globally and then through the tracking of the single vortices. The first analysis of the global field was evaluated through the Boccotti's quasi-determinism theory (Boccotti, 2008). As shown in the previous section, Boccotti's quasi-determinism theory predicts that the structure of a Gaussian field around an extreme or peak is shaped like the spacetime covariance function $\Psi(x,t)$, i.e. the anti-Fourier transform of the wave number frequency spectrum S(k,w). The most probable shape of a random field around a peak is given by the covariance function of the field. This result is not valid only for Gaussian processes as proven by Boccotti, but also for nonlinear fields and it can be proven via maximum entropy principle (new proof of this research). Given a random field as vorticity field, i.e. $\omega_z(X,t) = \eta(X,t)$, the spacetime dynamics nearby the large peak ($x = 0$, $t = 0$) $\eta_{max} = h$ is quasideterministic and given by the maximum entropy form:

$$\Psi(X,T) = <\eta(x,t)\eta(x+X,t+T)> \text{ covariance at } \eta \text{ (mean } \eta\text{=0)} \tag{6.12}$$

where

$$\Psi(X,T) = \int\int S(k,\omega)\cos(kx - wT)\,dk\,dw \tag{6.13}$$

$\Psi(X,T)$ is the anti-Fourier transform of the spectrum and $w$ is the angular frequency.

The particularity of QD theory, based on the study of the spacetime covariance, is that it is another way to reveal the dispersive nature of turbulence, but in physical space rather than in Fourier space, analysing the wave shape that leans backwards and forward as the packet slows down or speed up. The theory is also valid for non-Gaussian fields. The core of a turbulent field is quasi-Gaussian. The deviation from Gaussianity or intermittency is probably on the small scales. For further information, in figure 6.3 are shown the kurtosis and skewness evaluated for the streamwise velocity $U_x(x,y)$ and the

spanwise vorticity $\omega_z(x,y)$, averaged in z direction and in table 6.1 respectively the minimum, maximum and the average values. For a Gaussian field (weak turbulence) the value of skewness is aspected to be approximately equal to zero, while the kurtosis equal to 3. The mean values (table 6.1) would suggest the Gaussianity of the fields while they seem to be not everywhere Gaussian as shown in figures 6.3.

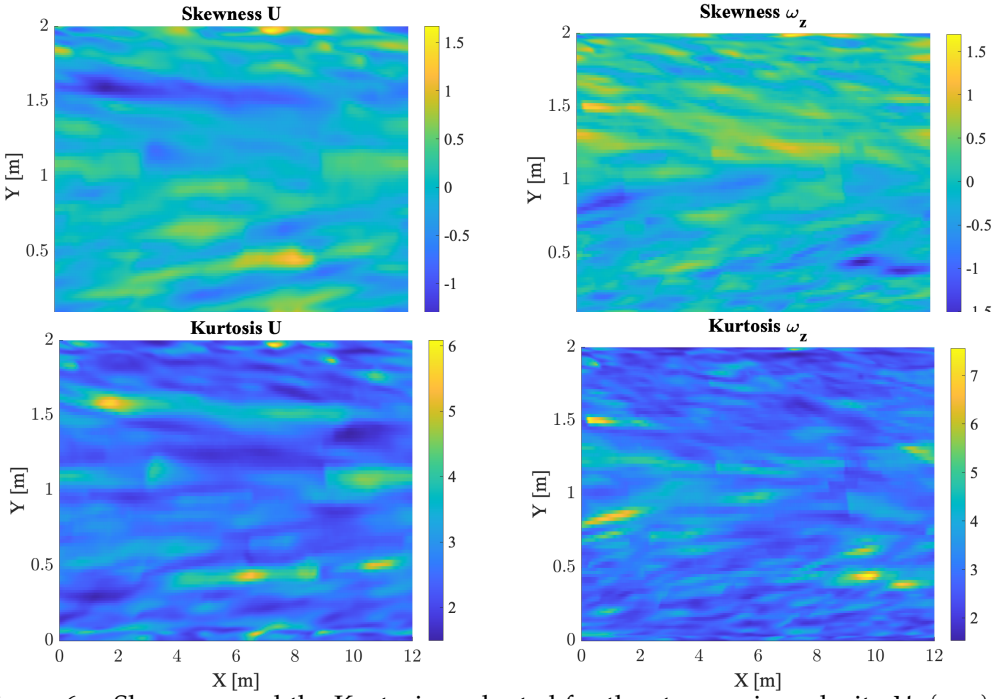


Figure 6.3: Skewness and the Kurtosis evaluated for the streamwise velocity $U_x(x,y)$ and the spanwise vorticity $\omega_z(x,y)$, averaged in z direction

| | Min | Max | Mean |
|---|---|---|---|
| Kurtosis U | 6.08 | 1.49 | 2.67 |
| Kurtosis $\omega_z$ | 7.56 | 1.54 | 2.98 |
| Skewness U | 1.67 | −1.44 | 0.0029 |
| Skewness $\omega_z$ | 1.69 | −1.67 | −0.023 |

Table 6.1: Kurtosis and skewness minimum, maximum and average value

### 6.2.1 *Dispersion feature of a Turbulent flow: from capillary to deep-water gravity waves*

***Full motion.*** The spanwise vorticity $\omega(x,y,t)$ (the same field used in the analysis of chapter 5), has been calculated on a prescribed section at a distance

$y = y_0$ from the wall, i.e. $\omega(x, y = y_0, t)$. In order to study the dispersion feature of the turbulence, through the Boccotti theory, the vorticity field $\omega$ will be considered alike the wave free-surface elevation $\eta(x, t)$. Then in the following we will use $\eta = \omega(x, y_0, t)$.The knowledge of the vorticity field along a prescribed wall normal section allows, according to the Boccotti's QD theory (see the previous subsection), the calculation of the covariance funtion $\Psi(x, t)$ for the spanwise vorticity. This enables the treatment of the vorticity as a QD wave packet: we then define it as a QD vorticity packet.
In order to preserve the dependency on the y direction, the covariance function has been estimated on two differents sections: one close to the wall and the second close to the centre of the channel.
Figure 6.4 shows the spanwise vorticity QD packet near the wall. The left plot shows the vorticity profiles along x for different time instants (y-axis). The right plot represents the velocity of the peak as a function of its amplitude. The evolution is symmetric with respect the focus time instant: the packet grows in amplitude reaching a peak and then the exact reversal phase occurs. The evolution resembles the one of the capillary wave packets: the packet speeds up $A- > B$ as it attains its maximum in B and then slowdown symmetrically $B- > C$. At the focusing there is a constructive interference of many elementary "waves": small scale structures behind large scales travel faster reaching them and generating a large peak.

In figure 6.5 the spanwise vorticity QD packet near the center is shown. It is interesting to observe as the trend is the opposite to the previous one, i.e. the QD vorticity packet near the center behaves as a deep-water gravity wave: it slightly slowdown as it peaks up. The speed up occurs, causing the decrease of the peak

This study seems to suggest that, as the distance from the wall increases, vorticity scales change their geometry and their dispersion features.
Figure 6.6 gives the hysteresis curves of the peak of velocity vs peak amplitude of the QD group of vorticity $\omega_z(x, t)$. Moving from wall (left) to centre (right), the speed up followed by the slow down behaviour, typical of the small turbulent scale (capillary waves) becomes slow down followed by the speed up typical of the large turbulent ones (deep-water gravity waves). The red dashed line, corresponding to the 3% of the channel half width marks the reversal of behaviour from capillary to deep water waves. It means that in the boundary layer, initially dominated by small scales, the large scales become even more significant.
***Desymmetrized motion***. To further confirm our insight the QD theory was also applied to the desymmetrized field.
Figures 6.7 and 6.8 depict, respectively, the pure speed-up/slow-down typical of the capillary-like behavior and the pure slow-down/speed-up typical of the deep water gravity wave-like behavior. Here, the desymmetrization has been done using the 14th Fourier slice. Because of that, the dynamical velocity

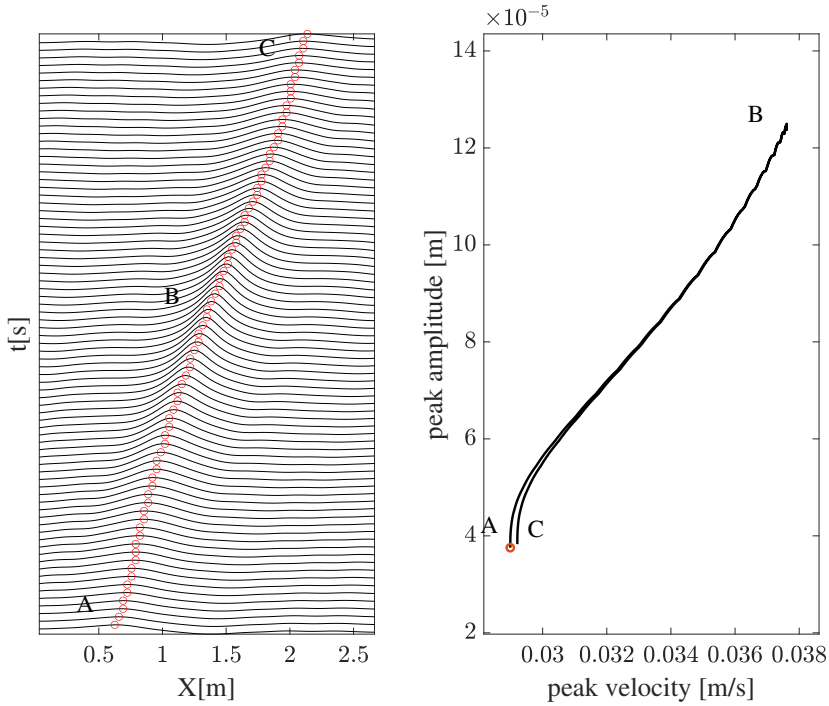


Figure 6.4: Spanwise vorticity QD packet near the wall. Packets behave as capillary wave groups. Vorticity profiles (left), Hysteresis curves of the peak velocity vs peak amplitude (right)

component has been removed and the turbulence dynamics is then governed by the pure deformation. Velocity module in figure 6.7 increases from A to B until the focusing (speed up) and decreases after from B to C (slowdown) according with the capillary behaviour in the wall region. In contrast, near the centre of the channel velocity decreases from A to B (slowdown) and increases from B to C (speed up) as a deep water gravity wave propagation.

***Phase velocity***. Assuming the general phase speed as $C(k) = \omega(k)/k$, the streamwise phase velocity U(k) for the QD packet is:

$$U(k) = \frac{\int S(k,\omega)\frac{\omega}{k}d\omega}{\int S(k,\omega)d\omega} \tag{6.14}$$

The assessment of the wave-like dispersion of turbulent scales is given in figure 6.9. Moving from wall to center of the channel, the phase speed changes from a hyper capillary regime for really small scales (i.e. large k) $(w \sim k^4)$ to water gravity wave regime $(w \sim \sqrt{(k)})$ for the larger scales (i.e. small k).

Figure 6.10 shows the phase velocity computed on the desymmetrized field, confirming the above observed behavior for small and large turbulence scales.

In this way we assessed that the analysis of the QD covariance of spanwise vorticity shows a strong analogy with the propagation of a capillary and a

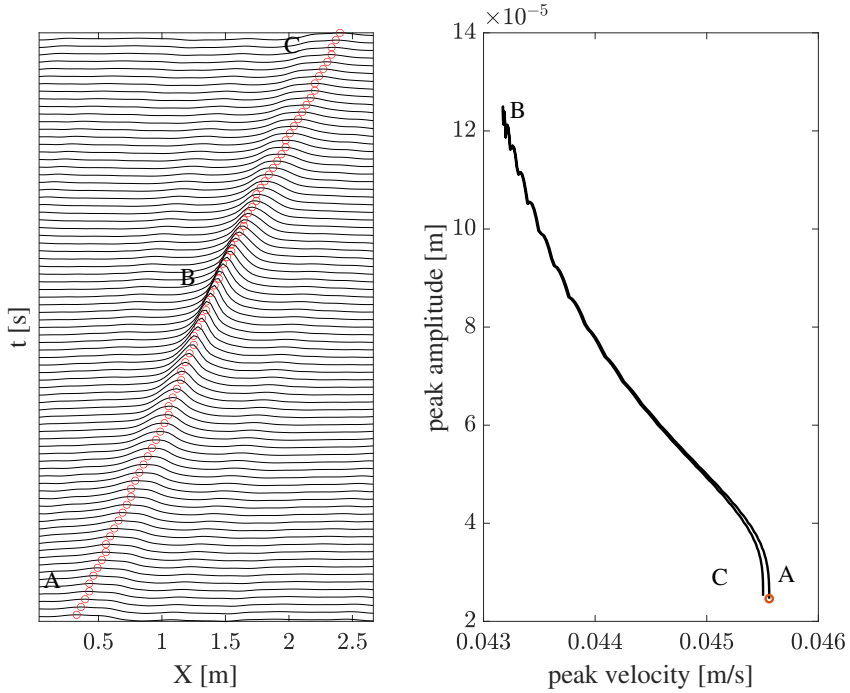


Figure 6.5: Spanwise vorticity QD packet near the center. Packets behave as deep water wave groups. Vorticity profiles (left), Hysteresis curves of the peak velocity vs peak amplitude (right)

deep water gravity wave packet, respectively, for the small turbulent scales characterizing the flow at the wall and the large scale of the flow at the center of the channel.

### 6.2.2 *Conclusions*

In this chapter, we demonstrate the wave-like feature of turbulence structures. In particular, we analyzed the 2D vorticity field $\omega(x, y, t)$ in order to discover that the deformation of vortices is strictly connected with the wave-like dispersion of turbulence. The evolution of a wave packet with capillary and deep-water gravity waves dispersion relationship were studied analytically in order to understand the different dispersive behaviors. Furthermore, the application of QD theory was a perfect way to reveal the dispersive nature of waves and later of turbulence. We discovered that moving from wall to center of the channel, the turbulence structures change from a hyper-capillary regime for really small scales ($w \sim k^4$) to water gravity wave regime ($w \sim \mathrm{sqrt}(k)$) for the larger scales. The QD theory was applied both to the original vorticity field and to the desymmetrized one. It highlighted even more, the shape-changing

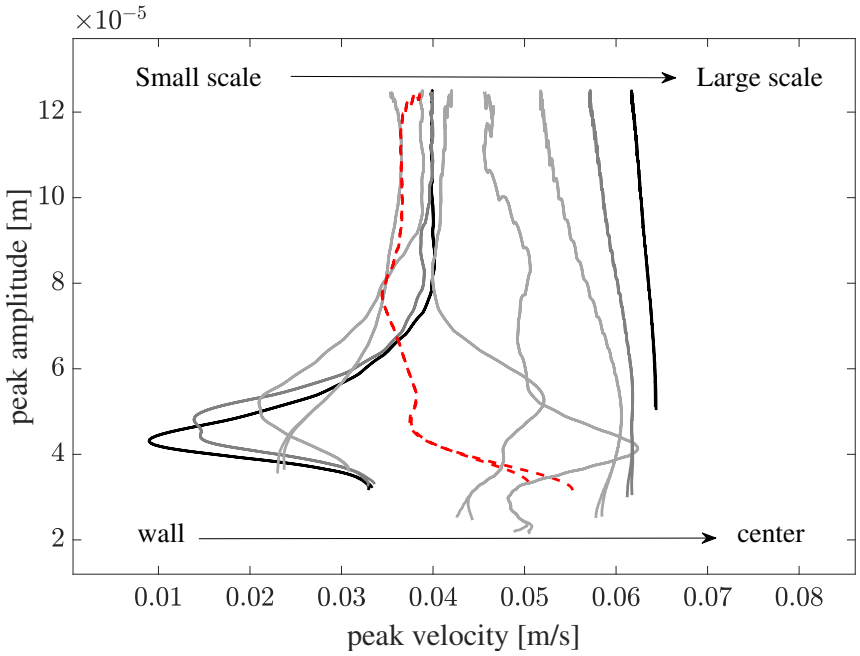


Figure 6.6: Hysteresys curves of the peak velocity vs peak amplitude of the QD group as a function to the distance from the wall

of vortices.
This new wave-like feature of the turbulence suggested us to represent the three tracked vortices as a free surface wave group evolving in time and space as the time-stack in figure 6.11, respectively Vortex 1 (top), Vortex 2 (center) and Vortex 5 (bottom) in Lab frame (left), comoving frame (center) and deymmetrized frame (right).
In particular, in the first two windows, vortices are watched from the earth-lab frame respectively at $x = X_{max} = cost$ and $y = Y_{max} = cost$. In $x = X_{max}$ we observe that vortices are moving in wall normal direction towards the center of the channel without any drift and changing their shape (section-shape). This is because vortices motion along the wall-normal direction, although bounded between $0.66m$ and $0.88m$, shows a weak trend to approach the center of the channel but without any symmetry, i.e. advection velocity. In $y = Y_{max}$ the vortices dynamics was prevailed by the drift given by the T-symmetry. According to Chapter §5, the vortices dynamics was observed by the comoving frame and then by the desymmetrized frame. While in the comoving frame there is still a drift given by the motion produced by the shape-changing of vortices, in the desymmetryzed frame the pure deformation is revealed. Looking at figure 6.11, Vortex 5 (bottom), one can realizes how much this representation is helpful to highlight the differences between the system of references and even more the

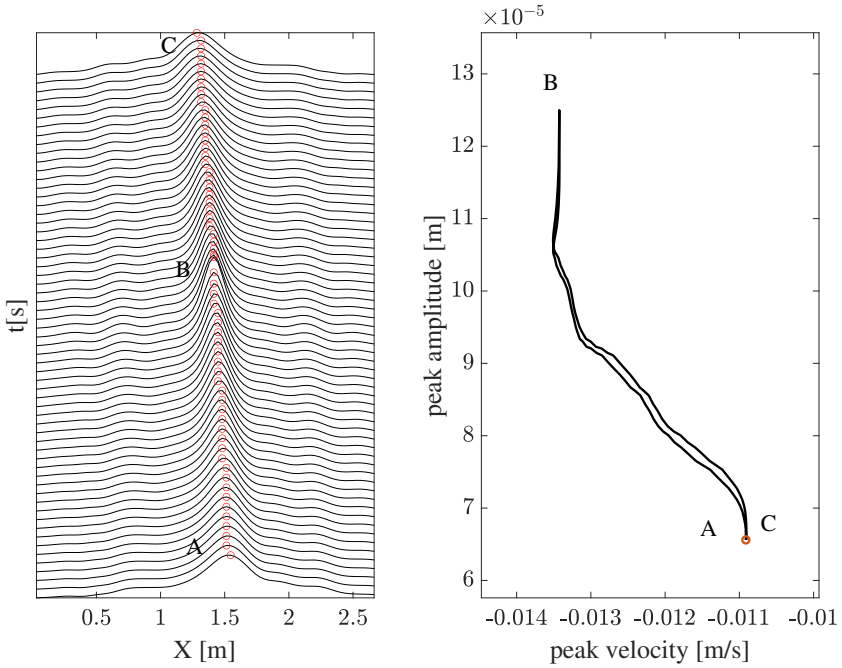


Figure 6.7: Desymmetrized spanwise vorticity QD packet near the wall.Pure speed up of small scaled as capillary wave groups. Vorticity profiles (left), Hysteresys curves of the peak velocity vs peak amplitude (right)

shape-changing in the desymmetrized frame. In the latter, indeed, we observe in the time evolution the shrinking and widening of the vortex section

In order to further assess the wave-like dispersive behavior of vortices, we applied the QD theory, as the first time, to the vortex 5. Unlike the previous application on the total field that was at y = cost, in the vortex case, the QD was applied to a 3D field $\omega_{vort}(x, y, t)$, respectively, to the full motion (see figure 6.12) and the to desymmetryzed motion (see figure 6.13).

As predicted by the QD theory, we observe the shape of the maximum of vorticity at the focusing point that occurred in $x = 0$ and $t = 0$. In the original field, the vortex travels in the channel and focused as shown in the time frames in figure 6.12 and in this video. In the desymmetrized field, the vortex changes its shape remaining fixed in a point as shown in figure 6.13 and in the video, thus showing its pure deformation. If a vortex is thought of as a superposition of harmonics waves, focusing occurs at the point when the tallest wave of the group reaches its maximum possible crest height, as observed in the wave packets.

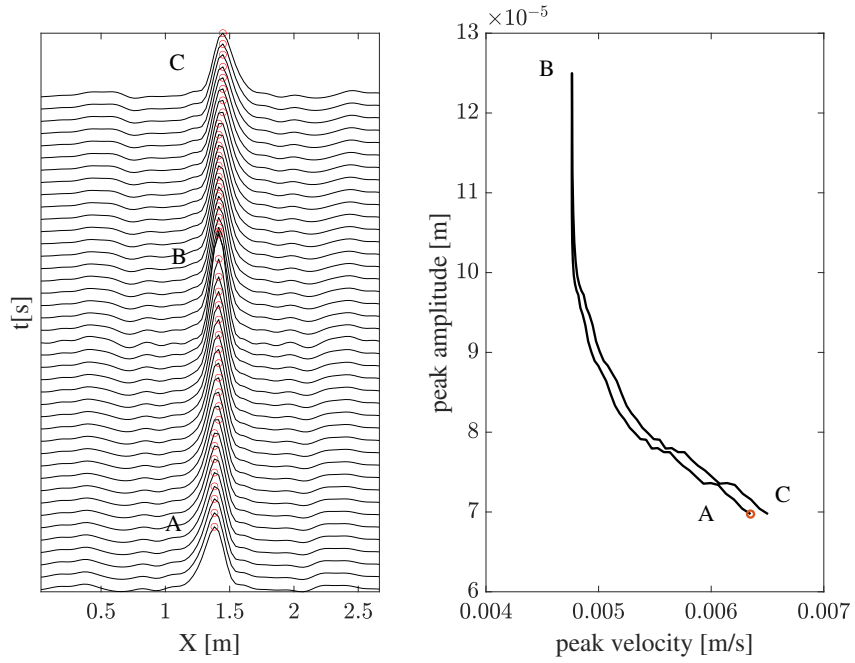


Figure 6.8: Desymmetrized spanwise vorticity QD packet near the center. Pure slow down of large scaled as deep water wave groups. Vorticity profiles (left), Hysteresys curves of the peak velocity vs peak amplitude (right)

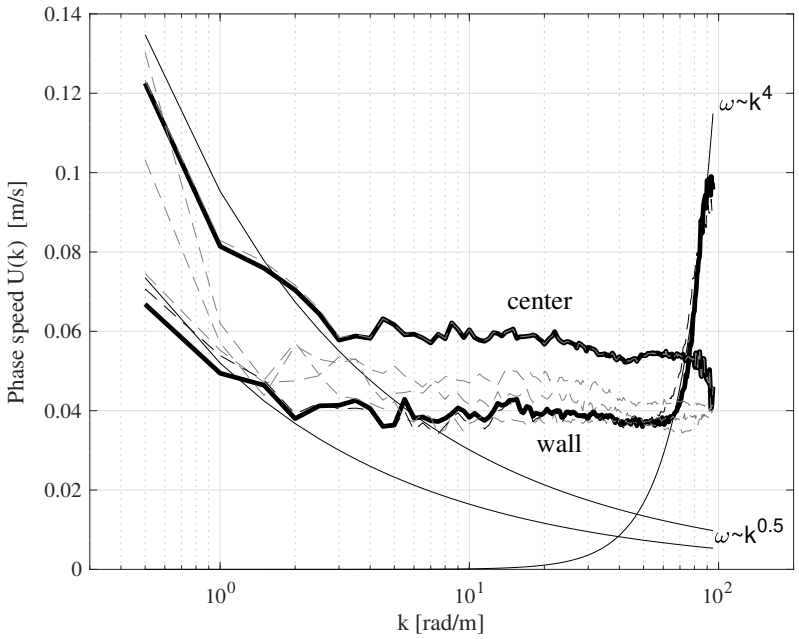


Figure 6.9: Phase speed $U(k)$ of the spanwise vorticity. Trends of wall and center of the channel compared with capillary and deep water waves regimes

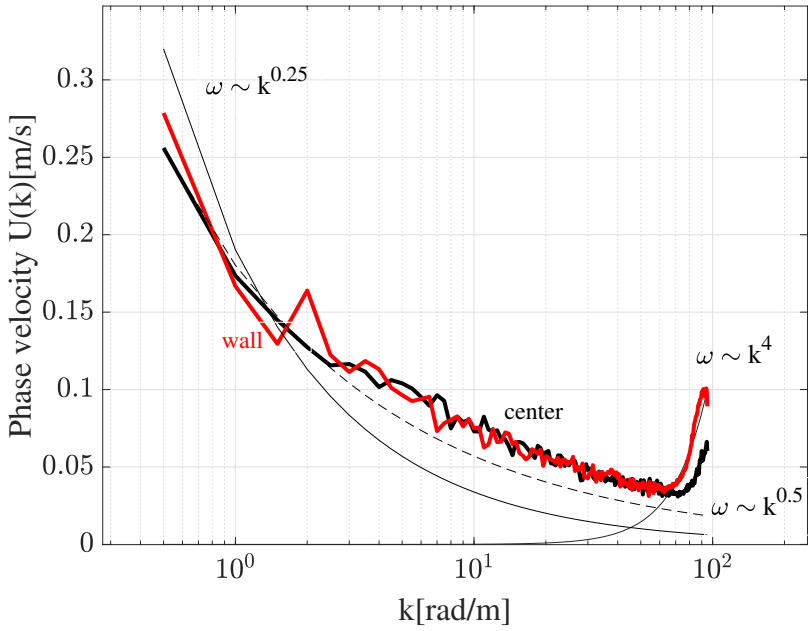


Figure 6.10: Phase velocity of the desymmetryzed field $\omega_z$ with 14th Fourier slice. Wall (red bold line) and center (black bold line) compared with capillary and deep water regimes

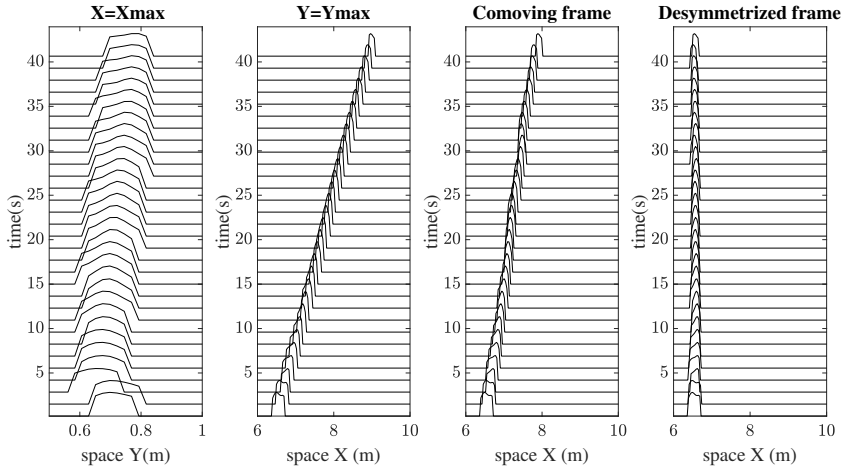


(a) Vortex 1

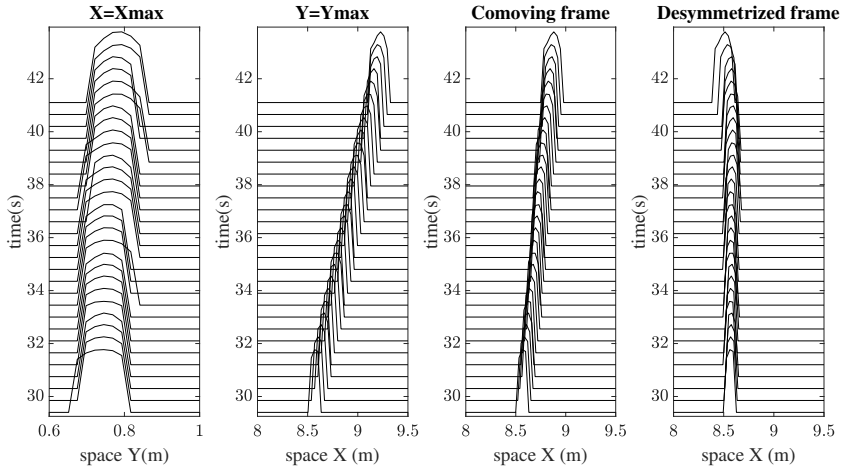


(b) Vortex 2

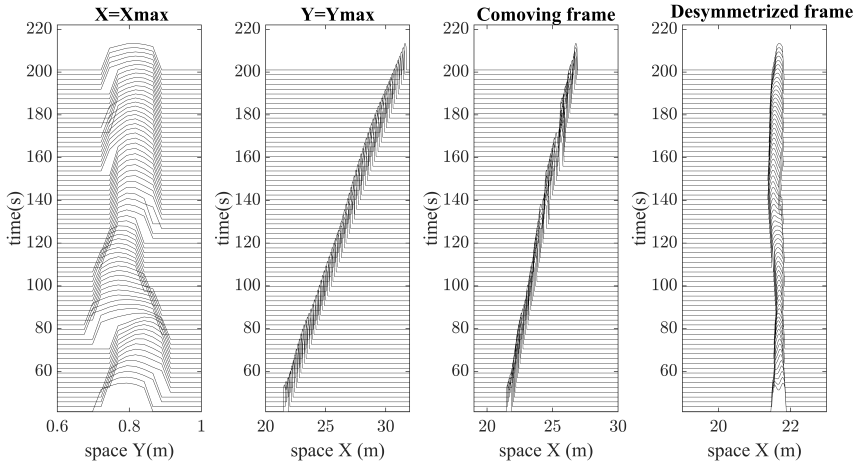


(c) Vortex 5

Figure 6.11: Time stack of vortices in the three reference system: Lab frame, Comoving frame and desymmetrized frame. Vortex 1(up), Vortex 2(center), Vortex 5(bottom)

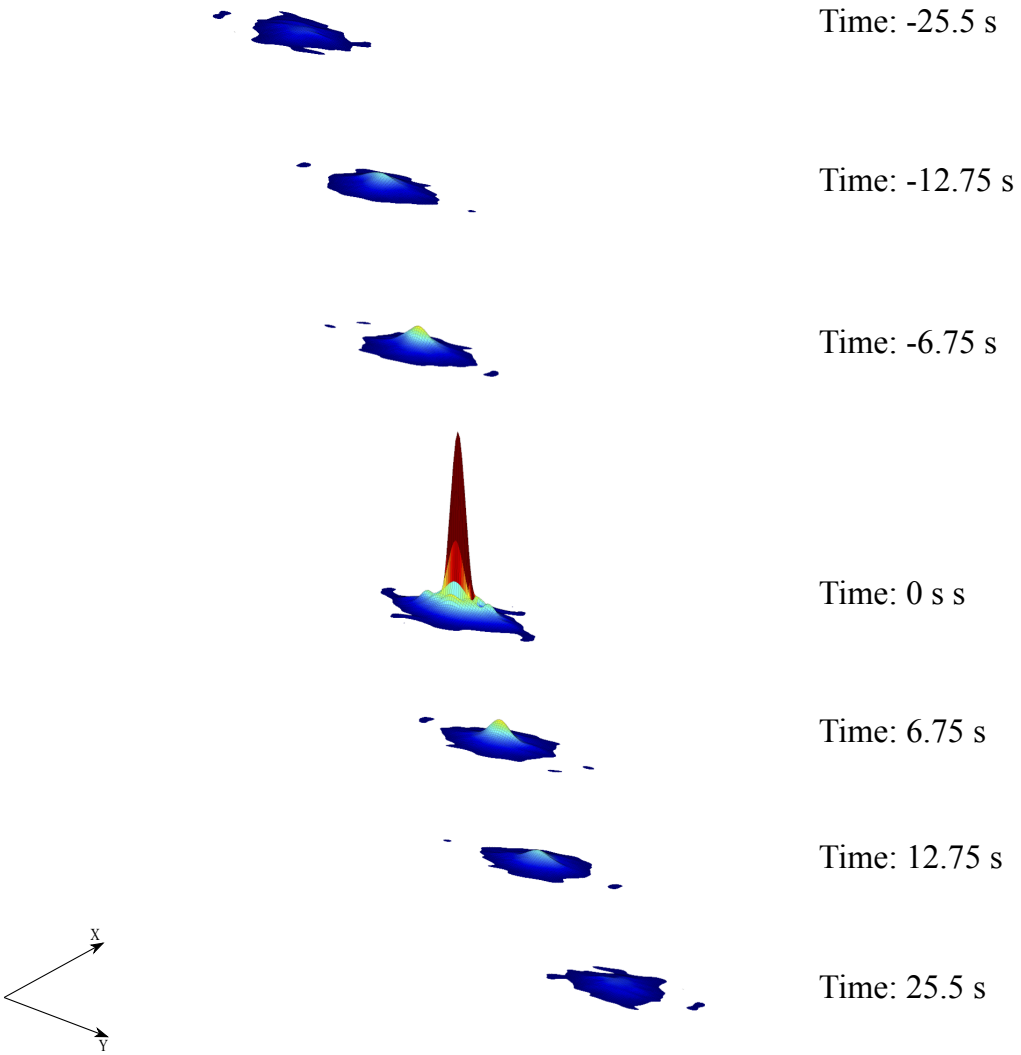


Figure 6.12: Time frames of QD theory applied to the vortex 5. It travels in the channel and focus at $x = 0$ and $t = 0$

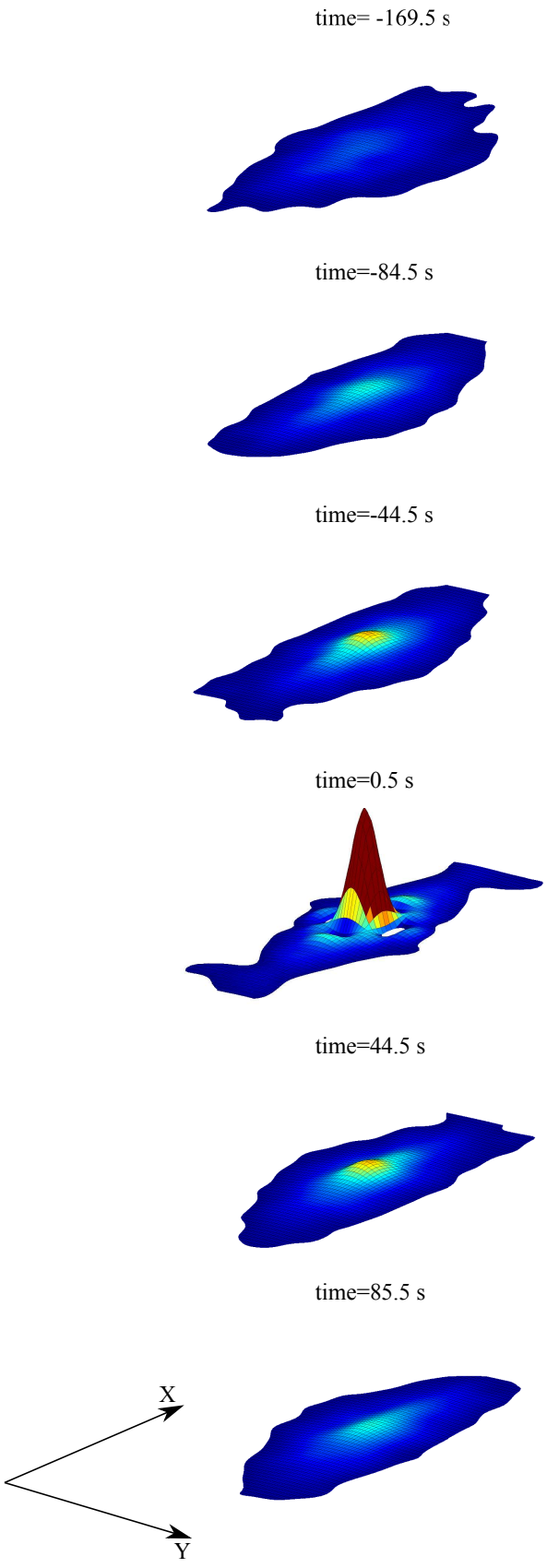


Figure 6.13: Time frames of QD theory applied to the desymmetrized Vortex 5. It is fixed in the channel and focuses at $x = 0$ and $t = 0$

# 7

# CONCLUSION AND FUTURE PERSPECTIVES

In the present resaerch activity, the turbulence of channel flow was studied for finding an additional and novel interpretation of the turbulent flow.
The results of the numerical simulated turbulent channel flows at $Re_\tau = 180$ were described and compared with the literature data (Chapter §2). These were suitable for implementing the subsequent study phase based on the use of symmetry reduction and vortex tracking.
In order to introduce the symmetry-reduction method and its concepts, simpler systems of discrete planar vortices were employed, exploiting the Hamiltonian theory (Chapter§3).
These allowed the later understanding thoroughly the more general symmetry reduction methods approaching them more in detail from the geometric and mathematics point of view (Chapter §4).
The symmetry-reduction was applied to the turbulent channel data: the translational symmetry was removed from the global field of vorticity, demonstrating that the Taylor's hypothesis is not consistent with this range of turbulence where a component of the vorticity velocity is due to the vortices shape-changing. Later, a group of vortices was tracked to go deeply inside the physics of turbulence. This allowed to apply the symmetry reduction also to the isolated vortices and reveal the shape of turbulence. This two analysis, global and local, showed some differences in the dynamical and geometric phase velocity. The explanation is that in the global view the flow field is considered as partially filled by vortices and with some flow regions with the only advective flow; the spatial average probably hides the single vortex behaviour. Furthermore, the difference in the geometric velocity may be related to possible destructive interference of the vortices deformations. On the contrary, in the single-tracked vortices, the contribution of vortex deformation is more explicit and fully assessed, after the removing of the symmetry (Chapter §5).
Last, but not least, the demonstration that the vortex shape-changing dynamics is the proof of the physical manifestation of an hidden wave-like dispersion behaviour of the turbulence. A capillary wave group and deep water gravity wave were studied to understand the different dispersive behaviours and associate it to the vortices through the application of the quasi-deterministic theory:

boundary layer vortices (small scales) behave as capillary waves while central vortices (large scales) as deep-water gravity waves (Chapter §6)

Summarizing, the novelties and understandings of this work were:

- symmetry reduction approach provides a new way to study the anatomy of the vortical motion. This depends on the inertia of the flow and on its own shape-changing form in time;
- because of the inertia of the flow, vortices are transported at the Taylor speed, the so-called dynamical velocity Fedele et al. (2015);
- the shape-changing in time induces a "self propulsion velocity", the so-called geometric velocity Fedele et al. (2015);
- in strong turbulence, the Taylor's hypothesis of frozen vortices is not satisfied since the geometric velocity is not negligible;
- the global view hides almost totally the geometrical velocity of vortices probably caused by the destructive interference of vortices deformation and by the not completely flow filled by vortices;
- on the contrary, single tracked vortices showed a geometrical velocity that is the half of the total one;
- in the Kolmogorov's inertial range, the geometric velocity is induced by the vortex shape-changing dynamics, which is the physical manifestation of an hidden wave-like dispersion property of turbulence (Fedele, 2014).
- The Boccotti's quasi-deterministic method (Boccotti, 2008) was applied to vorticity field evaluated as a wave group in order to further demonstrate the wave-like dispersion of turbulence. In particular, the small scales structures behaves as capillary waves while large scale as deep water gravity waves.

This new method of characterization of turbulence and a new methodology promises to be capable of being applied to a variety of fluid dynamics problems in which turbulence is present.
From the results and simulations experience, OpenFOAM is not the best performing code for doing DNS analysis. Computational efforts and cost were higher than other codes. Spectral codes for doing DNS simulations on simple geometries such as the turbulent channel are probably much more efficient. This research was born within a much larger project that aims to study rogue waves (an open problem (Fedele et al., 2016), (Fedele et al., 2017) and understand if the turbulence caused by the wind wave interaction is a factor that influences the arising of these huge and unexpected waves. In order to perform

DNS simulations for studing the wind wave boundary layer, it was necessary to be sure of having an accurate solver working with geometries that change over time and space.
In the future, to move forward in the characterization of turbulence at higher Re, it will be useful try other codes (Nek500, Channel flow 2.0).
Furthermore, numerical simulations alone are not sufficient, so experimental campaigns on the turbulent channel are planned to compare numerical results and reach higher turbulence regimes based on the works of (Antonia et al., 1997), (Cenedese et al., 1998), (Antonia et al., 1998), (Romano et al., 1999), and (Romano, 1995).
Moreover, a more detailed analysis of the vortex merging and instabilities on system of vortices in 2D and 3D based on the works of (Meunier et al., 2005), (Kraichnan, 1967), (Siggia and Aref, 1981), (Leweke et al., 2016). Regarding the characterization of vortices, it will certainly be useful to find other quantities for a better localization and detection of the vortex in time and space. In particular, it will be interesting to track vortices on the 3D field, to discover the evolution of their natural shape and the real-direct energy cascade.

# A

## APPENDIX A: HAMILTONIAN THEORY

The spring-mass system is shown in figure A.1 A mass m is subjected by a

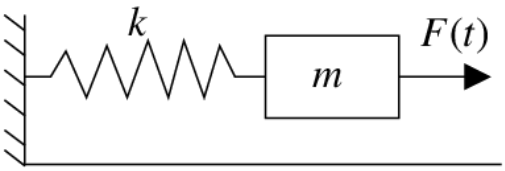


Figure A.1: Mass-spring system

force $F(t)$ and displays a displacement of $q(t)$ and k is the spring constant. The second Newton law gives the

$$m\ddot{q} + kq = f(t). \tag{A.1}$$

The total energy is an invariant of the motion since :

$$E = K + P = const \tag{A.2}$$

is conserved and that is $\frac{dE}{dt} = 0$, where the kinetic energy is:

$$K = \frac{1}{2}m\dot{q}^2 \tag{A.3}$$

and potential energy is:

$$P = \frac{1}{2}kq^2 - fq \tag{A.4}$$

The Lagrangian of the system is given by:

$$\mathcal{L} = K - P = \frac{1}{2}m\dot{q} - \frac{1}{2}kq^2 + fq. \tag{A.5}$$

the dynamics in the time interval T minimizes the action

$$A(q, \dot{q}, t) = \int_0^T \mathcal{L}(q, \dot{q}, t)dt \tag{A.6}$$

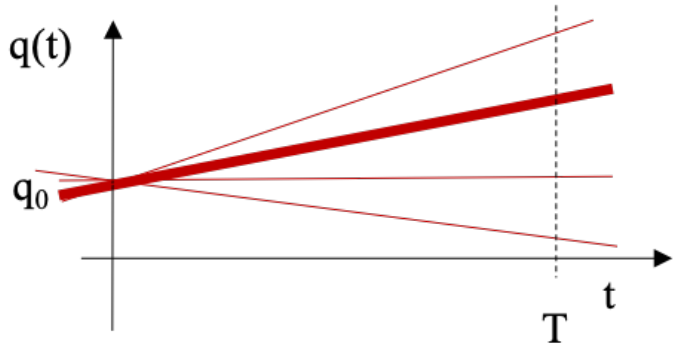


Figure A.2: Admissible trajectories

Figure A.2 depicts several admissible trajectories of the system. However there is only one that minimizes the action (Bold line).

So the variational derivative

$$\frac{\delta A}{\delta t} = 0 \tag{A.7}$$

yields equation A.1.

*DEMONSTRATION*

Since

$$A = \int_0^T [K - P] dt, \tag{A.8}$$

$$\frac{\delta A}{\delta q} = \frac{\partial \mathcal{L}}{\partial q} - \frac{d}{dt}\left[\frac{\partial \mathcal{L}}{\partial \dot{q}}\right] = -\frac{\partial P}{\partial q} - \frac{d}{dt}\left[\frac{\partial K}{\partial \dot{q}}\right] = -[kq - f] - \frac{d}{dt}[m\dot{q}] = 0 \tag{A.9}$$

So equation A.1 is obtained. This is a second order ODE. The equation A.1 can be reduced to a first order ODE. To do so, the Hamiltonian is written in terms of the conjugate variables [p.q], where the momentum is $p = m\dot{q}$

$$m\ddot{q} = \frac{d}{dt}(m\dot{q}) = \frac{dp}{dt} \tag{A.10}$$

So the first order system is obtained:

$$\begin{cases} \frac{dp}{dt} &= -kq + f \\ \frac{dq}{dt} &= \frac{p}{m} \end{cases} \tag{A.11}$$

together with the "sympletic structure" of the Hamiltonian equation:

$$\begin{cases} \frac{dp}{dt} &= -\frac{\partial H}{\partial q} \\ \frac{dq}{dt} &= \frac{\partial H}{\partial p} \end{cases} \tag{A.12}$$

Writing the kinetic and potential energy as a function of conjugate variables $(p, q)$

$$\begin{cases} K &= \frac{1}{2}m\dot{q}^2 = \frac{p^2}{2m} \\ P &= \frac{1}{2}kq^2 - fq \end{cases} \tag{A.13}$$

The Hamiltonian :

$$H(q,p) = K + P = \frac{p^2}{2m} + \frac{1}{2}kq^2 - fq \tag{A.14}$$

For the mass-spring system, H is the total energy but this is not true for a general system. If $F(p, q, t)$ is a generic observable, then the rate of change of F under the dynamics is:

$$\frac{dF}{dt} = \frac{\partial F}{\partial t} + \frac{\partial F}{\partial q}\frac{dq}{dt} + \frac{\partial F}{\partial p}\frac{dp}{dt}. \tag{A.15}$$

The Hamiltonian description defines a "hydrodynamic and incompressible

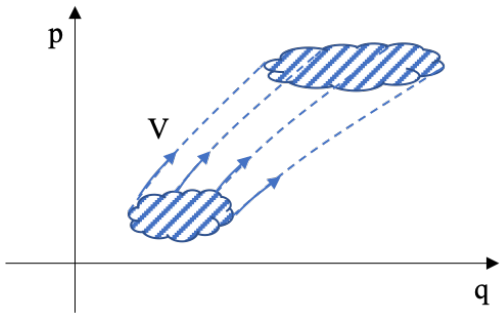


Figure A.3: Manifold

flow" $\mathbf{V}$ ($\nabla \cdot \mathbf{V} = 0$) on the manifold $M = \mathbf{R}^2$ (see figure A.3), given by:

$$\mathbf{V} = [u, v] = \left[\frac{\partial q}{\partial t}, \frac{\partial p}{\partial t}\right] = \left(\frac{\partial H}{\partial p}, -\frac{\partial H}{\partial q}\right) \tag{A.16}$$

At any point of $\mathbf{R}^2$ there is a velocity vector field $\mathbf{V}$ and the flow is defined as the tangent to $\mathbf{V}$. The velocity field is "incompressible",this means that starting with a initial volume of flow it remains the same as the flow evolves but it can change shape. In fact $\nabla \cdot \mathbf{V} = 0$ ,or

$$\frac{\partial u}{\partial q} + \frac{\partial v}{\partial p} = \frac{\partial}{\partial q}\left[\frac{\partial H}{\partial p}\right] + \frac{\partial}{\partial p}\left[\frac{\partial H}{\partial q}\right] = 0 \tag{A.17}$$

Hamiltonian equation generates a sort of hydrodynamic flow in the variable the conjugate variable (q,p) and the flow evolution is a such a way to keep the

flow incompressible so the area and the patches of the area evolve under the flow keeping the area constant

$$\omega = dq \wedge dp \tag{A.18}$$

An example of Hamiltonian system in fluid mechanics is as follow. Consider an incompressible flow $\vec{v}$, the stream functions $\Psi$ can be written as:

$$\vec{v} = \left[\frac{\partial \Psi}{\partial y}, -\frac{\partial \Psi}{\partial x}\right] \tag{A.19}$$

and

$$\nabla \cdot \vec{v} = \frac{\partial}{\partial x}\left[\frac{\partial \Psi}{\partial y}\right] + \frac{\partial}{\partial y}\left[-\frac{\partial \Psi}{\partial x}\right] = 0 \tag{A.20}$$

is always satisfied. Since

$$\vec{v} = \left(\frac{\partial x}{\partial t}, \frac{\partial y}{\partial t}\right) = \left[\frac{\partial \Psi}{\partial y}, -\frac{\partial \Psi}{\partial x}\right] \tag{A.21}$$

then

$$\left(\frac{\partial x}{\partial t}, \frac{\partial y}{\partial t}\right) = \left[\frac{\partial \Psi}{\partial y}, -\frac{\partial \Psi}{\partial x}\right] \tag{A.22}$$

that is similar to the equation A.16 in which the Hamiltonian $H$ coincides with the stream function $\Psi$.

The evolution of the observable F is:

$$\frac{dF}{dt} = \frac{\partial F}{\partial t} + \frac{\partial F}{\partial x}\frac{\partial x}{\partial t} + \frac{\partial F}{\partial y}\frac{\partial y}{\partial t} = \frac{\partial F}{\partial t} + \frac{\partial F}{\partial x}\frac{\partial \Psi}{\partial x} - \frac{\partial F}{\partial y}\frac{\partial \Psi}{\partial y} \tag{A.23}$$

$$\frac{dF}{dt} = \frac{\partial F}{\partial t} + [F, \Psi] \tag{A.24}$$

where $[F, \Psi]$ are the Poisson Brackets. In this case the Hamiltonian doesn't represent the kinetic energy or the total energy of the system as seen above. It is simply related to the stream function $\Psi$ of the flow evolution it's in such a way that it evolves and the stream functions remains constant $\Psi[x, y] = cost$.

# B

## APPENDIX B: PROPER ORTHOGONAL DECOMPOSITION-POD

Suppose to have a set of data $x(t) \in \mathbf{R}^n$, in the interval $0 < t < T$, and to seek a projection $P_r$ that minimize the total error (Rowley (2005)):

$$\int_0^T |x(t) - P_r x(t)|^2 \, dt \tag{B.1}$$

To solve this problem, a matrix $nxn$ is introduced that is:

$$R = \int_0^T x(t)x(t)^* dt \tag{B.2}$$

: where $x_r^*(t)$ denotes the transpose, and find the eigenvalues and eigenvectors of R given by:

$$R\phi_k = \lambda_k \phi_k \tag{B.3}$$

with $\lambda_k$ the eigenvalues and $\phi_k$ the eigenvectors chosen to be orthonormal. The results of the POD is that the optimal subspace of dimension r is spanned by $\phi_1 ... \phi_r$ and the optimal projection $P_r$ is given by

$$P_r = \sum_{k=1}^{r} \phi_k \phi_k^* \tag{B.4}$$

where $\phi_r$ are called POD modes. To compute the POD modes with the method of snapshot, one must solve a $nxn$ eigenvalue problem and the integral B.3 becomes:

$$R = \sum_{j=1}^{m} x_r(t) x_r^*(t) \delta_j \tag{B.5}$$

with $\delta_j$ the quadrature coefficients. Assembling data into a $nxm$ matrix

$$X = [x(t_1)\sqrt{\delta_1} ... x(t_j)\sqrt{\delta_j}] \tag{B.6}$$

and the sum B.5 is written $XX^*$. The eigenvalue problem becomes:

$$X^* X u_k = \lambda_k u_k \qquad u_k \in \mathbf{R}^m \tag{B.7}$$

The eigenvectors $u_k$ may be chosen to be orthonormal and the POD modes are then given by $\phi_k = Xu_k/\sqrt{\lambda_k}$. In matrix form, with $\Phi = [\phi_1 ... \phi_m]$ and $U = [u_1 ... u_m]$ this becomes:

$$\Phi = XU\Lambda^{-1/2} \tag{B.8}$$

# C

## APPENDIX C: FOURIER FFT IN THE SPACE

Given a solution $u(z, y, t)$ that is a snapshot of a dynamical field defined in $\mathbf{R}^N$. The Fourier transform in the space is:

$$\sum_{-N/2}^{N/2} a_{n,m} e^{i(k_x n x + k_y m y)} \tag{C.1}$$

The coefficients $a_{n,m}$ are called Fourier amplitudes and they are defined in a matrix of dimension $[N+1, N+1]$

$$\{a(t)_{n,m}\}_{n,m=-N/2;N/2} = \begin{bmatrix} a_{0,1} & a_{0,1} & \dots & a_{0,N} \\ \dots & & & \\ \dots & & & \\ \dots & & & \\ \dots & & & \\ a_{N,0} & a_{N,1} & \dots & a_{N,N} \end{bmatrix} \tag{C.2}$$

In MATLAB for a specific time instant $t = t^*$

$$z = reshape(A, (2N+2, 1)) = \begin{Bmatrix} a_{11} \\ a_{12} \\ \dots \\ \dots \\ a_{1,N} \\ \dots \\ \dots \\ a_{NN} \end{Bmatrix} = \begin{Bmatrix} z_1 \\ z_2 \\ \dots \\ \dots \\ a_N \\ \dots \\ \dots \\ a_{2N+2} \end{Bmatrix} \tag{C.3}$$

### FOURIER SERIES

In the space $\mathbf{R}$ , a bases of vectors linearly independent is:

$$v_j = v_1, v_2, \dots, v_n \tag{C.4}$$

but not orthonormal and a generic field solution $u \in \mathbf{R}$ is defined as:

$$u = \sum_{j=0}^{N} u_j \cdot v_j = u_1 \cdot v_1 + u_2 \cdot v_2 + \cdots + u_N \cdot v_N \tag{C.5}$$

The angle between vectors is found by scalar product:

$$u_j \cdot v_j = < \vec{u}, \vec{v} > = \left\| \vec{u} \right\| \left\| \vec{v} \right\| \cos\theta \tag{C.6}$$

that $\Pi_u(\vec{v})$ is a orthonormal projection of v on u that is:

$$\Pi_u(\vec{v}) = \left\| \vec{v} \right\| \cos \frac{\vec{u}}{\left\| \vec{u} \right\|} \frac{\left\| \vec{u} \right\|}{\left\| \vec{u} \right\|} = \frac{\vec{u}\vec{v}}{\left\| \vec{u} \right\|} \frac{\vec{u}}{\left\| \vec{u} \right\|} \tag{C.7}$$

and scalar product of u for itself results: $< \vec{u}, \vec{u} > = \left\| \vec{u} \right\|^2$ If $(\vec{v}_1, \vec{v}_2, \ldots, \vec{v}_N)$ are linearly independent:

$$\vec{u} = \sum_{j=0}^{N} \vec{u}_j \cdot \vec{v}_j \tag{C.8}$$

so:

$$\vec{u} \cdot \vec{v}_k = \sum_{j=0}^{N} u_j (\vec{v}_k \cdot \vec{v}_j) \qquad k = 1 \ldots N \tag{C.9}$$

and in matrix form:

$$\begin{bmatrix} \vec{v}_1 \cdot \vec{v}_1 & \vec{v}_1 \cdot \vec{v}_2 & \ldots & \vec{v}_1 \cdot \vec{v}_N \\ \vec{v}_1 \cdot \vec{v}_2 & \vec{v}_2 \cdot \vec{v}_2 & \ldots & \vec{v}_2 \cdot \vec{v}_N \\ \ldots & & & \\ \ldots & & & \\ \vec{v}_N \cdot \vec{v}_1 & \vec{v}_N \cdot \vec{v}_2 & \ldots & \vec{v}_N \cdot \vec{v}_N \end{bmatrix} \begin{bmatrix} u_1 \\ u_2 \\ \ldots \\ \ldots \\ u_N \end{bmatrix} = \begin{bmatrix} \vec{u} \cdot \vec{v}_1 \\ \vec{u} \cdot \vec{v}_2 \\ \ldots \\ \ldots \\ \vec{u} \cdot \vec{v}_N \end{bmatrix} \tag{C.10}$$

If the basis is orthogonal, the Gramian is the diagonal:

$$\begin{cases} \vec{v}_k \cdot \vec{v}_j & k \div j \\ \vec{v}_k \cdot \vec{v}_j = \delta_{kj} \left\| \vec{v}_j^2 \right\| \end{cases} \tag{C.11}$$

so :

$$\vec{u} \cdot \vec{v}_k = u_k (\vec{v}_k \vec{v}_k) \tag{C.12}$$

and in order to find the Fourier coefficients $u_k$:

$$u_k = \frac{\vec{u} \cdot \vec{v}_k}{\left\| \vec{v}_k \right\|^2} = \tag{C.13}$$

and if the vector base of $v_k$ is orthonormal $\left\|\overrightarrow{v}_k\right\|^2 = 1$ The pace of the periodic function is $\mathbf{L}_2([-l/2, l/2])$ is a vector space, l is the wave period and $\mathbf{L}_2$ is a vector. Two generic functions $f(x), g(x)$ are define in $\mathbf{L}_2$ whose properties are:

$$\begin{cases} f(x) + g(x) & \in \mathbf{L}^2 \\ \lambda \cdot f(x) \in \mathbf{L}^2 \end{cases} \tag{C.14}$$

It is defined also the scalar product (inner product) from which the angle between the two functions is obtained:

$$< f(x), g(x) >= f(x) \cdot g(x) = \int_{l/2}^{l/2} f(x)g(x)dx \tag{C.15}$$

If the f and g are discrete function:

$$f(x) \in \mathbf{R}^N = \begin{bmatrix} f(x_1) = f_1\sqrt{\Delta x} \\ f(x_2) = f_2\sqrt{\Delta x} \\ \dots \\ \dots \\ f(x_N) = f_N\sqrt{\Delta x} \end{bmatrix} \tag{C.16}$$

with $\Delta x = l/N$ and g :

$$g(x) \in \mathbf{R}^N = \begin{bmatrix} g(x_1) = g_1 \\ g(x_2) = g_2 \\ \dots \\ \dots \\ g(x_N) = g_N \end{bmatrix} \tag{C.17}$$

the inner product is defined:

$$\overrightarrow{f} \cdot \overrightarrow{g} = \sum_{j=1}^{N} f_j g_j \Delta x = \sum_{j=1}^{N} f(x_j)\overline{g}(x_j \Delta x \tag{C.18}$$

The function $g(x)$ can be expressed as a projection on a linearly independent function base of $\{f_1(x), f_2(x), \dots f_N(x), \dots\}$

$$g(x) = \sum_{k=1}^{inf} \alpha_k f_k(x) \tag{C.19}$$

A set of a linearly independent function is:

$$\left\{e^{-ik_o Nx}, e^{-ik_0(N-1)x}, e^{-ik_0(N-2)x}, \dots, e^{-2ik_0x}, \dots, e^{-ik_0x}, 1, e^{ik_0x}, \dots, e^{ik_oNx}\right\} \tag{C.20}$$

They are orthogonal to the scalar

$$< f_n, f_m >= \int_{-l/2}^{l/2} e^{ik_0 nx} e^{ik_0 mx} dx = \int_{-l/2}^{l/2} e^{ik_0 (n-m)x} dx = \begin{cases} l & \text{if } n = m \\ 0 & \text{if } n \neq m. \end{cases} = \delta_{nml} \tag{C.21}$$

and $\|f_n\| = \sqrt{l}$

$$g(x) = \sum_{-\inf}^{\inf} \alpha_n e^{ik_0 nx} \tag{C.22}$$

and the $\alpha_n$ coefficients are:

$$\alpha_n = \frac{g \cdot f_n}{\|f_n\|^2} = \frac{1}{l} \int_{-l/2}^{l/2} g(x) \bar{f}_n(x) dx = \frac{1}{l} \int_{-l/2}^{l/2} g(x) e^{-ik_0 nx} dx = \tag{C.23}$$

So if $g(x) \in \mathbf{L}^2$, then $\alpha_n \in \mathbf{C}^{2N} \sim \mathbf{R}^4$ represent a point:

$$\begin{bmatrix} \alpha_{-N} \\ \alpha_{-N+1} \\ \dots \\ \dots \\ \alpha_0 \dots \\ \dots \\ \alpha_{2N} \end{bmatrix} \tag{C.24}$$

# D

## APPENDIX D: SCALAR PRODUCT OF VECTORS IN $\mathbb{C}$

One important use of scalar product is in projections. The scalar product of two vectors $u, w \in \mathbb{C}^N$

$$u \cdot w =< u, w >= Re(u \cdot \overline{w}) \tag{D.1}$$

For example, if $u, w \in \mathbb{C}^2$ the scalar product is in 4D

$$u \cdot \overline{w} = (u_1 + iu_2) \cdot (w_1 - iw_2) = \underbrace{(u_1 w_1 + u_2 w_2)}_{Re(u \cdot \overline{w})} + i(u_2 w_1 - u_1 w_2) \tag{D.2}$$

it follows that:

$$< u, w >= \sum_{n=1}^{N} u_n \overline{w}_n \tag{D.3}$$

where $\overline{w}_n$ is the complex conjugate of $w_n$

# E

## APPENDIX E: ANALYTIC DETERMINATION OF DYNAMICAL AND GEOMETRIC PHASE VELOCITY EXPRESSIONS

Considering the $\dot{\alpha}_{tot}$ expression:

$$\dot{\alpha}_{tot} = \frac{T(Z)\cdot\dot{Z}}{|T(Z)|^2} - \frac{T(z)\cdot F(z)}{|T(z)|^2} = \dot{\alpha}_{geom} + \dot{\alpha}_{dynamic} \tag{E.1}$$

the geometric component in Fourier expansion is:

$$\dot{\alpha}_{geom} = \frac{\sum \Re[\overline{T(Z)}_n \dot{Z}_n]}{\sum n^2|Z_n|^2} = \frac{\sum \Re[-in\overline{Z}_n \dot{Z}_n]}{\sum n^2|Z_n|^2} \tag{E.2}$$

Considering the desymmetrized variables $Z_n$ (see equation 4.53 ) and substituting it in the geometric velocity(equation E.2), the numerator is:

$$\begin{aligned} -in\overline{Z}_n\dot{Z}_n &= -in\,|\overline{z_n}|\,e^{-i(\phi_n - n\phi_1)}\left[\frac{d\,|z_n|}{dt}e^{i(\phi_n-n\phi_1)} + i(\dot{\phi}_n - n\dot{\phi}_1)\,|z_n|\,e^{i(\phi_n-n\phi_1)}\right] = \\ &= -in\,|\overline{z_n}|\,\frac{d\,|z_n|}{dt} + n\,|z_n|^2\,(\dot{\phi}_n - n\dot{\phi}_1) \end{aligned} \tag{E.3}$$

taking into account $|\overline{z_n}| = |z_n|$ and the Re part is:

$$|z_n|^2\,(\dot{\phi}_n - n\dot{\phi}_1) \tag{E.4}$$

while the denominator is :

$$n^2|Z_n|^2 = n^2|z_n|^2 \tag{E.5}$$

Taking the $\mathbb{R}$ and the summation over n, the geometric component follows as :

$$\dot{\alpha}_{geom} = \frac{\sum n\,|z_n|^2\,(\dot{\phi}_n - n\dot{\phi}_1)}{\sum n^2\,|z_n|^2}. \tag{E.6}$$

The dynamical phase velocity in Fourier components is :

$$\dot{\alpha}_{dynamic} = -\frac{\sum \Re[\overline{T(z)_n}F_n(z)]}{\sum n^2|z_n|^2} = -\frac{\sum \Re[-in\overline{z_n}\dot{z}_n]}{\sum n^2|z_n|^2} \tag{E.7}$$

where $\dot{z}_n = F_n(z)$, based on the definition of dynamical system. Taking into account $z_n = |z_n| e^{i\phi_n}$ and its time derivative

$$\dot{z}_n = |\dot{z}_n| e^{i\phi_n} + i\dot{\phi}_n |z_n| e^{i\phi_n} \tag{E.8}$$

and substituting it in $\dot{\alpha}_{dyn}$

$$\dot{\alpha}_{dynamic} = -\frac{\sum \Re\left[-in\overline{z_n}\left(|\dot{z}_n| e^{i\phi_n} + i\dot{\phi}_n |z_n| e^{i\phi_n}\right)\right]}{n^2 |z_n|^2} \tag{E.9}$$

Performing the products and considering the conjugate expression $\overline{z_n} = |\overline{z_n}| e^{-i\phi_n}$

$$\dot{\alpha}_{dynamic} = -\frac{\sum \Re\left[-in |\overline{z_n}| |\dot{z}_n| - n |\overline{z_n}| |z_n| \dot{\phi}_n\right]}{n^2 |z_n|^2} \tag{E.10}$$

Taking the $\mathbb{R}$ part allows to obtain the dynamical phase velocity as a function of the phase velocities of all the harmonics:

$$\dot{\alpha}_{dynamic} = -\frac{\sum n^2 |z_n|^2 \frac{\dot{\phi}_n}{n}}{\sum n^2 |z_n|^2} \tag{E.11}$$

Finally the value of $\alpha_{tot}$ as the sum of $\alpha_{dynamic}$ and $\alpha_{geom}$ is:

$$\begin{aligned} \dot{\alpha}_{tot} =& -\frac{\sum n^2 |z_n|^2 \frac{\dot{\phi}_n}{n}}{\sum n^2 |z_n|^2} - \frac{\sum n |z_n|^2 (\dot{\phi}_n - n\dot{\phi}_1)}{\sum n^2 |z_n|^2} = \\ =& \frac{\sum n |z_n|^2 (\dot{\phi}_n - \dot{\phi}_n) - n^2 |z_n|^2 \dot{\phi}_1}{\sum n^2 |z_n|^2} = \dot{\phi}_1 \end{aligned} \tag{E.12}$$

# F

## APPENDIX F: ANALYTIC DETERMINATION OF SURFACE ELEVATION $\eta(x,t)$ FOR A WAVE GROUP WITH A GAUSSIAN SPECTRUM

Let the wave elevation $\eta(x,t)$ with a generic dispersion law $w(k)$ and the Gaussian shaped spectrum $S(k)$ with variance $\sigma^2$ be:

$$\eta(x,t) = \int_{-\infty}^{\infty} S(k) e^{i(kx - w(k)t)} dk \tag{F.1}$$

and

$$S(k) = \frac{1}{\sqrt{2\pi\sigma^2}} e^{-\frac{1}{2}\frac{(k-k_0)^2}{\sigma^2}} \tag{F.2}$$

The wave elevation can be written making explicit the dispersion law $w = k^2$ for capillary type wave group:

$$\eta(x,t) = \int_{-\infty}^{\infty} S(k) e^{i(kx - \frac{w_0}{k_0^2}k^2 t)} dk \tag{F.3}$$

where $w_0/k_0^2 = 1$ and $w_0$ and $k_0$ are respectively the wave number of the spectra peak and the associated frequency computed via the dispersion relation.

Substituting the Gaussian spectrum (equation F.2) in the wave elevation (F.1) yields:

$$\eta(x,t) = \int_{-\infty}^{\infty} \frac{1}{\sqrt{2\pi\sigma^2}} e^{-\frac{1}{2\sigma^2}(k-k_0)^2} e^{i(kx - \frac{w_0}{k_0^2}k^2 t)} dk \tag{F.4}$$

Taking into account only the exponent part:

$$-\frac{1}{2\sigma^2}(k-k_0)^2 + i(kx - \frac{w_0}{k_0^2}k^2 t) \tag{F.5}$$

and performing the multiplications :

$$\frac{1}{2\sigma^2}\left[-k^2(1 + 2i\sigma\frac{w_0}{k_0^2}t) + k(2k_0 + 2i\sigma^2 x) - k_0^2\right] \tag{F.6}$$

In order to simplify the integral, it is written as:

$$\eta(x,t) = \frac{1}{\sqrt{2\pi\sigma^2}} \int_{-\infty}^{\infty} e^{-Ak^2 + Bk + C} dk \tag{F.7}$$

with

$$A = \frac{1}{(2\sigma^2)}(1 + 2i\sigma^2 w_0/k_0^2 t) \tag{F.8a}$$

$$B = 1/(2\sigma^2)(2k_0 + 2ix\sigma^2) \tag{F.8b}$$

$$C = -1/(2\sigma^2)k_0^2 \tag{F.8c}$$

The exponent can be written as:

$$-Ak^2 + Bk + C = -(\sqrt{A}k - \frac{B}{2\sqrt{A}})^2 + \frac{B^2}{4A} + C \tag{F.9}$$

so the integral becomes:

$$\begin{aligned}\eta(x,t) &= \frac{1}{\sqrt{2\pi\sigma^2}}\int_{-\infty}^{\infty} e^{-(\sqrt{A}k - \frac{B}{2\sqrt{A}})^2} e^{(\frac{B^2}{4A} + C)} dk = \\ &= \frac{1}{\sqrt{2\pi\sigma^2}} e^{(\frac{B^2}{4A} + C)} \int_{-\infty}^{\infty} e^{-(\sqrt{A}k - \frac{B}{2\sqrt{A}})^2} dk\end{aligned} \tag{F.10}$$

The Gaussian integral

$$I = \int_{-\infty}^{\infty} e^{-y^2} dy = \sqrt{\pi} \tag{F.11}$$

can be used to solve the surface wave integral $\eta(x,t)$ analytically, making a change of variables such that:

$$y = \sqrt{A}k - \frac{B}{2\sqrt{B}} \tag{F.12}$$

that yields:

$$dy = \sqrt{A}dk \tag{F.13}$$

and

$$dk = \frac{dy}{\sqrt{A}} \tag{F.14}$$

The equation F.10 can be written and

$$\eta(x,t) = \frac{1}{\sqrt{2\pi\sigma^2}} e^{(\frac{B^2}{4A} + C)} \int_{-\infty}^{\infty} e^{-}y^2 dy \tag{F.15}$$

the Analytical integration of the Gaussian integral yields the simplified form

$$\eta(x,t) = \frac{1}{\sqrt{2\pi\sigma^2}} \sqrt{\frac{\pi}{A}} e^{(\frac{B^2}{4A} + C)} \tag{F.16}$$

Switching space with time in the time-space system of reference allows changing the dispersion law from capillary
$mathitw(k) = k^2$ to deep water gravity waves types $w = \sqrt{k}$.

# BIBLIOGRAPHY


Abe, H., Kawamura, H., and Matsuo, Y. (2001). Direct numerical simulation of a fully developed turbulent channel flow with respect to the reynolds number dependence. *Journal of fluids Engineering*, 123(2):382–393.

Absi, R. (2009). A simple eddy viscosity formulation for turbulent boundary layers near smooth walls. *Comptes Rendus Mecanique*, 337(3):158–165.

Alfonsi, G., Ciliberti, S. A., Mancini, M., and Primavera, L. (2016). Direct numerical simulation of turbulent channel flow on high-performance gpu computing system. *Computation*, 4(1):13.

Alfonsi, G. and Primavera, L. (2007). Direct numerical simulation of turbulent channel flow with mixed spectral-finite difference technique. *Journal of Flow Visualization and Image Processing*, 14(2).

Antonia, R., Orlandi, P., and Romano, G. (1998). Scaling of longitudinal velocity increments in a fully developed turbulent channel flow. *Physics of Fluids*, 10(12):3239–3241.

Antonia, R., Teitel, M., Kim, J., and Browne, L. (1992). Low-reynolds-number effects in a fully developed turbulent channel flow. *Journal of Fluid mechanics*, 236:579–605.

Antonia, R., Zhou, T., and Romano, G. (1997). Second-and third-order longitudinal velocity structure functions in a fully developed turbulent channel flow. *Physics of Fluids*, 9(11):3465–3471.

Aref, H. (2007). Point vortex dynamics: a classical mathematics playground. *Journal of mathematical Physics*, 48(6):065401.

Bernardini, M., Pirozzoli, S., and Orlandi, P. (2014). Velocity statistics in turbulent channel flow up to $re_\tau = 4000$. *Journal of Fluid Mechanics*, 742:171–191.

Boccotti, P. (2000). *Wave mechanics for ocean engineering*. Elsevier.

Boccotti, P. (2008). Quasideterminism theory of sea waves. *Journal of offshore mechanics and Arctic engineering*, 130(4).

Budanur, N. B., Cvitanović, P., Davidchack, R. L., and Siminos, E. (2015). Reduction of so (2) symmetry for spatially extended dynamical systems. *Physical review letters*, 114(8):084102.

Burghardt, G. M. (2005). *The genesis of animal play: Testing the limits*. Mit Press.

Cenedese, A., Romano, G., and Antonia, R. (1998). A comment on the "linear" law of the wall for fully developed turbulent channel flow. *Experiments in Fluids*, 25(2):165–170.

Chandler, G. J. and Kerswell, R. R. (2013). Invariant recurrent solutions embedded in a turbulent two-dimensional kolmogorov flow. *Journal of Fluid Mechanics*, 722:554–595.

Chorin, A. J., Marsden, J. E., and Marsden, J. E. (1990). *A mathematical introduction to fluid mechanics*, volume 175. Springer.

Cvitanovic, P., Artuso, R., Mainieri, R., Tanner, G., Vattay, G., Whelan, N., and Wirzba, A. (2005). Chaos: classical and quantum. *ChaosBook.org (Niels Bohr Institute, Copenhagen 2005)*, 69.

Cvitanović, P. and Gibson, J. (2010). Geometry of the turbulence in wall-bounded shear flows: periodic orbits. *Physica Scripta*, 2010(T142):014007.

da Vinci, M. L. (2020). Leonardo da vinci.l'acqua microscopio della natura. il codice leicester di leonardo da vinci—museo da vinci.

De Villiers, E. (2006). The potential of large eddy simulation for the modeling of wall bounded flows. *Imperial College of Science, Technology and Medicine*.

Dean, R. B. (1978). Reynolds number dependence of skin friction and other bulk flow variables in two-dimensional rectangular duct flow.

Del Alamo, J. C. and Jiménez, J. (2003). Spectra of the very large anisotropic scales in turbulent channels. *Physics of Fluids*, 15(6):L41–L44.

Del Álamo, J. C. and Jiménez, J. (2009). Estimation of turbulent convection velocities and corrections to taylor's approximation. *Journal of Fluid Mechanics*, 640:5–26.

del Álamo, J. C., Jiménez, J., Zandonade, P., and Moser, R. D. (2003). Scaling of the energy spectra of turbulent channels. *APS*, 56:DA–002.

Delfour, F. and Aulagnier, S. (1997). Bubbleblow in beluga whales (delphinapterus leucas): a play activity? *Behavioural Processes*, 40(2):183–186.

Eckelmann, H. (1974). The structure of the viscous sublayer and the adjacent wall region in a turbulent channel flow. *Journal of Fluid Mechanics*, 65(3):439–459.

Fedele, F. (2012). Travelling waves in axisymmetric pipe flows. *Fluid Dynamics Research*, 44(4):045509.

Fedele, F. (2014). Geometric phases of water waves. *EPL (Europhysics Letters)*, 107(6):69001.

Fedele, F., Abessi, O., and Roberts, P. J. (2015). Symmetry reduction of turbulent pipe flows. *Journal of Fluid Mechanics*, 779:390–410.

Fedele, F., Banner, M. L., and Barthelemy, X. (2019). Crest speeds of unsteady surface water waves. *arXiv preprint arXiv:1910.07946*.

Fedele, F., Banner, M. L., and Barthelemy, X. (2020). Crest speeds of unsteady surface water waves. *Journal of Fluid Mechanics*, 899.

Fedele, F., Brennan, J., De León, S. P., Dudley, J., and Dias, F. (2016). Real world ocean rogue waves explained without the modulational instability. *Scientific reports*, 6:27715.

Fedele, F. and Dutykh, D. (2013a). Camassa–holm equations and vortexons for axisymmetric pipe flows. *Fluid Dynamics Research*, 46(1):015503.

Fedele, F. and Dutykh, D. (2013b). Vortexons in axisymmetric poiseuille pipe flows. *EPL (Europhysics Letters)*, 101(3):34003.

Fedele, F., Lugni, C., and Chawla, A. (2017). The sinking of the el faro: predicting real world rogue waves during hurricane joaquin. *Scientific reports*, 7(1):1–15.

Ferziger, J. H., Perić, M., and Street, R. L. (2002). *Computational methods for fluid dynamics*, volume 3. Springer.

Friedlaender, A., Bocconcelli, A., Wiley, D., Cholewiak, D., Ware, C., Weinrich, M., and Thompson, M. (2011). Underwater components of humpback whale bubble-net feeding behaviour. *Behaviour*, 148(5-6):575–602.

Frisch, U. (1995). *Turbulence: the legacy of AN Kolmogorov*. Cambridge university press.

Gerritsen, D. and Kuipers, M. (1979). On the angular motion of a freely falling human or animal body. *Journal of Engineering Mathematics*, 13(4):347–353.

Hernández-Garduño, A. and Shashikanth, B. N. (2018). Reconstruction phases in the planar three-and four-vortex problems. *Nonlinearity*, 31(3):783.

Hopf, H. (1930). Uber die abbildungen der dreidimensionalen sphare aufdie kugelflache. *Mathematische Annalen*, 104:639–665.

Hopf, H. (1931). Über die abbildungen der dreidimensionalen sph'dre aufdie kugelfidche. *Math. Ann*, 104:637–665.

Hopf, H. (1935). Über die abbildungen von sphären auf sphäre niedrigerer dimension. *Fundamenta Mathematicae*, 25(1):427–440.

Hoyas, S. and Jiménez, J. (2006). Scaling of the velocity fluctuations in turbulent channels up to re $\tau$= 2003. *Physics of fluids*, 18(1):011702.

Hu, Z. W., Morfey, C. L., and Sandham, N. D. (2006). Wall pressure and shear stress spectra from direct simulations of channel flow. *AIAA journal*, 44(7):1541–1549.

Hua, B. and Klein, P. (1998). An exact criterion for the stirring properties of nearly two-dimensional turbulence. *Physica D: Nonlinear Phenomena*, 113(1):98–110.

Huntley, M. E. and Zhou, M. (2004). Influence of animals on turbulence in the sea. *Marine Ecology Progress Series*, 273:65–79.

Iwamoto, K., Kasagi, N., and Suzuki, Y. (2005). Direct numerical simulation of turbulent channel flow at re$\tau$= 2320. In *Proc. 6th Symp. Smart Control of Turbulence*, pages 327–333.

Iwamoto, K., Suzuki, Y., and Kasagi, N. (2002). Reynolds number effect on wall turbulence: toward effective feedback control. *International journal of heat and fluid flow*, 23(5):678–689.

Jones, B. and Kuczaj, S. (2014). Ii.(2014). beluga (delphinapterus leucas) novel bubble helix play behavior. *Animal Behavior and Cognition*, 1(2):206–214.

Kasagi, N., Tomita, Y., and Kuroda, A. (1992). Direct numerical simulation of passive scalar field in a turbulent channel flow.

Kim, J. (2012). Progress in pipe and channel flow turbulence, 1961–2011. *Journal of Turbulence*, (13):N45.

Kim, J., Moin, P., and Moser, R. (1987). Turbulence statistics in fully developed channel flow at low reynolds number. *Journal of fluid mechanics*, 177:133–166.

Kolmogorov, A. N. (1941). The local structure of turbulence in incompressible viscous fluid for very large reynolds numbers. *Cr Acad. Sci. URSS*, 30:301–305.

Kolmogorov, A. N. (1962). A refinement of previous hypotheses concerning the local structure of turbulence in a viscous incompressible fluid at high reynolds number. *Journal of Fluid Mechanics*, 13(1):82–85.

Komen, E., Shams, A., Camilo, L., and Koren, B. (2014). Quasi-dns capabilities of openfoam for different mesh types. *Computers & Fluids*, 96:87–104.

Kraichnan, R. H. (1967). Inertial ranges in two-dimensional turbulence. *The Physics of Fluids*, 10(7):1417–1423.

Krishnan, K., Ben-Gida, H., Morgan, G., Kopp, G. A., Guglielmo, C. G., and Gurka, R. (2020). Turbulent wake-flow characteristics in the near wake of freely flying raptors: a comparative analysis between an owl and a hawk. *Integrative and Comparative Biology*.

Lee, M. and Moser, R. D. (2015). Direct numerical simulation of turbulent channel flow up to $re_\tau = 5200$. *Journal of Fluid Mechanics*, 774:395–415.

Lesieur, M. (2012). *Turbulence in fluids*, volume 40. Springer Science & Business Media.

Leweke, T., Le Dizes, S., and Williamson, C. H. (2016). Dynamics and instabilities of vortex pairs. *Annual Review of Fluid Mechanics*, 48:507–541.

Lighthill, M. (1960). Note on the swimming of slender fish. *Journal of fluid Mechanics*, 9(2):305–317.

Lozano-Durán, A., Flores, O., and Jiménez, J. (2012). The three-dimensional structure of momentum transfer in turbulent channels. *Journal of Fluid Mechanics*, 694:100.

Lozano-Durán, A. and Jiménez, J. (2014). Effect of the computational domain on direct simulations of turbulent channels up to re $\tau$= 4200. *Physics of Fluids*, 26(1):011702.

Luchini, P. (2017). Universality of the turbulent velocity profile. *Physical review letters*, 118(22):224501.

Lupandin, A. (2005). Effect of flow turbulence on swimming speed of fish. *Biology Bulletin*, 32(5):461–466.

Lyons, S. L., Hanratty, T. J., and McLaughlin, J. B. (1991). Large-scale computer simulation of fully developed turbulent channel flow with heat transfer. *International journal for numerical methods in fluids*, 13(8):999–1028.

Mallon, J. M., Bildstein, K. L., and Katzner, T. E. (2016). In-flight turbulence benefits soaring birds. *The Auk: Ornithological Advances*, 133(1):79–85.

Marey, M. (1894). Des mouvements que certains animaux exécutent pour retomber sur leurs pieds, lorsqu'ils sont précipités d'un lieu élevé. 119:714–717.

Marocco, L. and Franco, A. (2017). Direct numerical simulation and rans comparison of turbulent convective heat transfer in a staggered ribbed channel with high blockage. *Journal of Heat Transfer*, 139(2).

Marsden, J. E., Montgomery, R., and Raţiu, T. S. (1990). *Reduction, symmetry, and phases in mechanics*, volume 436. American Mathematical Soc.

Marten, K., Shariff, K., Psarakos, S., and White, D. J. (1996). Ring bubbles of dolphins. *Scientific American*, 275(2):82–87.

Mathieu, J. and Scott, J. (2000). *An introduction to turbulent flow*. Cambridge University Press.

McCowan, B., Marino, L., Vance, E., Walke, L., and Reiss, D. (2000). Bubble ring play of bottlenose dolphins (tursiops truncatus): Implications for cognition. *Journal of Comparative Psychology*, 114(1):98.

Meringolo, D. (2009). Caratterizzazione frattale del moto turbolento.

Meunier, P., Le Dizes, S., and Leweke, T. (2005). Physics of vortex merging. *Comptes Rendus Physique*, 6(4-5):431–450.

Moreno, K. and Macgregor, R. (2019). Bubble trails, bursts, rings, and more: a review of multiple bubble types produced by cetaceans. *Anim. Behav. Cogn*, 6:105–126.

Moser, R. D., Kim, J., and Mansour, N. N. (1999). Direct numerical simulation of turbulent channel flow up to re $\tau$= 590. *Physics of fluids*, 11(4):943–945.

Mukha, T. and Liefvendahl, M. (2015). Large-eddy simulation of turbulent channel flow.

Nelkin, M. (2000). Resource letter tf-1: turbulence in fluids. *American Journal of Physics*, 68(4):310–318.

Péntek, A., Tél, T., and Toroczkai, T. (1995). Chaotic advection in the velocity field of leapfrogging vortex pairs. *Journal of Physics A: Mathematical and General*, 28(8):2191.

Pope, S. B. (2001). Turbulent flows.

Romano, G., Antonia, R., and Zhou, T. (1999). Evaluation of lda temporal and spatial velocity structure functions in a low reynolds number turbulent channel flow. *Experiments in fluids*, 27(4):368–377.

Romano, G. P. (1995). Analysis of two-point velocity measurements in near-wall flows. *Experiments in fluids*, 20(2):68–83.

Rowley, C. W. (2005). Model reduction for fluids, using balanced proper orthogonal decomposition. *International Journal of Bifurcation and Chaos*, 15(03):997–1013.

Ruelle, D. (1976). The lorenz attractor and the problem of turbulence. In *Turbulence and Navier Stokes Equations*, pages 146–158. Springer.

Rutledge, J. and Sleicher, C. A. (1993). Direct simulation of turbulent flow and heat transfer in a channel. part i: Smooth walls. *International journal for numerical methods in fluids*, 16(12):1051–1078.

Shapere, A. and Wilczek, F. (1989). Geometry of self-propulsion at low reynolds number. *Journal of Fluid Mechanics*, 198:557–585.

Shashikanth, B. N. and Marsden, J. E. (2003). Leapfrogging vortex rings: Hamiltonian structure, geometric phases and discrete reduction. *Fluid Dynamics Research*, 33(4):333–356.

Siggia, E. D. and Aref, H. (1981). Point-vortex simulation of the inverse energy cascade in two-dimensional turbulence. *The Physics of Fluids*, 24(1):171–173.

Siminos, E. and Cvitanović, P. (2011). Continuous symmetry reduction and return maps for high-dimensional flows. *Physica D: Nonlinear Phenomena*, 240(2):187–198.

Sreenivasan, K. R. (1999). Fluid turbulence. *Reviews of Modern Physics*, 71(2):S383.

Tanahashi, M., Kang, S.-J., Miyamoto, T., Shiokawa, S., and Miyauchi, T. (2004). Scaling law of fine scale eddies in turbulent channel flows up to re$\tau$= 800. *International Journal of Heat and Fluid Flow*, 25(3):331–340.

Taylor, G. I. (1938). The spectrum of turbulence. *Proceedings of the Royal Society of London. Series A-Mathematical and Physical Sciences*, 164(919):476–490.

Treccani, E. (2020). Turbolenza da treccani.

Van Dyke, M. and Van, D. (1982). *An Album of Fluid Motion*. An Album of Fluid Motion. Parabolic Press.

Vo, S., Kronenburg, A., Stein, O. T., and Hawkes, E. R. (2016). Direct numerical simulation of non-premixed syngas combustion using openfoam. In *High Performance Computing in Science and Engineering´ 16*, pages 245–257. Springer.

Vortmeyer-Kley, R., Gräwe, U., and Feudel, U. (2016). Detecting and tracking eddies in oceanic flow fields: a lagrangian descriptor based on the modulus of vorticity. *Nonlinear Processes in Geophysics*, 23(4):159–173.

Vreman, A. and Kuerten, J. G. (2014a). Comparison of direct numerical simulation databases of turbulent channel flow at re $\tau$= 180. *Physics of Fluids*, 26(1):015102.

Vreman, A. and Kuerten, J. G. (2014b). Statistics of spatial derivatives of velocity and pressure in turbulent channel flow. *Physics of fluids*, 26(8):085103.

Wikipedia (2020). Leonardo da vinci — wikipedia.

Willis, A. P., Cvitanović, P., and Avila, M. (2013). Revealing the state space of turbulent pipe flow by symmetry reduction. *Journal of Fluid Mechanics*, 721:514–540.

Willmarth, W. (1975). Pressure fluctuations beneath turbulent boundary layers. *Annual review of fluid mechanics*, 7(1):13–36.

Zhang, F., Bonart, H., Zirwes, T., Habisreuther, P., Bockhorn, H., and Zarzalis, N. (2015). Direct numerical simulation of chemically reacting flows with the public domain code openfoam. In *High Performance Computing in Science and Engineering '14*, pages 221–236. Springer.

Zheng, E., Rudman, M., Singh, J., and Kuang, S. (2019). Direct numerical simulation of turbulent non-newtonian flow using openfoam. *Applied Mathematical Modelling*, 72:50–67.